Effect of Nozzle Geometry on Mixing Characteristics of Turbulent Free Orifice Jets

by

Yaw Yeboah Afriyie

A Thesis submitted to the Faculty of Graduate Studies of

The University of Manitoba

in partial fulfilment of the requirements of the degree of

MASTER OF SCIENCE

Department of Mechanical Engineering

University of Manitoba

Winnipeg

ABSTRACT

An experimental investigation was conducted using particle image velocimetry to study the effect of nozzle geometry on turbulent free orifice jets. The nozzle geometries studied include the round, cross, flower, star, rectangular and elliptical nozzles (aspect ratio 2). The spread rate of the rectangular nozzle was 61% greater than the square nozzle while the elliptical nozzle was 45% greater than the round nozzle using the conventional half velocity width. The superior mixing capacity of the rectangular and elliptical nozzles is attributed to the axis-switching mechanism. Evaluation of the energy budget showed a higher level of production of turbulence and convection of the mean flow for the rectangular nozzle compared with the round nozzle. Two-point auto-correlation function revealed larger structures in the non-circular nozzles and in particular the rectangular nozzle. The Kolmogorov and Taylor microscales however, did not show any significant dependency on nozzle geometry.

ACKNOWLEDGEMENTS

I would like to express my profound gratitude to my academic advisor, Dr. Mark F. Tachie for his continual support, encouragement and constructive criticism

I am very grateful to Price Industries Limited and the University of Manitoba (University of Manitoba Graduate Fellowship) for the financial support I received during my stay at the University of Manitoba

I would also like to acknowledge the technical support received from Paul Krueger, Mike Koupriyanov and Tom Epp. The support and encouragement received from Baafour Nyantekyi-Kwakye and Ebenezer Essel is duly noted and appreciated.

DEDICATION

This thesis is dedicated to my parents, Mr. & Mrs. Afriyie for their love and support throughout my stay in the University of Manitoba.

TABLE OF CONTENTS

LIST OF TABLES

LIST OF FIGURES

NOMENCLATURE

English

d	equivalent diameter of non-circular nozzles or diameter of round nozzle
d_p	diameter of seeding particle
g	acceleration due to gravity
K_u	mean velocity decay rate
K_s	spread rate of jet
$K_{s0.1\text{-}0.9}$	jet thickness rate
L	integral length scale
L_c	potential core length
m_e	mass entrainment of jet
Re_j	Reynolds number based on jet exit velocity and (equivalent) diameter of nozzle
Re_b	Reynolds number based on exit bulk velocity and (equivalent) diameter of nozzle
Re_a	Reynolds number based on jet exit velocity and the major axis diameter of an elliptical nozzle
R_{uu}	streamwise two-point auto-correlation function
R_{vv}	transverse two-point auto-correlation function
t_r	particle response time
T	integral time scale
U	streamwise mean velocity
U_b	exit bulk velocity
$\sqrt{\overline{u^2}}, \sqrt{\overline{v^2}}$	streamwise and transverse turbulent intensities

U_c	streamwise mean velocity on the jet centerline
U_j	jet exit velocity
U_m	maximum streamwise mean velocity on the jet centerline
$\overline{u^2}$, $\overline{v^2}$	Reynolds normal stress in the streamwise and transverse directions
$-\overline{uv}$	Reynolds shear stress
v_s	settling velocity of seeding particles
V	transverse mean velocity
x	streamwise distance
y	transverse distance
$y_{0.1}$	transverse distance from the jet centerline to the point corresponding to $0.1U_c$
$y_{0.25}$	transverse distance from the jet centerline to the point corresponding to $0.25U_c$
$y_{0.5}$	transverse distance from the jet centerline to the point corresponding to $0.5U_c$
$y_{0.75}$	transverse distance from the jet centerline to the point corresponding to $0.75U_c$
$y_{0.9}$	transverse distance from the jet centerline to the point corresponding to $0.9U_c$

Greek

Δs	local displacement vector
Δt	laser time delay
η	Kolmogorov length scale
λ	Taylor microscale
ρ_f	fluid density
ρ_p	seeding particle density
μ_f	dynamic viscosity of fluid

v	kinematic velocity of fluid
v_t	eddy viscosity
Ω_x	streamwise mean vorticity
Ω_z	spanwise mean vorticity

Acronyms

AR	aspect ratio
CCD	charged coupled device
DNS	direct numerical simulation
IA	interrogation area
Nd:YAG	Neodymium: Yttrium Aluminum Garnet
PIV	Particle image velocimetry

CHAPTER 1

1 INTRODUCTION

1.1 Motivation

A turbulent free jet is formed when a jet of fluid is injected into another fluid medium, but the development of the jet is free from the effects of solid or free surface boundaries. Turbulent free jets have diverse engineering applications which include heating ventilation and air conditioning (HVAC) systems, disposal of industrial waste, combustion and heat transfer augmentation. Also, due to their relative simplicity compared to wall-bounded turbulent shear flows, they are used as prototypical flows for exploring turbulent flow dynamics. In HVAC applications for instance, entrainment is required for optimal performance. There is therefore the need to conduct research to identify ways (e.g. optimal nozzle configurations) that will maximize induction and mixing between the core jet and the ambient flow.

Due to their immense practical applications and fundamental importance, turbulent free jets have received considerable research attention. Experimental techniques such as hot-wire anemometry (HWA), laser Doppler anemometry (LDA) and particle image velocimetry (PIV), as well as numerical methods such as direct numerical simulation (DNS) have been employed to investigate the flow physics of turbulent free jets.

Initial conditions or parameters that affect the development of the jet flow, especially in the region near the nozzle exit, include the aspect ratio of non-circular nozzles (Lee & Baek, 1994), exit turbulence levels (Goldschmidt & Bradshaw, 1981), jet exit Reynolds number (*Re*) (Abdel-Rahman et al., 1996), nozzle geometry (Ho & Gutmark, 1987), and nozzle type (Mi et al., 2001).

For example, jet flows of practical importance may be produced from three main types of nozzles: contoured (or smooth contracting) nozzles, orifice plates and long pipes. The mixing performance of a round jet issuing from these three nozzle types was studied by Mi et al. (2001). The investigation revealed that the orifice plate nozzle provided the greatest rate of mixing with the ambient fluid and the pipe jet was the least efficient nozzle type. Although the presence of large-scale coherent structures existed in both the smooth contraction and orifice plate nozzles, the three-dimensionality of these structures were observed to be higher in the orifice plate nozzle. This resulted in the highest rate of decay of centerline temperature and the highest spread rate of the jet occurring in the orifice plate nozzle.

A round jet issues from a circular or axisymmetric nozzle, while a plane jet issues from a rectangular nozzle with a high aspect ratio, usually more than 50 (Pope, 2000). Most of the fundamental research on jet flows have focused on round and planar jets issuing from contoured nozzles, with those issuing from orifice plates receiving relatively less attention. More recently however, non-circular nozzles have attracted research attention because they provide enhanced mixing between jet flows and the ambient fluid which surrounds it when compared to their circular counterparts (Gutmark & Grinstein, 1999).

The overwhelming number of research on turbulent jet flows focused on free jets at high Reynolds numbers, where the effect of Reynolds number is not expected to affect the jet development and mixing characteristics. However, in some practical applications such as in HVAC systems, the devices are operated at relatively low Reynolds numbers. Also, since entrainment and hence mixing of the ambient fluid with the core jet is desired, the effect of different nozzle geometries

have been investigated by different researchers. However, the test facility, measurement technique and initial conditions of the various studies were not necessarily uniform. This presents a challenge when a comparison of the most effective nozzle geometry is to be made from the different studies. Toward this end, a research collaboration was established between the University of Manitoba and Price Industries Limited, a leading manufacturer and producer of HVAC systems in North America, to study the effect of nozzle geometry on turbulent free jets at relatively low Reynolds numbers.

1.2 Objective and scope of research

The objective of the study is to examine the effect of nozzle geometry on the mixing performance of turbulent free orifice jets at identical initial conditions. The measurements are performed at relatively low Reynolds numbers. The nozzle geometries considered include the round, square, ellipse and rectangle (of aspect ratio 2), cross, flower and star shapes. The nozzles have the same opening area or equivalent diameter (d) to facilitate comparison.

A high resolution particle image velocimetry (PIV) system is used to perform the velocity measurements. The experiments are conducted in two stages; in the first stage, the mean characteristics of the flow are studied by analyzing the mean velocity decay rate, the spread rate and the mass entrainment of the various jets considered. For the second stage, the mixing performance of the best nozzles from the first stage are further analyzed by employing contour plots of their mean velocity, spanwise mean vorticity, turbulent intensities and Reynolds shear stress. One-dimensional profiles of the mean velocity, turbulent intensity, Reynolds shear stress and some terms of the turbulent kinetic energy budget of the best nozzle geometries are also

evaluated to systematically examine the flow features of the jets. Two-point auto-correlation function is also used to examine the statistical features of the coherent structures that exist in the flow.

The results from this research will advance our understanding of jet flows and provide valuable experimental data for validating numerical models. The results will also provide information for the HVAC industry to potentially design more efficient and environmentally friendlier air distribution systems.

1.3 Thesis structure

In chapter 2, a description of the free jet flow field and a review of previous studies are presented. Chapter 3 provides an overview of the experimental setup and measurement procedure employed in the study. The results and discussions are then presented in Chapter 4, and conclusions and recommendations for future works are presented in Chapter 5.

CHAPTER 2

2 LITERATURE REVIEW

In this chapter, an overview of the free jet flow field is presented. This is followed by a review of the relevant investigations highlighting the effect of different initial conditions on the jet flow field and a summary of the major conclusions.

2.1 Overview of free jet flow

The turbulent free jet forms part of a broader group of turbulent flows known as free shear flows. Other examples of free shear flows include the wake and mixing layer. Free shear flows develop in the absence of boundaries (solid and free surface) and the turbulence arises due to mean velocity differences (Pope, 2000). The flow field of jets issuing from round and plane nozzles can be characterized by two spatially independent variables or two-dimensions. Three-dimensional jets (e.g. elliptical and triangular) however, require three spatially independent variables to completely characterize the flow field. For example, the asymmetric shape of the elliptical nozzle causes different behaviour in its major and minor axes. Due to the relative simplicity of round and planar jets compared to their three-dimensional or asymmetric counterparts, they have typically been used in the vast majority of the fundamental research on jet flows.

Figure 2.1 shows the schematic of a free jet issuing into a quiescent environment. The streamwise and transverse directions are represented as x and y respectively and the origin of the x-y plane is at the centerline of the nozzle exit. The nozzle diameter or equivalent diameter (which is defined as the diameter of a circle with the same opening area as a non-circular nozzle) is represented as d. As the jet discharges from the nozzle, it entrains the surrounding fluid and spreads in the

transverse direction with increasing streamwise distance. For jets issuing from both contoured nozzles and long pipes, the jet velocity on the centerline (U_c) remains constant for the first few nozzle diameters downstream of the nozzle, before decaying with streamwise distance due to the entrainment of the ambient fluid into the core jet. In the case of orifice plate jets however, U_c increases from the nozzle exit till it reaches a maximum (U_m) away from the nozzle exit due to the well-known vena contracta effect. After reaching U_m, the centerline velocity of the jet then decays with streamwise distance.

Three distinct axial regions are usually defined for jet flows; the potential core, transition (or developing) and developed regions (Figure 2.1). The potential core region may be defined as the distance from the nozzle exit to the point where the centerline mean velocity has decayed to 99% of the jet exit velocity. The developing region is the transition zone between the potential core and developed regions. The potential core and the early stage of the transition region are often referred to as the near-field or initial region of the jet. In the developed region, the distributions of the dimensionless streamwise mean velocity are self-similar and for this reason, it is sometimes referred to as the self-similar or fully developed region (Lipari & Stansby, 2011). With the exception of a few studies (George, 1989), the general viewpoint is that the higher order turbulent statistics also become self-similar in this region, but at greater streamwise distances compared with the mean velocity (Wygnanski & Fiedler, 1969).

The exact demarcation between the various regions, however, may depend on initial conditions like the exit Reynolds number, turbulence levels and the nozzle geometry used. In the near-field, an intense entrainment and hence mixing of the ambient fluid and the core jet takes place and the

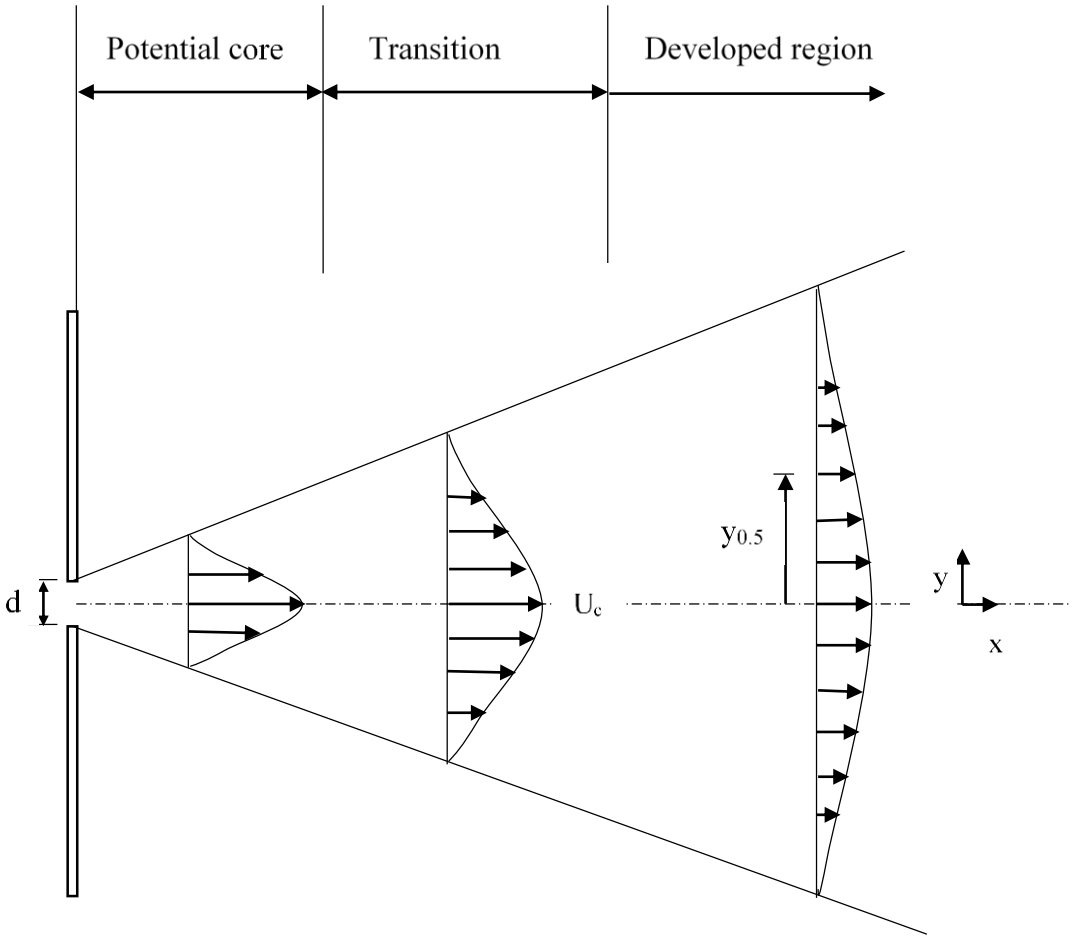

Figure 2.1: Free jet flow field and coordinate system used

large-scale coherent structures are believed to be responsible for this phenomenon. Since the upstream conditions of the jet flow can significantly influence heat, mass and momentum transfer, the near-field region is of immense importance in practical applications of jets (Abdel-Rahman, 2010).

In the shear layer of the free jet, vortices form, evolve and pair up due to the large velocity gradient in the transverse direction. The large-scale structures that are formed through these mechanisms subsequently break down and form smaller structures or eddies and energy is transferred from the

large structures to the smaller ones. The regular vortex formation and pairing processes are important for the mixing and entrainment of the ambient fluid into the core jet (Ball et al., 2012).

The ability to control the large-scale coherent structures could lead to increased entrainment and mixing which is desirable in most free jet applications. For example, in HVAC applications, it is desirable to have effective mixing of the conditioned air (either hot or cold) and the existing air in a space to make its occupants comfortable. The rapid mixing of the fuel and oxidant is also desirable for combustion application of jets. The control of coherent structures are primarily divided into active and passive means. The active means of controlling these structures include using external energy such as excitation to modify the dynamics of the flow. On the other hand, the passive means use change of initial conditions (e.g. nozzle geometry) to produce modifications in the development of the flow structures (Lee & Baek, 1994).

One way of quantifying mixing in free jets is by estimating the rate of decay of U_c. As the ambient fluid is entrained into the core jet, the two fluids are mixed and hence there is a gradual decay of U_c. Hence a faster velocity decay rate would imply a greater mixing efficiency of a particular jet. The mean velocity data is fitted to the linear equation:

$$\frac{U_m}{U_c} = K_u\left(\frac{x}{d} + C_u\right) \tag{2.1}$$

where K_u (the slope of the plot) is the mean velocity decay rate on the jet centerline, and C_u is the kinematic virtual origin. C_u has not been found to vary in any systematic manner (e.g. Quinn, 1989).

Due to the entrainment of the ambient fluid into the core jet, spreading of the jet in the transverse direction occurs and hence can also be used as a measure of mixing in free jets. The jet spread is typically quantified by using the jet half-velocity width, $y_{0.5}$ (Figure 2.1). This is defined as the transverse distance from the jet centerline to the point where the local streamwise mean velocity has decayed to 50% of its corresponding mean centerline velocity. The jet half-velocity widths are then determined at several streamwise distances from the nozzle exit and then fitted to the linear equation:

$$\frac{y_{0.5}}{d} = K_s\left(\frac{x}{d} + C_s\right) \tag{2.2}$$

where K_s (slope of the plot) and C_s are the spread rate and geometric virtual origins respectively. Values of K_s (as well as K_u) vary depending on the nozzle aspect ratio (for non-circular nozzles), Reynolds number, initial turbulence level and other initial and boundary conditions (e.g. Quinn, 1989).

Non-circular nozzles (e.g. rectangular nozzles with a much smaller aspect ratio than a plane one, elliptical, triangular) have been found to enhance mixing between the core jet and the ambient fluid when compared to their circular counterparts. In jets issuing from rectangular and elliptical nozzles for example, the phenomenon of axis-switching has been identified as the main underlying mechanism for the increased entrainment properties compared with circular and planar nozzles. As the jet evolves, there is more spreading in the minor axis plane of the jet compared with its major axis; as a result, there is a point in the flow where the spread of the jet is equal in both axes and the jet cross section switches orientation (Gutmark & Grinstein, 1999; Ho & Gutmark, 1987). The dynamics and interaction of the large-scale coherent structures are responsible for axis-switching. The azimuthal curvature variation of vortical structures in non-circular nozzles (e.g.

ellipse) causes its non-uniform self-induction and complex three-dimensional deformation. A non-circular (e.g. elliptical) vortex ring moves in such a way that its shape is distorted and does not remain in the same plane; a circular vortex ring however advects downstream without changes in its shape, assuming no azimuthal perturbations (Grinstein, 1997; Hussain & Husain, 1989). According to Hussain & Husain (1989), while an elliptic vortex ring is being advected downstream, its self-induced velocity causes it to deform, causing the major-axis ends to move much faster than the minor-axis ends. As a result, the vortex configuration takes the shape of the seam of a tennis ball. The forward inclination of the major-axis sides folds the initial minor-axis sides. The induced velocity on the minor-axis sides therefore increases and moves outward. Consequently, the vortex finally takes the shape of an ellipse, but this time with the axes switched.

2.2 Previous studies on free jet flows

As already stated, free jet flows have received significant research attention due to its immense practical and fundamental importance. The effects of parameters such as initial turbulence level, aspect ratio (AR) of non-circular nozzles, Reynolds number, type of nozzle and nozzle geometry on the jet flow dynamics have been investigated by various researchers.

A summary of some relevant previous studies on free jet flows is presented in Table 2.1 and Table 2.2. Table 2.1 provides the summary of studies on round and planar nozzles, while Table 2.2 shows those for non-circular nozzles. The tables show the nozzle geometry used, type of nozzle, measurement technique used, Reynolds number at which the flow was studied and flow quantities reported in each of the studies. In the tables, *U*, *V* and *W* represent the streamwise, transverse and spanwise mean velocities respectively; $\sqrt{\overline{u^2}}$, $\sqrt{\overline{v^2}}$ and $\sqrt{\overline{w^2}}$ represent the turbulence intensity in

the streamwise, transverse and spanwise directions respectively; $\overline{u^2}$, $\overline{v^2}$ and $\overline{w^2}$ are the streamwise, transverse and spanwise Reynolds normal stresses whilst $-\overline{uv}$, and $-\overline{uw}$ represent the Reynolds shear stresses. The triple velocity correlations are $\overline{u^3}$, $\overline{u^2v}$, $\overline{uv^2}$, $\overline{vw^2}$, $\overline{v^3}$, $\overline{uw^2}$ and $\overline{w^3}$, S and F represent the skewness and flatness factors; ϕ represents the energy or power spectra; K_u and K_s represent the decay and spread rates respectively and γ represents the intermittency factor. The streamwise and transverse two-point auto-correlation functions are represented by R_{uu} and R_{vv} respectively. The turbulent kinetic energy per unit mass and mass entrainment are represented by k and m_e respectively; Ω_x represents the streamwise mean vorticity, and PDF represents the probability density function. For the measurement techniques, LDA denotes laser Doppler anemometry, HWA refers to hot-wire anemometry, LIF denotes laser-induced fluorescence, PLIF denotes planar laser-induced fluorescence, SPIV denotes stereoscopic particle image velocimetry and PIV refers to particle image velocimetry. For the nozzle types, SC stands for smooth contracting (or contoured), and OP stands for orifice plate nozzles. Finally, Re_j refers to Reynolds number (Re) based on the jet exit velocity, U_j and d; Re_b refers to a Reynolds number based on the exit bulk velocity (U_b) and d; and Re_a refers to Re based on U_j and major axis diameter (a) of an elliptical nozzle.

2.2.1 Round and planar nozzles

As previously stated, round and planar nozzles have received the most research attention when it comes to free jet flows. Consequently, most of our basic understanding of free jet flow phenomena has been deduced from studies involving round and planar jets issuing from smooth contraction nozzles.

Tso & Hussain (1989) studied the dynamics of large-scale coherent vortical motions in the fully developed region of a turbulent round jet. The measurements were made in an air jet using a radial rake of seven x-wires at Re_j = 69,000. The large-scale vortical structures were identified using large-scale vorticity peaks. Structures with axisymmetric, helical and double helical configurations were educed, with the helical structures being the most dominant and hence controlling the flow physics. The helical structures moved radially outward as they move downstream. The simultaneous local ejection of turbulent fluid and the entrainment of the ambient fluid, together with the radially outward movement of helical structures, appeared to be a major means of jet spreading. Intense small-scale turbulent production and mixing was also caused by the shear strain rate acting on the downstream side of the structures.

Wygnanski & Fiedler (1969) studied the flow field of an air jet issuing from a round nozzle. They used hot-wire anemometry to investigate the flow field at Re_j = 100,000. The mean velocity was found to be self-preserving (or self-similar) about 20 nozzle diameters downstream of the nozzle; the streamwise turbulent intensity became self-similar 40 nozzle diameters downstream while the turbulent intensities in the transverse and spanwise directions attain self-similarity 70 diameters downstream of the nozzle exit. The skewness and flatness factors for the fluctuating velocities were observed to deviate from the Gaussian values of 0 and 3 respectively, as one moved away from the jet centerline. For the turbulent energy balance, the dissipation was found to be maximum on the jet centerline; the production was found to be maximum at $y/x \approx 0.052$ (with the maximum shear stress occurring at $y/x = 0.058$) and the production was approximately equal to dissipation at this point. Also, the convection was observed to be maximum on the jet centerline, where it was the largest contributor; at values of y/x greater than 0.117, the convection term became negative.

The role of streamwise vortex structures in the near-field evolution of a round jet was examined by Liepmann & Gharib (1992). Streamwise vortex structures were found to exist in the round jet. These structures grow and combine to form bigger structures as they move downstream. In the braid region (region between primary vortical structures), these structures are amplified which in turn alters the entrainment process, causing more of the ambient fluid to be drawn into the core jet. By using flow visualization and measures of entrainment, they showed that the entrainment process is mainly controlled by streamwise vorticity beyond the potential core region; as the flow evolves downstream, the streamwise vorticity entrains more fluid compared to the azimuthal vorticity.

The effect of Reynolds number on the near-field of a round air jet was investigated by Abdel-Rahman et al. (1996). The centerline velocity was found to decay faster and the potential core length shortened with decreasing Reynolds number, indicating more mixing of the core jet with the ambient fluid. The streamwise component of the turbulence intensity was also observed to increase as *Re* decreased. Profiles of the skewness and flatness factors indicate the jet becomes more intermittent with decreasing *Re;* approach the Gaussian values close to the jet centerline, but start to deviate from the Gaussian values in the transverse direction. The power spectrum of the streamwise fluctuating velocities showed that there is a greater energy content at higher frequencies with increasing *Re*.

Laurence (1955) performed measurements of turbulence intensity, the streamwise and transverse scales and the spectra in a free round jet. The experiments were performed at Re_j = 75,000 – 700,000 and exit Mach numbers between 0.2 and 0.7. The results showed that the turbulent

Table 2.1: Summary of some previous studies on round and planar jets.

Author(s)	*Nozzle Geometry*	*Nozzle type*	*Technique*	*Re*	*Quantities*
Abdel-Rahman, et al. (1996)	Round	SC	LDA	Re_j = 1,400-20,000	U, $\sqrt{\overline{u^2}}$, S, F, ϕ
Namer & Ötügen (1988)	Plane	SC	HWA & LDA	Re_j = 1,000-7,000	U, R_{uu}, ϕ, $\sqrt{\overline{u^2}}$, K_u, K_s
Goldschmidt & Bradshaw (1981)	Plane	SC	HWA	Re_j = 27,000	U, $\sqrt{\overline{u^2}}$, K_u, K_s
Wygnanski & Fiedler (1969)	Round	SC	HWA	Re_j = 100,000	U, V, $\sqrt{\overline{u^2}}$, γ, $\sqrt{\overline{v^2}}$, $\sqrt{\overline{w^2}}$, S, $-\overline{uv}$, F, R_{uu}, $\overline{w^3}$, R_{uv}, $\overline{u^2v}$, $\overline{uw^2}$, $\overline{uv^2}$, $\overline{vw^2}$, $\overline{v^3}$, *Budget terms*
Gutmark & Wygnanski (1976)	Plane	SC	HWA	Re_j = 30,000	γ, U, V, $\sqrt{\overline{u^2}}$, $\sqrt{\overline{v^2}}$, $\sqrt{\overline{w^2}}$, $\overline{v^3}$, $-\overline{uv}$, R_{uu},, $\overline{u^3}$, $\overline{uv^2}$, $\overline{uw^2}$, $\overline{u^2v}$, $\overline{vw^2}$, F, *Budget terms*
Laurence (1955)	Round	SC	HWA	Re_j = 75,000 - 700,000	U, ϕ, R_{uu}, R_{vv}, $\sqrt{\overline{u^2}}$, $\sqrt{\overline{v^2}}$
Mi, et al. (2007)	Round	OP	PIV	Re_b = 72,000	U, U_i, $\sqrt{\overline{u^2}}$, $\sqrt{\overline{v^2}}$, m_e, $-\overline{uv}$, $\overline{u^2}$, $\overline{v^2}$
Hussein et al. (1994)	Round	SC	HWA & LDA	Re_j = 100,000	U, K_u, $\overline{u^2}$, $\overline{v^2}$ $\overline{w^2}$, $\overline{v^3}$, $-\overline{uv}$, $\overline{u^3}$, $\overline{uv^2}$, $\overline{uw^2}$, $\overline{u^2v}$, *Budget terms*

intensity was at its maximum a distance of about 0.5d from the centerline and decreases with increasing Mach and/or Reynolds number. The streamwise and transverse scales were observed to be nearly independent of Mach and/or Reynolds number and varied proportionally with downstream distance from the nozzle exit.

Hussein et al. (1994) studied the velocity field of a high Reynolds number (Re_j = 100,000) round jet using HWA and LDA. The mean velocity became self-similar after 30 nozzle diameters. The off-center peak of axial Reynolds normal stress observed was attributed to the strong off-axis peak in the production of turbulence energy by the Reynolds stress working against the mean shear. The energy balance showed that in the core region the mean convection and pressure diffusion terms are dominant while the production is small; these terms mainly balance the dissipation. However, in the flow region away from the core region, the balance is primarily between production and dissipation.

Mi et al. (2007) also investigated a round jet produced from an orifice plate nozzle using PIV. The instantaneous velocity vectors, contours and streamlines revealed that primary coherent structures exist in the near-field of both the SC and OP jet, but occurs more frequently in the orifice plate jet. The self-similarity of the mean flow of the OP jet was attained for $x \geq 8$, while the turbulent field did not attain self-similarity for the measurement range considered (i.e. $0 \leq x/d \leq 16$).

The plane jet was investigated by Gutmark & Wygnanski (1976) using HWA at Re_j = 30,000. The plane jet was found to also exhibit self-preserving features. For example, the turbulent intensities on the jet centerline reached an asymptotic value (and hence self-preserving state) approximately

30 slot widths downstream from the nozzle exit. When compared to the round jet, the plane jet showed a similar distribution of the mean velocity, and turbulent quantities (e.g. intermittency factor and turbulent intensities). The magnitude of the streamwise turbulent intensity was also greater than intensity in the other directions. In terms of the energy budget, the dissipation was also found to be greater in the central region of the jet compared to its value away from the jet centerline. The production term was highest in the shear layer and occurred approximately at the location where the shear stress is maximum. The dominant budget term in the central portion of the jet is convection by the mean flow, and these observations are similar to the conclusions drawn from the energy budget of the round jet.

Goldschmidt & Bradshaw (1981) studied the dependence of the spreading rate on the exit turbulence level in a plane jet. It was observed that the velocity decay rate was not as sensitive to changes in exit turbulence levels as the spread rate. The spreading rate however, was observed to increase with exit turbulence level from 0.112 for an exit turbulence level of 0.59% to 0.123 for an exit turbulence level of 2.23%.

The effects of Reynolds number on the flow field of a turbulent plane jet was also investigated by Namer & Ötügen (1988). The range of *Re*, defined by the jet exit conditions varied from 1000 to 7000. The results showed that there was no *Re* dependence on the average size and number of large-scale structures. It was however noted that the relative energy content (or strength) of the large eddies decreased with increasing *Re*. Consequently, the spread rates and centerline velocity decay rate decreased with increasing *Re*. The turbulent flow also exhibited higher levels of streamwise turbulent intensity on the jet centerline for lower Reynolds numbers.

2.2.2 Non-circular nozzles

As previously stated, jet flows from non-circular nozzles have the potential to provide enhanced mixing between the jet flows and the ambient fluid; and as a result, has received significant research attention in the recent past.

Ho & Gutmark (1987) used a small aspect ratio elliptic jet (AR = 2) as a passive means of controlling coherent structure formation and hence increased entrainment compared to a round or plane jet. The authors argued that in other studies involving larger aspect ratios, the entrainment properties were not significantly different from those in plane jets, hence the motivation to use a smaller aspect ratio jet. The measurements were made using HWA at a *Re* based on major axis diameter (*a*) and jet exit velocity of 78,000. The self-induction of the asymmetric coherent structure caused azimuthal distortions and this was responsible for entraining large amounts of ambient fluid into the core jet (three to eight times greater than the entrainment observed in a round or plane jet). The axis-switching phenomenon occurred three times within the measurement range ($0 \leq x/r_1 \leq 40$, where r_1 is the major axis radius) due to the self- induction of the elliptic vortex ring. As a result, in the near-field, a large entrainment of the elliptic jet was observed in the minor axis while the major axis entrainment was similar to that of a round or plane jet.

A turbulent elliptic jet (AR = 2) was also studied by Yoon & Lee (2003) for Re_b = 10,000 using SPIV. The first axis-switching of the jet was observed at x/d = 2. The total entrainment rate of the elliptic jet was estimated to be about 1.5% greater than that of a comparable round jet. The entrainment in the elliptic jet was observed to be more intense on the minor axis of the jet due to

the self-induction of the elliptic vortical structure in the near-field; this results in the fast expansion of the jet along this axis.

Lee & Baek (1994) studied the effect of aspect ratio on the flow development in the near-field of an elliptic jet. The axis-switching phenomenon was observed in all the elliptic jets studied. It was observed that as the aspect ratio of the elliptic jet increased, the location where the first axis-switching occurred moved further downstream of the nozzle exit (i.e. x/d = 2, 3.2 and 6.5 for AR = 2, 4 and 8 respectively). This trend of increasing axis-switching location with aspect ratio was also observed by Krothapalli et al. (1981) for a rectangular jet. For the same aspect ratio however, the axis-switching location for a smooth contraction nozzle occurred further downstream than for an orifice plate nozzle. For example, for AR = 2, the axis-switching location for a SC elliptic jet (Ho & Gutmark, 1987) occurred at x/d = 5 compared to x/d = 2 in their study. Lee & Baek (1994) also observed that in the near-field of the flow, the aspect ratio 2 nozzle exhibited a higher mean velocity decay, turbulence intensity and Reynolds shear stress level. This implied that there was more entrainment and mixing in an aspect ratio 2 nozzle compared to other aspect ratios (4 and 8) as well as the round jet.

The rectangular jet (AR = 2 and 10) was investigated by Quinn (1991). Saddle-shaped mean streamwise velocity profiles were present in the major axis plane of the aspect ratio 10 jets; this was however absent in the rectangular jet with an aspect ratio 2. The rectangular jet of aspect ratio 10 also produced higher values of the Reynolds shear stress and turbulent kinetic energy in its near-field.

Table 2.2: Some previous studies on non-circular jets

Author(s)	*Nozzle Geometry*	*Nozzle type*	*Technique*	*Re*	*Quantities*
Ho & Gutmark (1987)	Ellipse (AR = 2)	SC	HWA	Re_a = 78,000	*U, V, W,* ϕ, m_e, $\sqrt{\overline{u^2}}$, $-\overline{uv}$, $\sqrt{\overline{v^2}}$, $\sqrt{\overline{w^2}}$, $-\overline{uw}$
Lee & Baek (1994)	Round, & Ellipse (AR = 2, 4, 8)	OP	LDA	Re_j = 40,000	*U, V, W,* $\sqrt{\overline{u^2}}$, *k,* $-\overline{uv}$,$-\overline{uw}$
Quinn (1991)	Rectangle, (AR = 2, 10)	OP	HWA	Re_j = 208,000	*U, k,* $-\overline{uv}$, $-\overline{uw}$, $\overline{u^2v}$, $\overline{uv^2}$
Yoon & Lee (2003)	Ellipse (AR 2)	OP	SPIV	Re_b = 10,000	*U, V, W, k,* $\sqrt{\overline{u^2}}$, $\sqrt{\overline{v^2}}$, $\sqrt{\overline{w^2}}$, $-\overline{vw}$
Mi & Nathan (2010)	Round, Square, Ellipse & Rectangle (AR 2), Cross, Star Triangle	OP	HWA	Re_b = 15,000	*U,* $\sqrt{\overline{u^2}}$, ϕ, *PDF, length scales*
Hu et al. (2000)	Round, Lobed	SC	PLIF & PIV	Re_j = 3,000 & 6,000	*U, k,* Ω_x, $\sqrt{\overline{v^2}}$, $\sqrt{\overline{w^2}}$

Mi & Nathan (2010) reported the centerline evolution of nine turbulent air jets issuing from differently shaped nozzles using HWA. All the nozzles studied had the same equivalent diameter and the measurements were made for Re_b = 15,000. The mean velocity decayed faster and the turbulence intensity was higher in the near filed of the asymmetric nozzles (e.g. equilateral and isosceles triangle) compared to the reference round nozzle, implying increased overall entrainment rate for these nozzles. This was especially the case in the isosceles triangular jet, whose near-field structure was deduced to be the most three-dimensional and hence possessing the greatest mixing

capacity. The centerline evolutions of the length scales (i.e. integral, Taylor and Kolmogorov scales) showed an increase in the scales with streamwise distance. However, the nozzle shape did not seem to affect the size of the turbulent structures. The integral scale was also found to be 5 to 6 times greater than the Taylor microscale but greater than the Kolmogorov scale by a factor of 150 to 250.

The characteristics of lobed jets were investigated by Hu et al. (2000) using PLIF and PIV. The jet issuing from the lobed nozzle showed a faster decay of centerline velocity and a larger shear layer growth, compared to a round nozzle having the same exit area. This implied greater mixing in the lobed jet and this occurred within the first two nozzle diameters of the flow. Azimuthal perturbations (which are enhanced by streamwise vorticity) produced by the lobed nozzle configuration, enhanced the transfer of energy and vorticity from the larger scales to the smaller ones. Small-scale turbulence was also generated by the reduction in scale of the spanwise vortices due to action of the streamwise vorticity. These processes resulted in the enhanced mixing of the ambient fluid with the core jet in the lobed nozzle configuration.

2.3 Summary

The free jet flow field has been extensively studied by various researchers. Initial conditions such as the specific nozzle geometry (e.g. round, plane and triangular nozzles), type of nozzle (e.g. smooth contraction nozzles and long pipes), exit Reynolds number, aspect ratio for non-circular nozzles and exit turbulence levels affect the mixing characteristics of the free jets. Jets from round and planar nozzles issuing from smooth contracting nozzles have been the most extensively studied and the results have provided insight into the mechanisms responsible for entrainment. Despite the

research attention that free jets have received, majority of these studies have been conducted at relatively high Reynolds numbers (where *Re* does not affect flow characteristics of the jet). There is therefore the need to examine free jet flows at relatively low *Re* for a wide range of nozzles to advance our understanding of these type of flows.

CHAPTER 3

3 EXPERIMENTAL SETUP AND MEASUREMENT PROCEDURE

This chapter describes the experimental setup and the measurement procedure used for the velocity measurements in this study. A description of both the water jet and air jet facilities used are provided, together with a description of the PIV system. Finally, a summary of the test conditions is also presented. It should be noted that the main reference for this section is the PIV user manual supplied by Dantec Dynamics.

3.1 Experimental setup

3.1.1 Water jet facility

Figure 3.1 shows the experimental setup that was employed in the water jet study. The experiments were conducted in an open recirculating water channel which consists of a flow settling chamber for flow conditioning, test section, centrifugal pump, variable speed drive, piping and valves, supporting framework and a filtering system. The test section has dimensions 2500 (length) × 200 (width) × 200 (height) mm. The side walls of the channel were made from smooth acrylic to facilitate optical access. The recirculating flow is driven by the pump through the flow settling chamber which is at the inlet of the water channel. A series of steel plates and honey combs are fitted within the settling chamber to condition the flow by providing flow uniformity and reducing the turbulence levels before entering a contraction section. The area contraction ratio is six-to-one and the presence of the contraction causes the flow to accelerate thereby further reducing the turbulence levels of the flow. The variable speed drive regulates the speed of the motor that drives the pump while the filtering system is used to remove contaminants from the system's water when required.

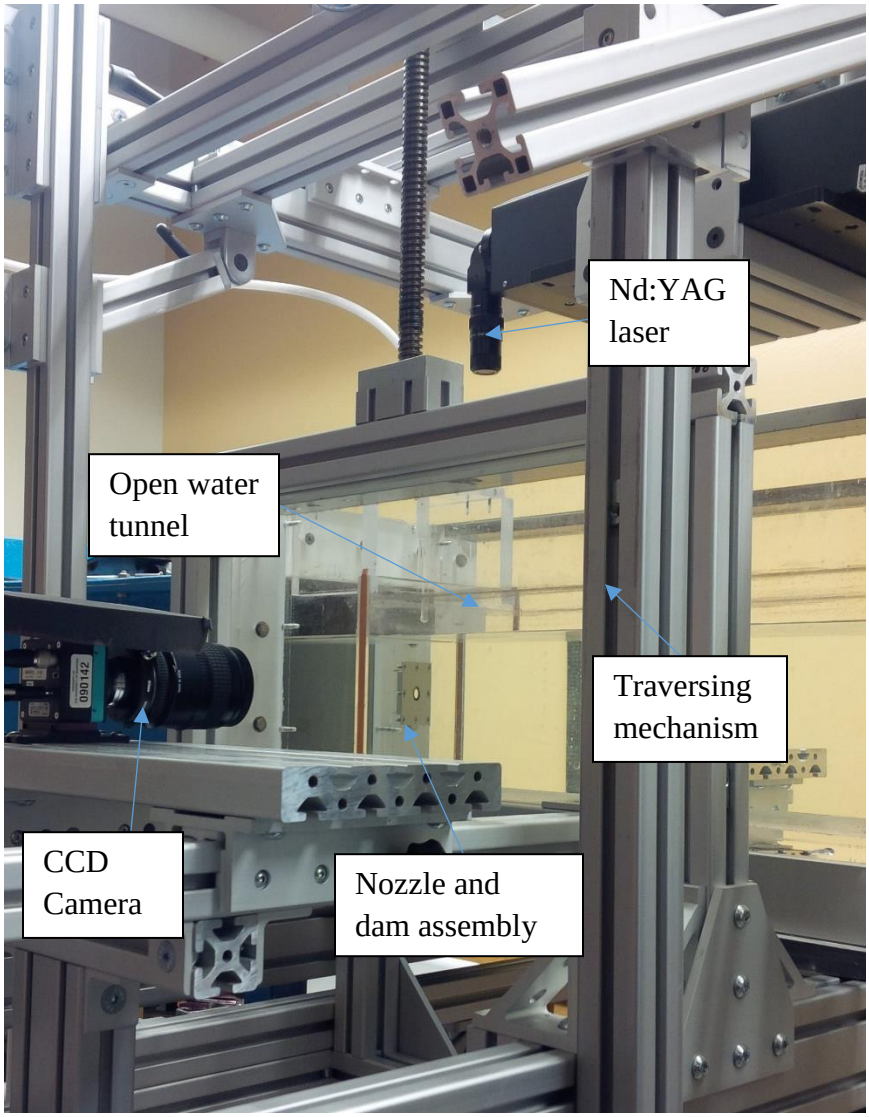

Figure 3.1: Experimental setup for water jet study

3.1.1.1 Nozzle assembly

The nozzle assembly for the water jet experiments consists of a dam and nozzle plates. A series of interchangeable nozzles were used in this study and the different nozzles shapes studied are shown in Figure 3.2. The nozzle plates were made of stainless steel of thickness 1 mm (since a smaller thickness produces flow conditions that closely mimic an orifice plate nozzle) and each plate has dimensions 60 (length) × 60 (width) mm. The nozzle assembly was mounted 120 mm from the

inlet of the water channel. The dam assembly was tight-fitted into the sides of the water tunnel. The round (RD) nozzle is of diameter 9 mm and all other nozzle shapes had the same opening area (or equivalent diameter, *d*) as the round case (i.e. opening area of 63.62 mm^2). The rectangular (Rect) and elliptical (Elp) nozzles have an aspect ratio of 2. In the case of the flower (Flwr), rectangular and elliptical nozzles, measurements were made in both the major axis plane (plane parallel with the horizontal) and the minor axis plane (plane parallel with the vertical) and are denoted as Maj and Min respectively (as shown in Figure 3.3).

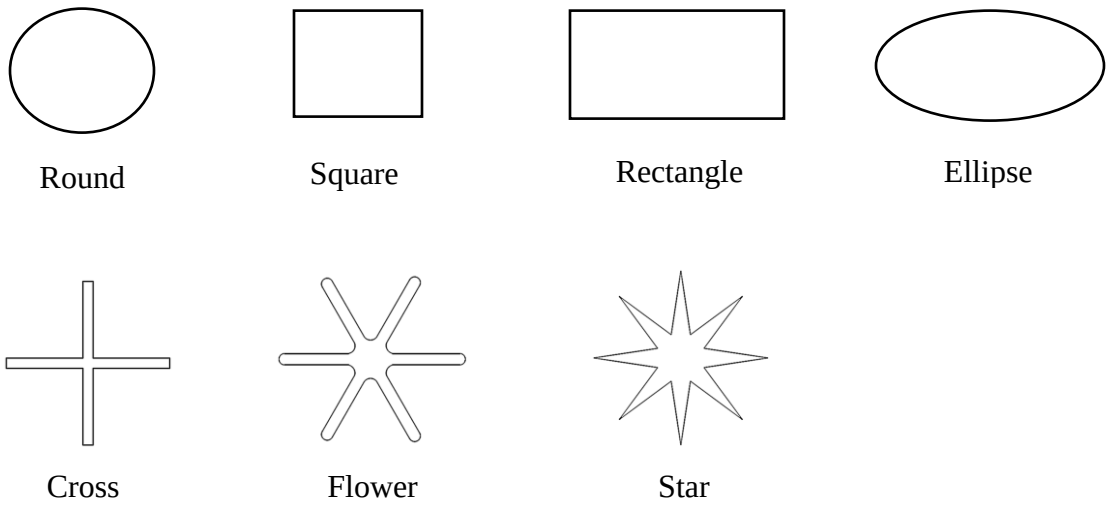

Figure 3.2: Nozzle geometries used in water jet study

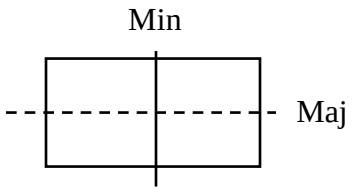

Figure 3.3: Rectangular nozzle showing the major and minor planes

The Cartesian coordinate system was adopted in this study: the streamwise and transverse directions are denoted by x and y respectively and the origin of the x-y plane is at the centerline of the nozzle exit. Also, the velocity measurements measured on the jet centerline are denoted as U_c, the jet centerline velocity.

3.1.2 Air jet facility

The air jet facility is shown in Figure 3.4. It consists of three main sections; the plenum/settling chamber, test chamber and outlet section. The settling chamber consists of several perforated stainless steel plates and a polycarbonate honeycomb to break down the large-scale turbulence and make the flow uniform. The test chamber has dimensions 1100 (length) × 734 (width) × 534 (height) mm. The side and top walls were made of transparent acrylic to facilitate optical access. Compressed air with a maximum air pressure of about 650 kPa at ambient temperature was supplied to the air jet facility which contains various flowmeters, pressure gauges, valves and pressure reducing devices. Symmetric piping spreads the air flow evenly into the plenum, through interchangeable nozzles, the test chamber and finally through the outlet section. Before the air reaches the plenum, it passes through the aerosol generator that controls the amount of aerosols introduced into the flow. The outlet section consists of a fan driven filtration system that draws the air exiting from the test chamber, through filters before exhausting into the room.

3.1.2.1 Air jet nozzles

A series of interchangeable nozzles are also used for the air experiments; however, only the round, cross and rectangular (AR = 2) nozzles are used based on the results of the water jet experiments. The nozzles also have an equivalent diameter of 9 mm. The nozzles have a 20 mm long straight

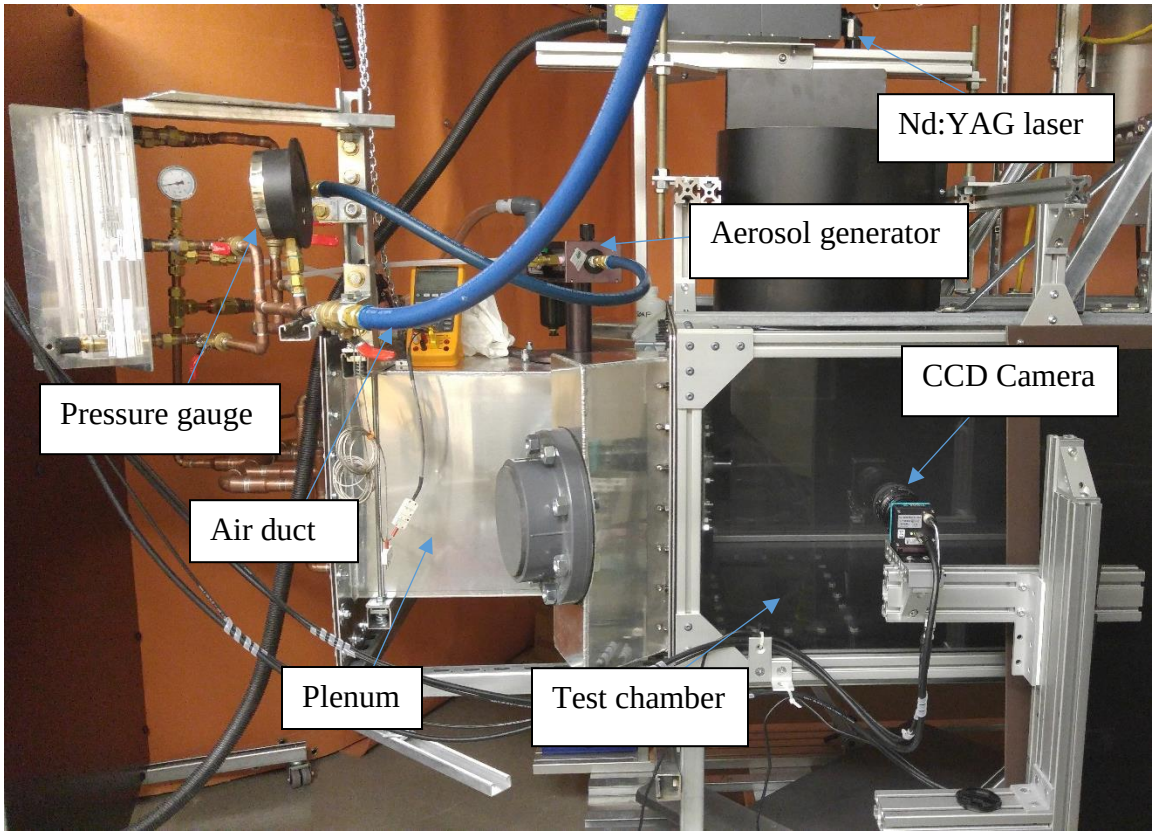

Figure 3.4: Air jet experimental setup

section, followed by a sharp linear contraction of length 6 mm, leading to the opening of each nozzle.

3.2 PIV system and measurement procedure

A particle image velocimetry (PIV) system was used to perform velocity measurements in the streamwise-transverse plane (*x*-*y*) of the jet flow. PIV is a whole-field non-intrusive velocity measurement technique that measures instantaneous velocity vectors simultaneously at multiple locations within the flow field. A two-component two-dimensional (2C-2D) PIV system was employed in the present study to measure the instantaneous velocity field of the 2D flow domain.

The main components of a PIV system consists of a laser source to illuminate the flow field, a camera used to capture the flow field (as shown in both Figure 3.1 and Figure 3.4) and a data acquisition system to acquire and process the images obtained. The flow is first seeded with tracer particles which are assumed to follow the fluid motion. The flow field is then illuminated by two pulses of laser sheet separated by a time delay, Δt. A couple-charged device (CCD) camera captures the light scattered by the tracer particles and two successive images are recorded. The images are then divided into grids and each grid is called an interrogation area (IA). A numerical correlation algorithm is then applied to statistically determine the local displacement vector (Δs) of particles between the first and second image for each IA. The velocity vector for each IA is then obtained by dividing Δs by Δt. This process is then repeated for all the IA's to obtain the velocity vector map of the entire flow field.

3.2.1 Light source

Since the whole-field measurements are made during PIV measurements, a high power laser is required to illuminate the flow to enable the camera capture the sideways light scattered by the tracer particles. A high intensity pulse laser is also required to freeze the motion of the particles during image capturing. Frequency doubled neodymium-yttrium-aluminum-garnet (Nd:YAG) lasers are normally used for PIV measurements because they provide monochromatic light with high intensity illumination. The light emitted by the laser is passed through a lens system to create a plane sheet of light to illuminate the region of interest. The length and width of the light sheet can be adjusted to the required field of view.

3.2.2 Seeding particles

The seeding particles should be distributed homogeneously throughout the flow, be large enough to scatter sufficient light to be detected by the camera; but small enough to follow the flow motion "faithfully" (Westerweel et al., 1996). This is because PIV measures the velocity of the particle and not the fluid velocity; therefore, it is essential that the particles have certain hydrodynamic properties to ensure they follow the fluid motion "faithfully". The settling velocity (v_s) can be estimated from Stokes drag law for flow around a sphere under gravity and is given by:

$$v_s = \frac{(\rho_p - \rho_f) g d_p^2}{18 \mu_f} \tag{3.1}$$

where ρ_p is the particle density, ρ_f is the fluid density, g is the acceleration due to gravity, d_p is the diameter of the particle and μ_f is the dynamic viscosity of the fluid. It should be noted that particles with negligible settling velocity are desirable. The response time (t_r) of the seeding particles is also estimated; it is a measure of the tendency of the particles to reach the same velocity with the fluid, and t_r is given by (Raffel et al., 1998):

$$t_r = \rho_p \frac{d_p^2}{18 \mu_f} \tag{3.2}$$

Additionally, the wavelength of radiation, refractive index, shape and size of the particles also affect its ability to scatter light. Commonly used seeding particles include hollow glass spheres, silver coated hollow glass spheres and fluorescent polymer particles for liquid flows and different kinds of oils for gaseous (e.g. air) flows.

3.2.3 Recording medium

The CCD camera is the most commonly used recording medium for PIV applications. This is because it has higher frame rates and the possibility of on-line analysis compared with

photographic film cameras. One drawback, however, is that photographic film cameras do have higher resolutions compared to the CCD camera. The CCD camera consists primarily of a CCD sensor, which comprises an array of detectors called pixels. High-performance progressive scan interline CCD chips are also used in the CCD camera. The chip contains an array of photosensitive cells and an equal number of storage cells. After the first image is captured (after the first laser pulse is triggered), it is immediately transferred from the photosensitive cells to the storage cells. This enables the photosensitive cells to be ready to store the second image (after the second laser pulse is triggered). As a result, the storage cells contain the first image and the photosensitive cells the second image. Both images are then transferred sequentially from the camera to the computer for storage. This allows Δt to be reduced to less than 1 μs.

3.3 PIV settings for current study

3.3.1 Water jet experiment

In the current study, the flow was seeded using 10 μm silver coated hollow glass spheres having a specific gravity of 1.4. These particles are large enough to scatter sufficient light for the CCD camera to record. The settling velocity (from Equation 3.1) and the response time (from Equation 3.2) of the particles were estimated as $v_s = 2.18 \times 10^{-5}$ m/s and $t_r = 7.78 \times 10^{-6}$ s respectively. Since both the settling velocity and the response time were small compared with the streamwise mean velocities measured and the sampling time respectively, this implies that the particles will follow the fluid motion “faithfully”.

The flow field was illuminated with a New Wave Solo Nd:YAG double-pulsed laser that emits green light up to a maximum of 120 mJ/pulse at 532 nm wavelength and 15 Hz repetition rate. The

laser sheet was aligned with the mid-span of the channel and a 12-bit couple-charged device (CCD) camera with a 2048 pixel × 2048 pixel array and 7.4 μm pixel pitch was used to capture the flow field. The field of view used for all the planes of measurement was set to 65 mm × 65 mm. Based on a convergence test (see Appendix), a sample size of 6000 image pairs was acquired at a sampling rate of 2.5 Hz for each measurement plane. The time between successive image pairs was 0.4 s and it took 2,400 s to acquire the sample size. The integral time scale, T, was estimated by dividing the integral length scale, L, (obtained from two-point correlation function at different streamwise locations) by the local maximum streamwise turbulent intensity. It was determined that T varied from 0.01 s to 0.093 s depending on the test condition. Thus the time of 0.4 s (time between successive image pairs) is about two orders of magnitude larger than the integral time scale and therefore sufficiently large to obtain successive image pairs that are uncorrelated.

3.3.2 Air jet experiment

The air jets were seeded with olive oil with mean diameter of 1 μm. The settling velocity and response time were estimated as 4.68×10^{-5} m/s and 4.78×10^{-6} s respectively (from Equation 3.1 and Equation 3.2). Again the settling velocity and response time were small compared with the streamwise velocities and the sampling time, implying that the particles follow the flow "faithfully".

The flow field was illuminated with the same laser and images captured with the same CCD camera as in the water jet experiments. Due to constraints of the air jet facility, the smallest possible field of view was 100 mm × 100 mm and this field of view was used for all the measurement planes. Here, 6000 image pairs were acquired at a sampling frequency of 2.5 Hz in each plane. The

acquisition time for each sample size was 2400 s, and the integral time scale varied from 0.002 s to 0.017 s. The time between successive image pairs was therefore 0.4 s and was again found to be about two orders of magnitude larger than T, implying that successive image pairs were uncorrelated.

3.3.3 PIV post processing

The images captured were post processed using adaptive correlation option of a commercial software (DynamicStudio version 3.40) supplied by Dantec Dynamics. The adaptive correlation algorithm uses a multi-pass fast Fourier transform cross-correlation algorithm to determine the average particle displacement within an interrogation area. A one-dimensional Gaussian peak-fitting function was used to determine particle displacement with subpixel accuracy. The IA size for the adaptive correlation was set to 32 pixels × 32 pixels with 50% overlap in both the x and y directions for both the water and air experiments. The vector spacing was $0.057d$ and $0.087d$ for the water and air jet experiments, respectively. In the air experiments, for example, the Taylor microscale (λ) and the Kolmogorov length scale correspond to $0.1d \sim 0.3d$ and $0.005d \sim 0.01d$ respectively. During the data acquisition, precautionary measures such as ensuring a maximum particle displacement of one quarter of the interrogation area (8 pixels) were observed to ensure a good signal-to-noise ratio. This is because the particles to be tracked must stay within the same IA during the illumination of the flow. As a result, keeping the maximum displacement at 8 pixels helps to keep the number of particles that leave an IA to a minimum. With a maximum displacement of 8 pixels and a 0.1 sub-pixel accuracy, the dynamic range was 80.

3.4 Test conditions

A total of seven (7) nozzles (as shown in Figure 3.2) were studied in the water jet facility. Based on $U_j \approx 0.63$ m/s and d, the Reynolds number was kept constant at $Re_j \approx 5{,}670$ to facilitate comparison of the results to be obtained. The data was acquired in 3 measurement planes, extending from the nozzle exit to $x/d = 21$.

For the air experiments, the round nozzle was used as a reference nozzle, while the cross and rectangular nozzles were chosen due to their mixing performance (results from the water experiments). The Reynolds number based on the jet exit velocity ($U_j \approx 16.7$ m/s) and the equivalent diameter of 10,000 was also kept constant to facilitate comparison. Data was acquired in 3 measurement planes extending from $0 \leq x/d \leq 30$.

3.5 Measurement uncertainty

A measurement uncertainty analysis was performed following the procedure outlined by Forliti, et al., 2000 and Coleman & Steele, 1995. The analysis involved identifying and quantifying both the bias and precision errors of the PIV measurement. For PIV measurements, sources of error include particle response to fluid motion, light sheet positioning, size of interrogation area and laser pulse timing.

Due to the size of the interrogation area and the Gaussian peak-fitting function, the large sample size and the filtering used to calculate the instantaneous vector maps, the uncertainties in the mean velocity, turbulent intensity and Reynolds stresses and energy budget terms at 95% confidence

level were estimated as ±2%, ±7%, ±10% and ±15% respectively. Detailed uncertainty analysis in this study are presented in the Appendix.

CHAPTER 4

4 RESULTS AND DISCUSSION

This chapter presents the mean and turbulent flow characteristics of the various jets studied. The discussion is divided into two parts. The first section focuses on results obtained from the water jet experiments and include the mean velocity decay, the jet spread rate as well as mass entrainment. The second section presents results from the air jet experiments and were based on the nozzles with the best mixing performance from the water jet experiments. The best nozzle configurations were further analyzed using contours as well as one-dimensional profiles of the turbulent intensities, Reynolds stresses, and two-point auto-correlation. Some of the terms of turbulent kinetic energy budget were also evaluated to examine the flow features of these jets.

4.1 Water jets

This section presents the results from all the nozzles studied in the water tunnel. The nozzles are the round (RD), square (SQ), cross, flower (Flwr), star, rectangular (Rect) and elliptic (ELP) nozzles of aspect ratio (AR) 2.

4.1.1 Mean streamwise velocity development

The development of the jet is usually characterized by the decay of the streamwise velocity on the centerline. The jet centerline velocities (U_c) for the various nozzle geometries normalized by their respective exit velocities (U_j) are shown in Figure 4.1 (a). In each case, the jet centerline velocity increases from the exit till it reaches a maximum value (U_m) due to the well-known vena contracta effect. U_m occurs at $x/d \approx 0.5$ for the majority of the jets and there is no apparent effect of nozzle geometry (as shown in Figure 4.1 a). After the occurrence of the maximum velocity, the centerline

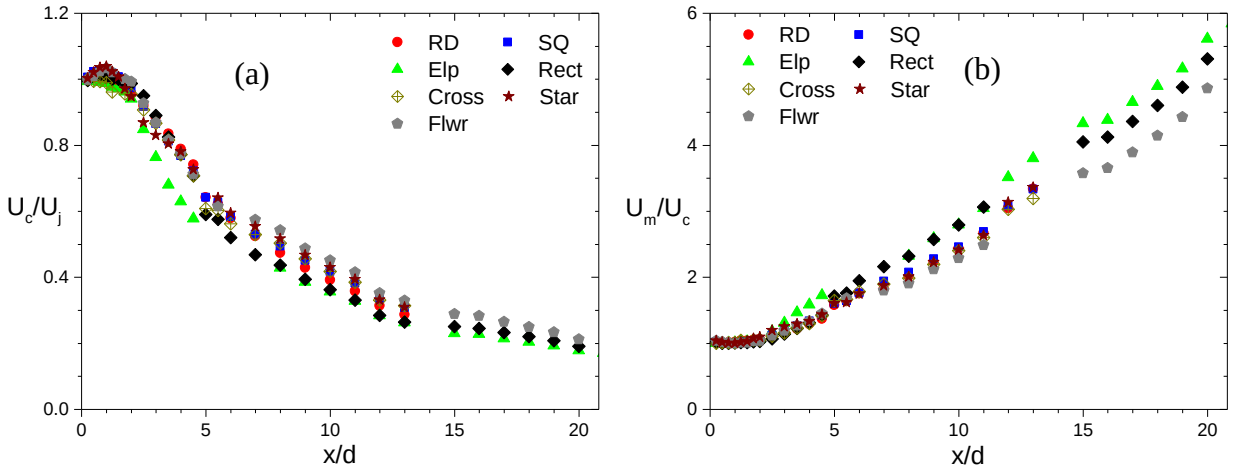

Figure 4.1: Variation of the mean streamwise velocity decay on the jet centerline

velocity decays with increasing streamwise distance due to the entrainment of the ambient fluid into the core jet.

In order to quantify the velocity decay, the variation of the normalized streamwise centerline velocity (U_m/U_c) with streamwise distance was plotted (Figure 4.1 b). The data is then fitted to Equation 2.1. The decay rates (K_u) for all the jets, which were obtained from the slope of each plot, are summarized in Table 4.1. Some values from previous studies are also included in Table 4.1 for comparison. The values of K_u for the round and square nozzle are almost identical and lower when compared with all the other non-circular nozzles. For example, the decay rate for the elliptical nozzle is 18% greater than the reference round nozzle. The greatest decay rates are observed in the elliptical and rectangular nozzles (AR = 2) implying that the jets produced from these nozzles mix faster with the ambient fluid compared with the other nozzles studied. Although the values of K_u for the different nozzles studied by Mi & Nathan (2010) were observed to be similar, the shorter unmixed-core length of the non-circular nozzles implied greater entrainment in the near-field of these jets compared to the round jet.

Table 4.1: Mean velocity decay parameter

Study	*Jet nozzle*	K_u	*Re*
Present	Round	0.213	Re_j = 5,670
	Square	0.211	
	Cross	0.228	
	Flower	0.231	
	Star	0.234	
	Rectangle (AR = 2)	0.230	
	Ellipse (AR = 2)	0.252	
Mi & Nathan (2010)	Round	0.208	Re_b = 15,000
	Square	0.203	
	Cross	0.201	
	Rectangle (AR = 2)	0.200	
	Ellipse (AR = 2)	0.202	

4.1.2 Jet width and spreading rate

The spreading of the jet was quantified using the conventional half-velocity width ($y_{0.5}$) and other velocity widths. These other velocity widths are defined as the distance from the jet centerline to the point where the local streamwise mean velocity has decayed to 90% ($y_{0.9}$), 75% ($y_{0.75}$), 25% ($y_{0.25}$) and 10% ($y_{0.1}$) of its corresponding mean velocity as shown in Figure 4.2. The various jet velocity widths for each nozzle were then plotted against the streamwise distance and fitted to the linear equation:

$$\frac{y_b}{d} = K_s\left(\frac{x}{d} + C_s\right) \tag{4.1}$$

where y_b refers to the various velocity widths (i.e. $y_{0.9}$, $y_{0.75}$, $y_{0.5}$, $y_{0.25}$, $y_{0.1}$), K_s is the spread rate and *Cs* is the geometric virtual origin. The values of K_s obtained were then plotted against their corresponding jet widths as shown in Figure 4.3. In the case of the rectangular, elliptical and flower nozzles, the geometric mean (avg) was used to facilitate comparison with the other nozzles; it is defined as the square root of the product of the velocity widths in the major and minor planes. For

all the nozzles studied, the values of K_s increase from close to the jet centerline ($y_{0.9}$) to their largest value further away ($y_{0.1}$). This is because the entrainment of the ambient fluid into the core jet results in the spread of the jet in the transverse direction and the effects of mixing are more pronounced close to the edge of the jet. The main observation is that the rectangular and elliptical nozzles spread faster than all the other nozzles studied. This is due to the axis-switching phenomenon which results from the evolution of elliptical and rectangular vortex structures. In the elliptic jet, for example, as the major axis side of the vortex rings shrinks, the minor axis side expands and vice versa; this process entrains fluid from the ambient into the core jet and aids in the mixing of the two fluid streams (Hussain & Husain, 1989). The least spreading (i.e. smallest value of K_s) is observed in the round and square nozzles. For example, for the conventional half-velocity width ($y_{0.5}$), K_s for the rectangular nozzle is 61% greater than that for the square nozzle, while the elliptical nozzle is 45% greater than the round nozzle. All the other non-circular nozzles (cross, flower and star shapes) also spread faster than the square and round nozzles and this implies that they would entrain more ambient fluid and more mixing would occur, which is desirable in most applications. For all other velocity widths studied, this trend was conserved, i.e., the other non-circular nozzles spread faster than the round and square nozzles.

The location at which axis-switching occurs is typically deduced from the plot of the jet half-velocity width in both the major and minor axis planes for the rectangular and elliptical nozzles. In the present study, the other velocity widths evaluated were also used to determine this axis switching location and are shown in Figure 4.4. The axis-switching location is estimated as x/d = 1.25 and x/d = 2.3 for the elliptical and rectangular nozzles respectively. The flower nozzle also

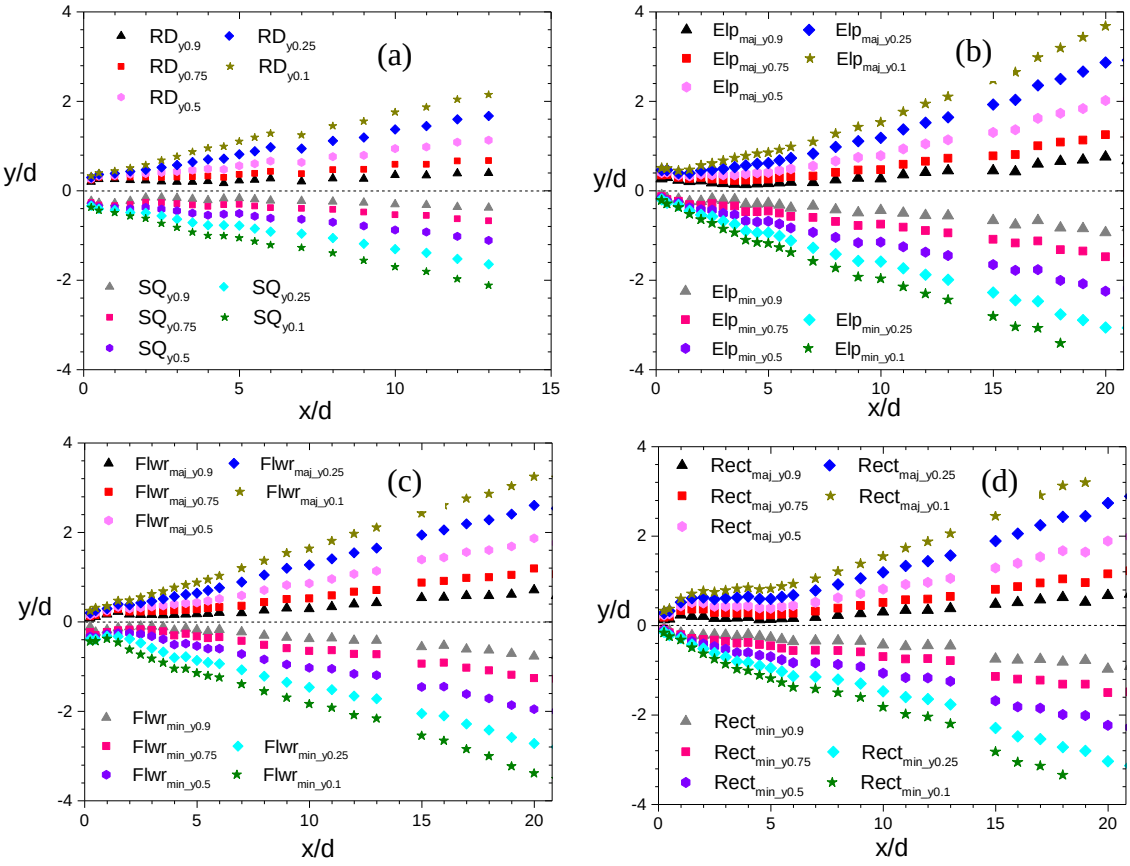

Figure 4.2: Variation of jet velocity widths for the various nozzle geometries

exhibited the axis-switching phenomenon (not shown) and its location is estimated as $x^* = 1.1$. It should be noted that the axis-switching location remained constant regardless of the jet velocity width that was used to estimate it.

The variation of the jet shear layer thickness with streamwise direction (not shown) was also estimated in the present study. The jet thickness was evaluated by subtracting the jet width closest to the jet centerline ($y_{0.9}$) from the jet velocity width furthest away from the jet centerline ($y_{0.1}$). The difference between the jet velocity widths was then plotted with streamwise distance for each

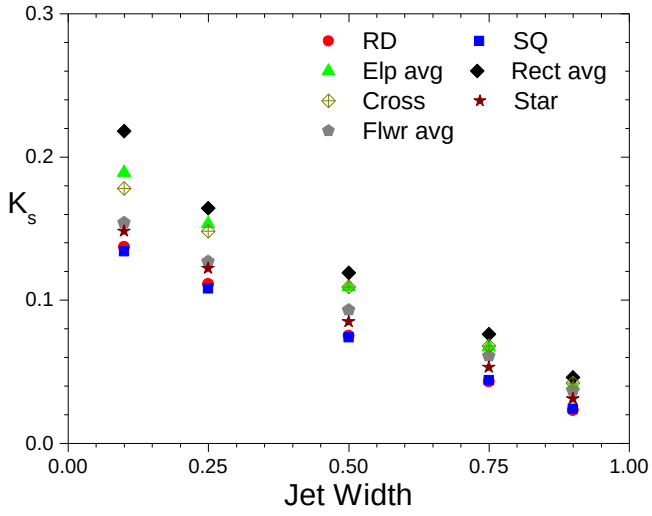

Figure 4.3: Variation of spread rate with jet width

nozzle geometry and the slope ($K_{s0.1\text{-}0.9}$) of the linear part of the plot estimated. The results are summarized in Table 4.2 together with the conventional spread rate ($K_{s0.5}$) for $y_{0.5}$. It is observed that the jets with larger jet thickness also have larger spread rates; for example, the rectangular nozzle which has the greatest spread rate also has the greatest slope (and hence jet thickness), while the round and square nozzles with the least value of $K_{s0.5}$ also have the least value of $K_{s0.1\text{-}0.9}$.

4.1.3 Mass entrainment

As the jet evolves, the mass flux is expected to increase with streamwise direction due to spreading and subsequent entrainment of the ambient fluid. The mass flux per unit width (m) at selected streamwise locations was estimated for each jet nozzle as shown in Figure 4.5. This mass flux was then normalized by the corresponding value at the jet exit (m_o at $x^* = 0.25$). The mass flux was estimated using the equations:

$$m = 2\pi\rho \int_0^\infty Ur\, dr \tag{4.2}$$

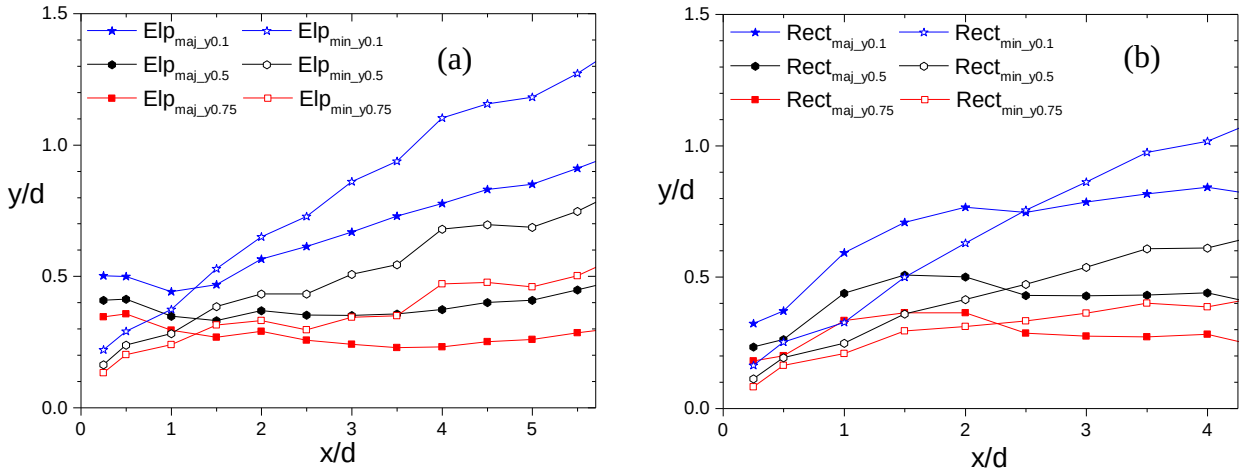

Figure 4.4: Axis-switching location for the (a) elliptical and (b) rectangular nozzles

Table 4.2: The spread rate (K_s) and jet thickness rate ($K_{s0.1\text{-}0.9}$)

Jet Nozzle	$K_{s0.5}$	$K_{s0.1\text{-}0.9}$
Round	0.075	0.113
Square	0.074	0.110
Cross	0.109	0.135
Flower avg	0.093	0.117
Star	0.085	0.117
Rectangle avg (AR = 2)	0.119	0.161
Ellipse avg (AR = 2)	0.112	0.150

$$m = \rho \int_{-\infty}^{\infty} U dy \tag{4.3}$$

where ρ is the density of water, r is the radius of the round and elliptical nozzles and U is the mean streamwise velocity. Jets produced from rectangular and elliptical nozzles in their respective minor axes entrain more ambient fluid than in their major axis and this is consistent with the more spreading that occurs in the minor axis planes of these jets as they evolve in the streamwise direction. This trend is consistent with Ho & Gutmark (1987) who observed higher entrainment in

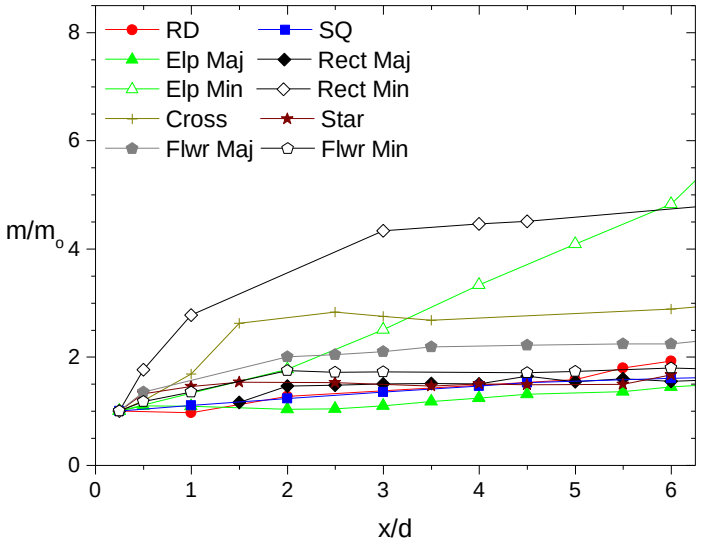

Figure 4.5: Variation of mass flux with streamwise distance

the minor axis plane of an elliptic jet (AR = 2) compared with its major axis plane, as well as plane and round jets. The cross nozzle also entrained more ambient fluid than the round, square, star and flower nozzles in the near-field of the jet. For example, at x/d = 3, the mass flux of the cross nozzle is about 2 times greater than the square nozzle. By x/d = 6, the highest mass entrainment is observed in the minor plane of both the rectangular and elliptical nozzles, implying more mixing in the rectangular and elliptical nozzles compared to all the other jets studied.

4.1.4 Summary

The mixing characteristics were explored for round, square, elliptical, rectangular, star, cross and flower shaped nozzles. The rectangular and elliptical nozzles have a higher decay rate compared to the other nozzles studied. The spread rate of the rectangular nozzle is 61% higher than the square nozzle, while the elliptical nozzle spread rate is about 45% greater than the round nozzle according to the conventional half-velocity width ($y_{0.5}$). The other velocity widths (i.e. $y_{0.9}$, $y_{0.75}$, $y_{0.25}$, $y_{0.1}$)

used in the present study also showed the greatest spreading occurring in the rectangular and elliptical nozzles. The axis-switching phenomenon, which results from the dynamics of the elliptical and rectangular vortex structures, is the reason for this enhanced entrainment and mixing in the rectangular and elliptical nozzles. The axis-switching location is estimated at x/d = 2.3 and x/d = 1.25 for the rectangular and elliptical nozzles respectively and this location remained the same regardless of the jet width used to estimate it. The greatest mass entrainment occurred in the rectangular, elliptical and cross nozzles

4.2 Air experiment results

The rectangular (Rect) and cross shaped nozzles were selected based on their mixing performance from the water jet experiment. The round (RD) nozzle was also investigated and used as a reference nozzle for comparison. The mean and turbulent fields of these jets were studied and are presented in this section.

4.2.1 Contours of mean and turbulent fields of the jet

Contour plots are used to help visualize the qualitative features of the flow. As a result, they are useful in revealing the differences of flow characteristics due to the jet nozzle geometry. Contours of the streamwise mean velocity, spanwise mean vorticity, turbulent intensities and Reynolds shear stress in the near-field (i.e. $0 \leq x/d \leq 10$) are presented in this section.

4.2.1.1 Mean streamwise velocity

The mean velocity contours normalized by U_j and d (i.e. $U^* = U/U_j$, $y^* = y/d$) for the round, cross and rectangular nozzles are shown in Figure 4.6. It can be seen that the velocity of the jets increase

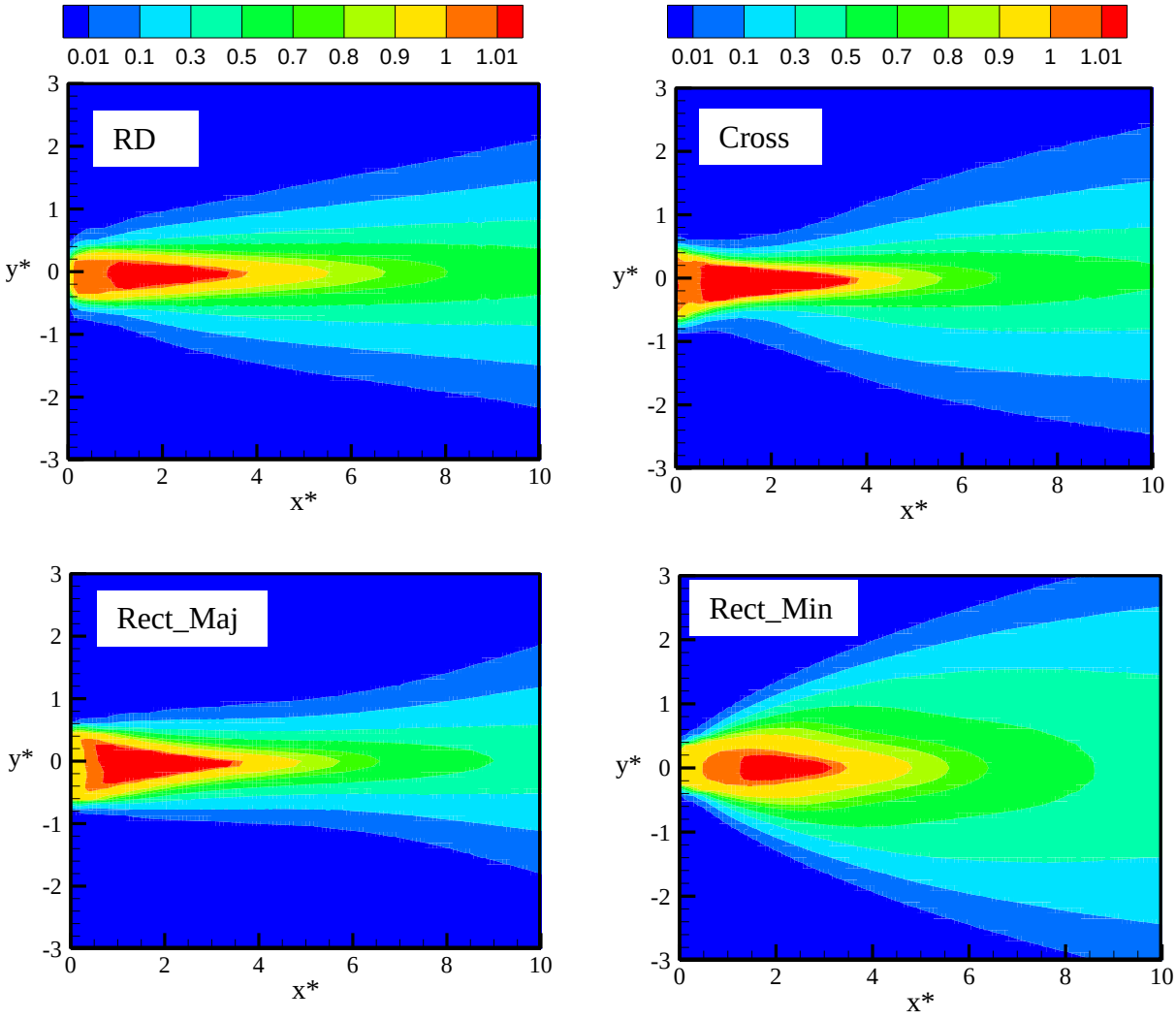

Figure 4.6: Normalized mean velocity (U^*) contours for round, cross and rectangular nozzles

from the nozzle exit till it reaches its maximum some distance from the nozzle exit due to the vena contracta effect. The jet velocity then decays with streamwise distance. For the rectangular nozzle, in the major axis plane, the jet is initially thicker compared to its minor axis plane, but as the jet evolves downstream and the ambient fluid is entrained into the core jet, the jet becomes thicker in the minor axis plane compared to its major axis. This process illustrates the axis-switching phenomenon which is the reason for the enhanced entrainment in the rectangular jet compared

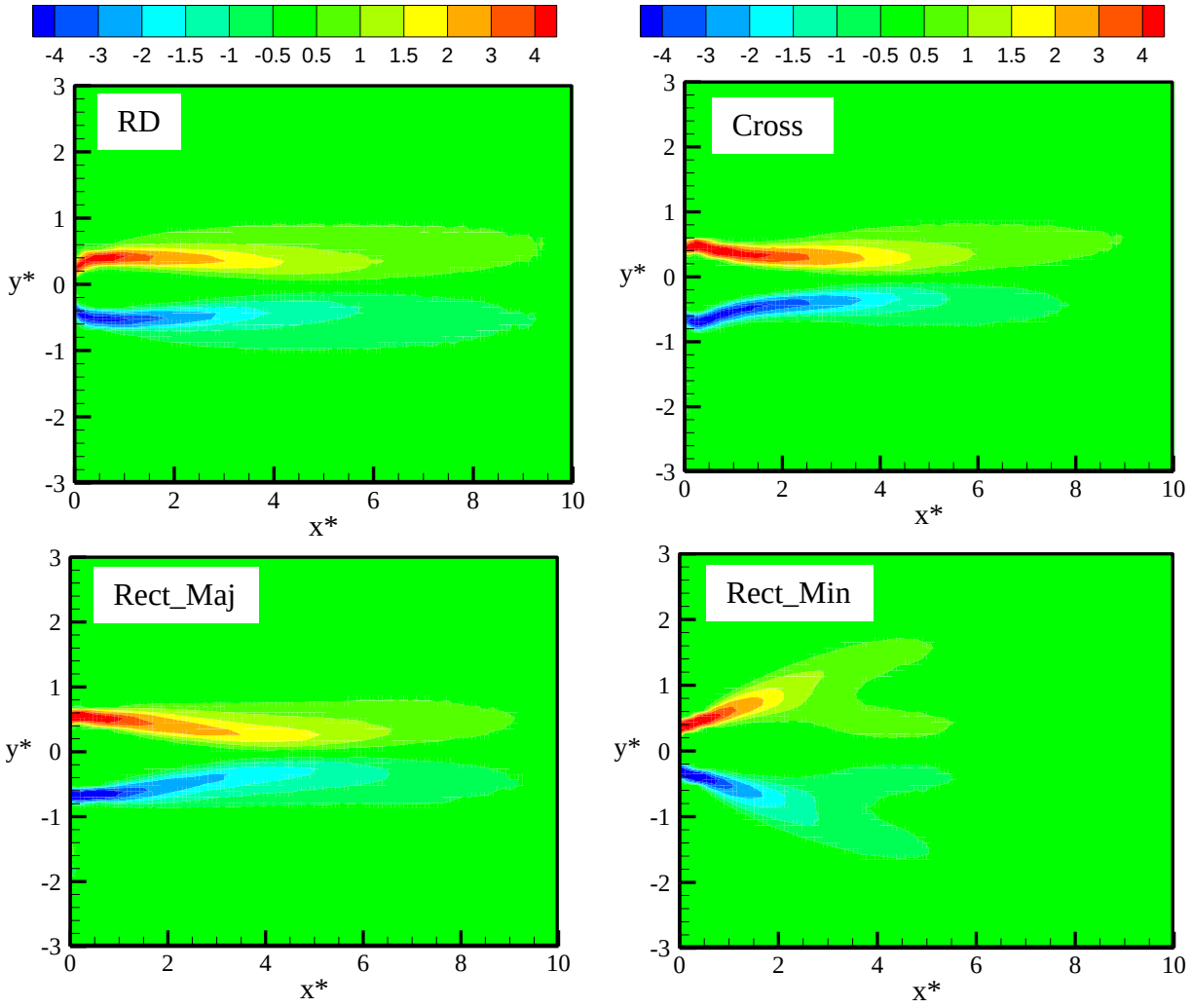

Figure 4.7: Normalized spanwise vorticity (Ω_z^*) of round, cross and rectangular nozzles

with the other jets.

4.2.1.2 Spanwise mean vorticity

The normalized spanwise mean vorticity ($\Omega_z^* = \Omega_z d/U_j$) contours are shown in Figure 4.7. The spanwise mean vorticity was calculated from the mean shear gradients (i.e. $\Omega_z = \partial V/\partial x - \partial U/\partial y$). The positive values of the spanwise mean vorticity indicate a counter-clockwise rotation of

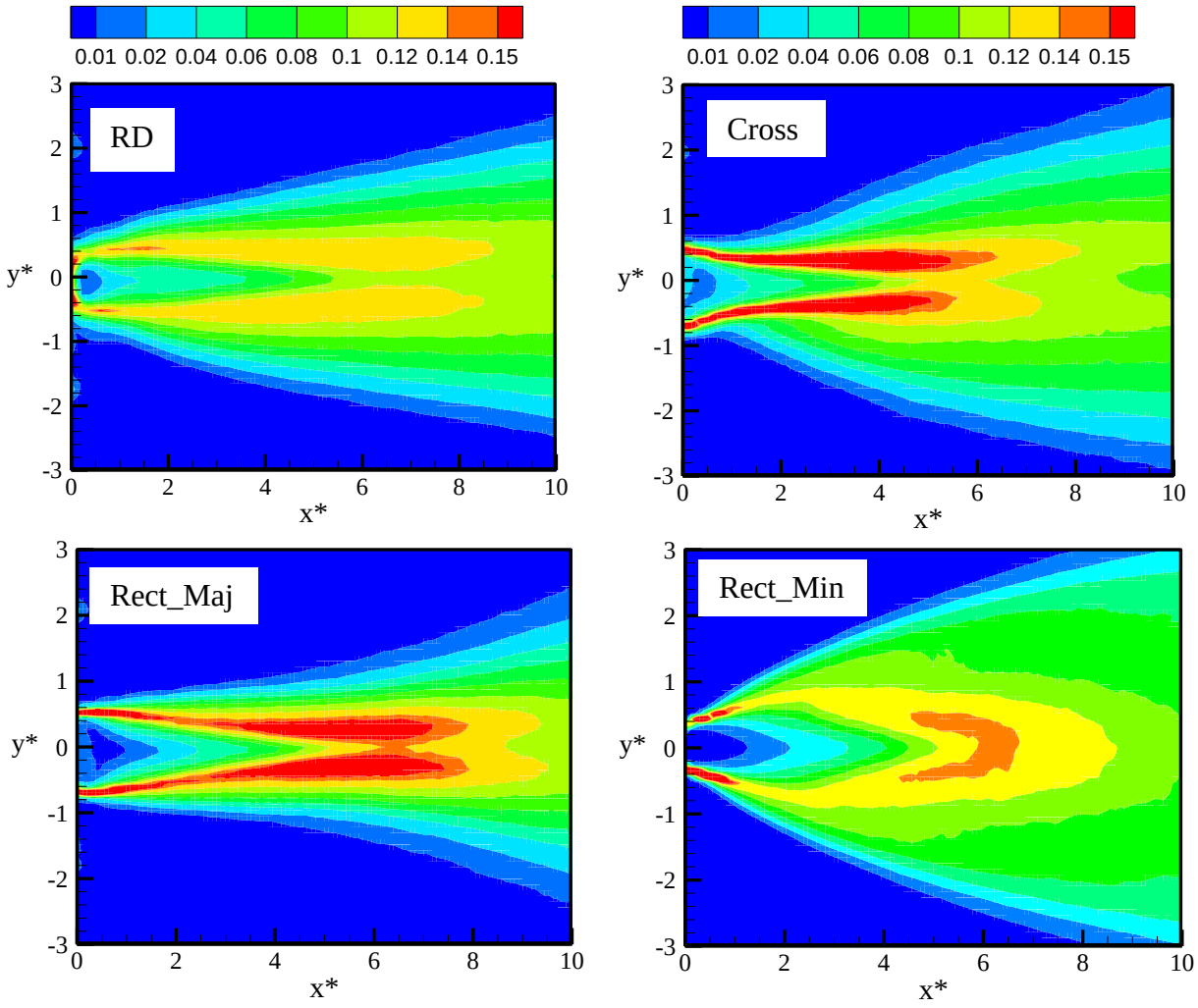

Figure 4.8: Normalized streamwise turbulent intensity for the round, cross and rectangular nozzles

vortices while the negative values indicate a clockwise rotation of the vortices in the flow field. There exists a pair of counter-rotating vortices which have a larger value close to the nozzle exit, but their intensity decays with streamwise distance. This is because the dominant term of the spanwise mean vorticity, $\partial U/\partial y$, is greatest close to the nozzle exit and decays with streamwise distance. Also, $\Omega_z^* \approx 0$ on the jet centerline since the velocity gradients are approximately zero on the jet centerline. The counter-rotating vortices entrain the ambient fluid into the core jet and

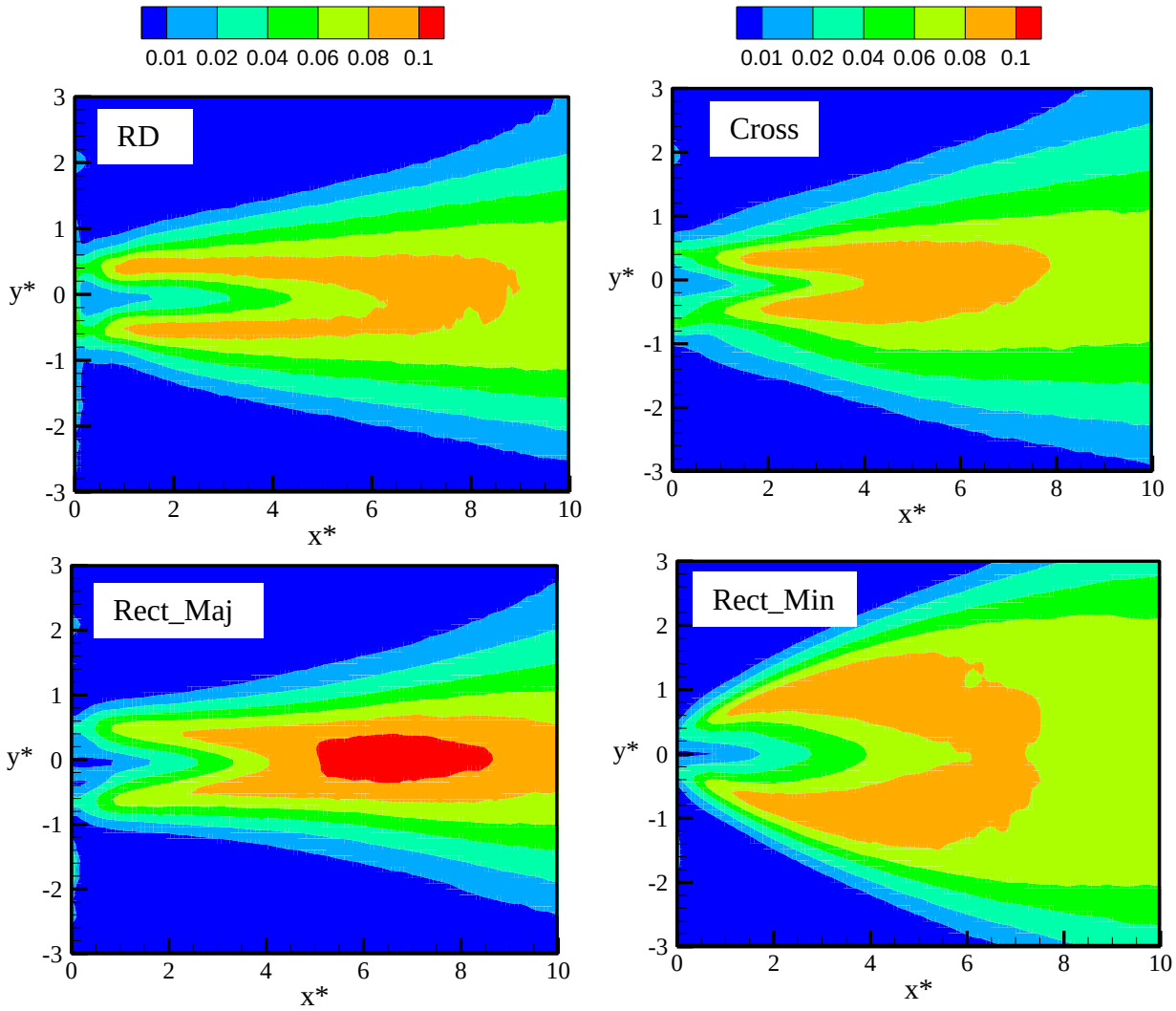

Figure 4.9: Normalized transverse turbulent intensity for the round, cross and rectangular nozzles

thereby aid in the mixing of the two fluid streams. This entrainment and subsequent mixing leads to the decay of the vorticity, with the fastest decay occurring in the rectangular minor plane.

4.2.1.3 Turbulence intensity

Contours of the streamwise turbulent intensity normalized by U_j are shown in Figure 4.8. The initial instabilities produced in the shear layer of the jet flow result in turbulence, which aids in the

mixing of the ambient fluid with the core jet. As a result, the local maxima values of $\sqrt{\overline{u^2}}/U_j$ for all the nozzles studied occurred on either side of the jet centerline. The streamwise turbulence intensity then decays with streamwise distance in the jet shear layers and diffuses towards the jet centerline. Consequently, $\sqrt{\overline{u^2}}/U_j$ on the centerline increases from the nozzle exit till it reaches it maximum at some distance downstream the nozzle exit, before decaying with streamwise distance.

The normalized transverse turbulent intensity ($\sqrt{\overline{v^2}}/U_j$) for the various nozzles are presented in Figure 4.9. The contours show that $\sqrt{\overline{v^2}}/U_j$ increase from the nozzle exit, attain a maximum downstream of the nozzle due to the merging of the jet layers, then decrease with streamwise distance. This trend was observed for all the nozzle geometries studied.

4.2.1.4 Reynolds shear stress

Figure 4.10 shows the normalized Reynolds shear stress contours (i.e. $-\overline{uv}^* = -\overline{uv}/U_j^2$). The contours show a gradual increase from the nozzle exit to reach a maximum some distance downstream of the nozzle, before decaying with streamwise distance. The maximum intensity of the Reynolds shear stress persists for longer streamwise distances in the rectangular (major plane) and cross nozzles, compared with the round nozzle. Since the dominant term of the production of Reynolds shear stress is $\overline{v^2}\partial U/\partial y$, it implies that the Reynolds shear stress is intense where $\overline{v^2}\partial U/\partial y$ is high and zero where its production is also zero. The higher values of $-\overline{uv}^*$ seen in the contours implies that the transfer of momentum from the streamwise to the transverse direction in the rectangular and cross shaped jet flow fields are higher and hence improve the overall mixing capacity compared to the round nozzles.

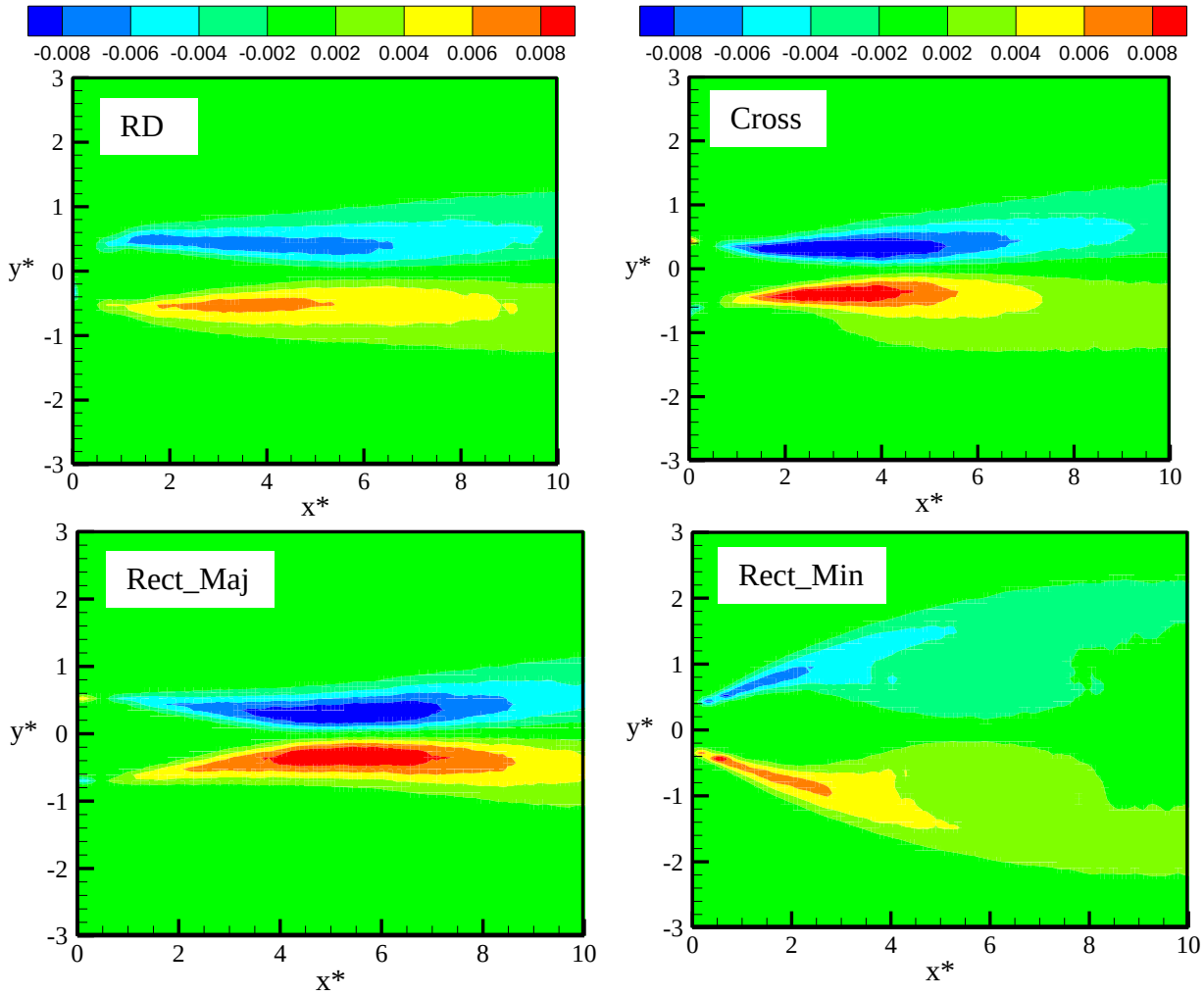

Figure 4.10: Normalized Reynolds shear stress ($-\overline{uv}^{*}$) contours for round, cross and rectangular nozzles

4.2.2 One-dimensional profiles of mean and turbulent quantities

In order to quantify the differences in the mean and turbulent quantities of the various jet flows, one-dimensional profiles of the mean velocities, turbulent intensities and the Reynolds shear stress were examined. The mean velocity decay rate, spread rate and streamwise evolution of the streamwise turbulent intensity were also evaluated.

4.2.2.1 Mean velocity decay and spread rate

Figure 4.11 shows the mean velocity decay distribution. The data from the round, cross and rectangle nozzles is fitted to Equation 2.1 and the decay rates are summarized in Table 4.3. The decay rates (K_u) for the rectangular, cross and round nozzles are 0.188, 0.180 and 0.174 respectively. The rectangular nozzle has the highest value of K_u and would therefore mix more with the ambient fluid compared to the round nozzle. The values of K_u obtained in the water jet experiments for round, cross and rectangular nozzles are higher (about 18% in the rectangular cases for example) than the values obtained for the air jets. This can be attributed to the modified configuration of the nozzles used for the air jet study, i.e. a straight section leading to a linear contraction for the nozzles. The nozzles used in the water jet experiment do not have such a modification and approximate more an orifice plate nozzle compared with the modified air jet experiment nozzles. There is also a stronger *Re* dependence on K_u for $Re < 10{,}000$ but this dependence becomes weaker for $Re > 10{,}000$ (Deo et al., 2008) and this may also account for some of the differences in K_u between the two experiments.

Another way to quantify the near-field entrainment is by estimating the potential core of the jet. A shorter potential core implies a faster mixing of the core jet with the ambient fluid. The potential core length (L_c) was estimated as the length from the nozzle exit to the location where the centerline velocity has decayed to 98% of the maximum velocity (e.g. Mi & Nathan, 2010). $L_c \approx 3.7d$, $3.3d$ and $3.2d$ for the round, rectangular and cross nozzles respectively in the present study; the smaller values of L_c for the rectangular and cross nozzles compared with the round nozzle indicate a more efficient near-field mixing in the non-circular nozzles. The values of L_c for the round, cross and rectangular nozzles for the study of Mi & Nathan (2010) also indicate smaller potential core

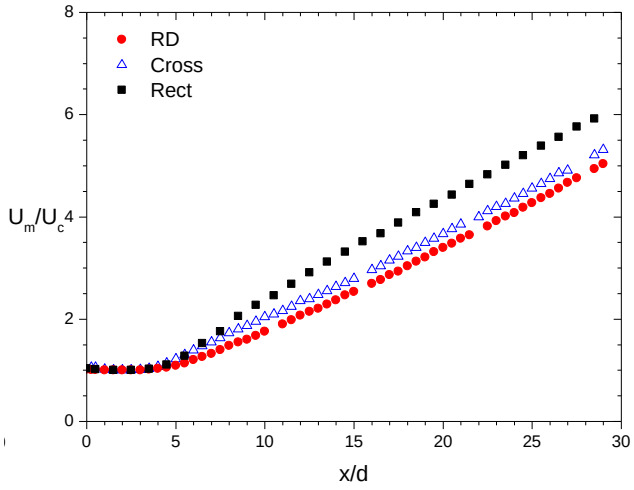

Figure 4.11: Mean velocity decay on jet centerline for round, cross and rectangular nozzles

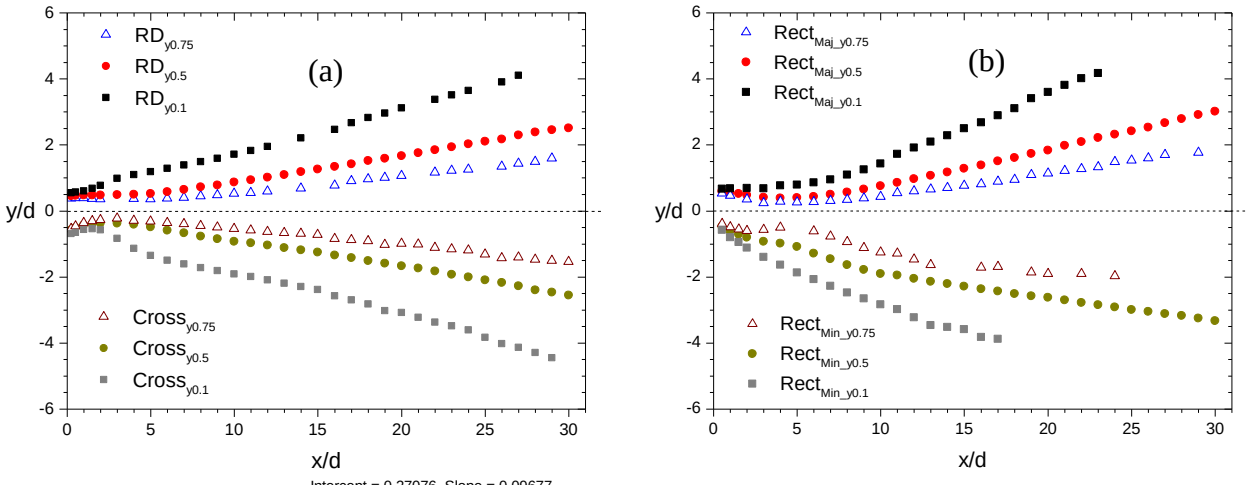

Figure 4.12: Variation of $y_{0.1}$, $y_{0.5}$ and $y_{0.9}$ of the various nozzle geometries with streamwise distance

Table 4.3: Decay rates for round, cross and rectangular nozzles

Jet Nozzle	*Decay Rate*
Round	0.174
Cross	0.180
Rectangle	0.188

Table 4.4: Jet spread rate for the various jet widths for the nozzles

Jet Nozzle	$K_{s0.1}$	$K_{s0.5}$	$K_{s0.75}$
Round	0.139	0.083	0.053
Cross	0.148	0.089	0.059
Rectangle avg	0.193	0.100	0.062

lengths for the rectangular and cross nozzles compared with that for the round nozzle (i.e. L_c = 4.2d for the round nozzle, L_c = 3.1d for the cross nozzle and L_c = 2.9 for the rectangular nozzle).

The jet velocity widths, $y_{0.75}$, $y_{0.5}$ and $y_{0.1}$ (Figure 4.12) were used to quantify the spreading of the jets (fitting the data to Equation 4.1) and the results are summarized in Table 4.4. It can be seen that the rectangular nozzle shows the greatest spreading compared with the round and cross nozzles for all the velocity widths considered. For example, near the jet centerline, the jet spread rate ($K_{s0.75}$) in the rectangular nozzle is 17% greater than the round nozzle; at the edge of the jet, the value of $K_{s0.1}$ for the rectangle nozzle is 39% greater than the round nozzle, while for the conventional spread rate ($K_{s0.5}$), the rectangular nozzle spreads 20% faster than the round nozzle. This implies that although the jet spread faster as one moves from the jet centerline to the edge of the jet for all nozzles, the rate of spreading and hence mixing of the core jet with the ambient fluid occurs at the fastest rate for the rectangular nozzle. This again, is due to the axis-switching phenomenon, which occurs at $x/d \approx 1$ for the rectangular jet. The value for $K_{s0.5}$ reported for a round jet in Quinn (2006) at Re_j = 184,000 was 0.098 and is about 15% greater than the value for $K_{s0.5}$ in the air jet experiments. This can be attributed to the modified orifice plate nozzle used, as well as the relatively low *Re* in the current study.

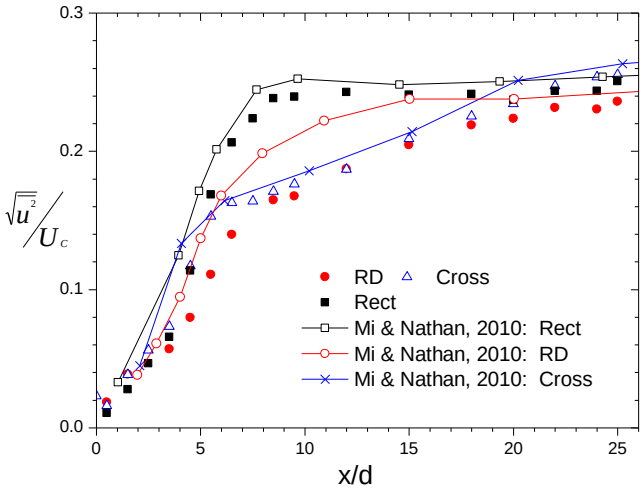

Figure 4.13: Streamwise turbulent intensity on the jet centerline for round, cross and rectangular nozzles

4.2.2.2 Streamwise turbulent intensity along the jet centerline

The evolution of streamwise turbulent intensity ($\sqrt{\overline{u^2}}/U_c$) with streamwise distance is shown in Figure 4.13. The datasets reported by Mi & Nathan (2010) for round, cross and rectangular nozzles are also included in the plot for comparison. An initial increase in $\sqrt{\overline{u^2}}/U_c$ occurs for all nozzles studied in the near-field of the jet. This is due to the net positive production of turbulent kinetic energy on the jet centerline, as well as the diffusion of turbulence from the jet shear layer into the core jet in the near-field of the jet. The turbulence intensity in the rectangular nozzle is higher than in the round and cross nozzles, and the peak value of 0.24 is comparable to 0.25 reported for the rectangular jet in Mi & Nathan (2010). After attaining its peak, the streamwise turbulent intensity then decays to its asymptotic value further downstream of the flow. At x/d = 25, for example, the values of $\sqrt{\overline{u^2}}/U_c$ in the present study are 0.24, 0.25 and 0.26 for the round, rectangle and cross nozzles respectively and these values are comparable to those obtained for Mi & Nathan (2010).

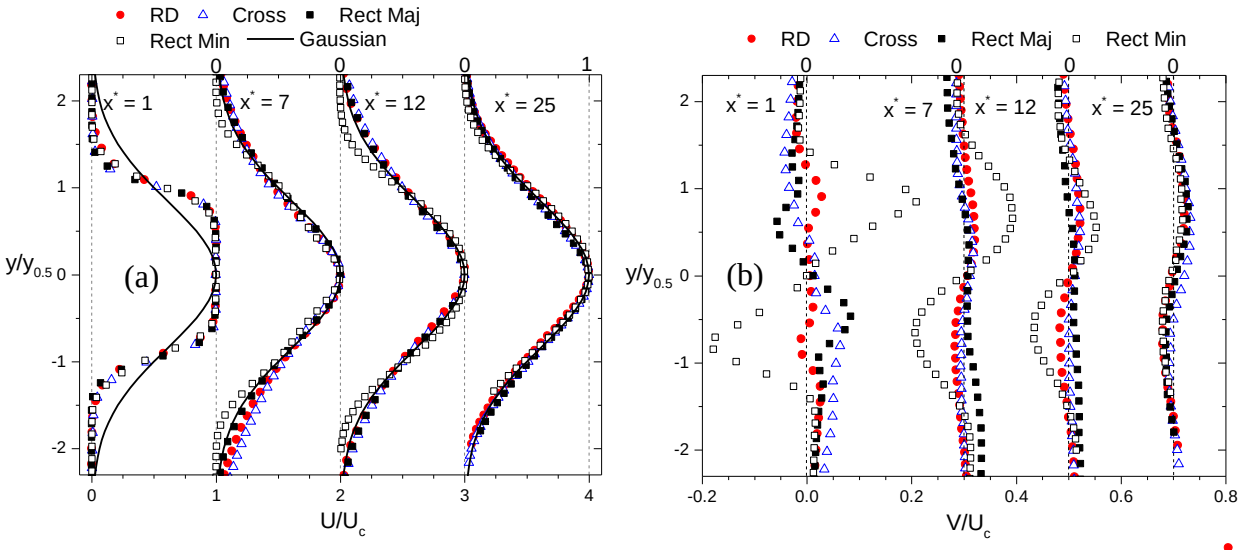

Figure 4.14: (a) Streamwise and (b) transverse mean velocity profiles for the round cross and rectangular nozzles

It should be noted that the typical asymptotic value for the round jet in the self-similar region is approximately 0.24 (e.g. Panchapakesan & Lumley, 1993).

4.2.2.3 Mean velocity profiles

The streamwise mean velocity profiles of the round, rectangular and cross nozzles for $x^* = 1$, 7, 12 and 25 (where $x^* = x/d$) are presented in Figure 4.14 (a). The velocity profiles are normalized by U_c and $y_{0.5}$. The normalized velocity profiles in the self-similar region of the free jet are expected to follow a Gaussian distribution. Therefore for comparison purposes, the following Gaussian distribution is included:

$$\frac{U}{U_c} = e^{-\ln 2(y/y_{0.5})^2} \tag{4.3}$$

The profiles of U/U_c for all the nozzle configurations very near the nozzle exit (e.g. at $x^* = 1$), do

not follow the Gaussian distribution as expected. However, as one moves further downstream, the profiles evolve into a Gaussian-like distribution. The streamwise mean velocity profiles become self-similar for $x^* > 12$, and by $x^* = 25$, the profiles of U/U_c for all the nozzles collapse onto each other.

The transverse mean velocity profiles normalized by U_c are shown in Figure 4.14 (b). At $x^* = 1$, 7 and 12 for example, the transverse velocity in the rectangular jet is directed towards the jet centerline in the major axis while V/U_c is directed away from the jet centerline in the minor axis plane. This is because the vortical structures in jet shrink in the major axis plane, while expanding in the minor axis plane. As a result, ambient fluid is drawn into the jet through the major axis side, whilst fluid in the core jet is ejected outwardly, hence causing the two fluid streams to mix (Hussain & Husain, 1989). For example, at $x^* = 1$, V/U_c for the rectangular nozzle in the minor axis is about 6 times greater than its corresponding value for the round nozzle, implying more mixing and entrainment are taking place in the rectangular nozzle, compared with its round counterpart. Although the magnitude of the transverse mean velocity decays with streamwise distance, its magnitude at $x^* = 7$ and $x^* = 12$ is still higher for the rectangular nozzle, compared with the round or cross jet. By $x^* = 25$, however, the values of V/U_c become identical to each other.

4.2.2.4 Turbulent intensity profiles

Profiles of the turbulent intensities in both the streamwise and transverse directions are shown in Figure 4.15. Both the streamwise and transverse turbulence intensities are normalized by U_c. Although the profiles of both $\sqrt{\overline{u^2}}/U_c$ and $\sqrt{\overline{v^2}}/U_c$ show a double peak in the near-field (for example at $x^* = 1$), the magnitude of the streamwise turbulence intensity is higher than its

transverse counterpart. The intensities on the jet centerlines ($y/y_{0.5}$ = 0) however, are very low and the overall distributions are similar in all the jets. As the jets develop further downstream, the double peaks disappears by (x^* = 7) for $\sqrt{\overline{v^2}}/U_c$ but persists further for the case of $\sqrt{\overline{u^2}}/U_c$. The rectangular nozzle shows higher turbulent intensities in the near-field of the jet, but further downstream, the intensities of the various nozzles collapse on each other.

4.2.2.5 Reynolds shear stress profiles

The profiles of the Reynolds shear stress for the rectangular, cross and round nozzles for x^* = 1, 7, 12 and 25 are shown in Figure 4.16. Near the nozzle exit (i.e. x^* = 1), the profiles of $-\overline{uv}/U_c^2$ for all the nozzles are identical to each other. The Reynolds shear stress is zero at the jet centerline but is non-zero in the jet shear layer. By x^* = 7 and 12, the effects of the nozzle geometry emerge. In the major axis of the rectangular nozzle, the highest values of the Reynolds shear stress were observed. For example, at x^* = 7, the peak value for the Reynolds shear stress in the major axis of the rectangular nozzle is about 1.5 times greater than its corresponding value in the round nozzle. These peak values then decay with streamwise distance and by x^* = 25, there is no significant difference between the levels of the Reynolds shear stress in any of the nozzles studied. The peak value of the normalized Reynolds shear stress at x^* = 25 for the round nozzle is 0.016 which compares well with the study of Hussein et al. (1994) who reported a value of $-\overline{uv}/U_c^2 \approx 0.018$ in the self-similar region of a round jet.

4.2.3 Reynolds stress ratios, correlation coefficient, structure parameter and eddy viscosity

Figure 4.17 shows profiles of the ratio of the streamwise Reynolds normal stress to the transverse Reynolds normal stress ($\overline{u^2}/\overline{v^2}$) for x^* = 7, 15 and 25 and this ratio is used to assess the large-scale

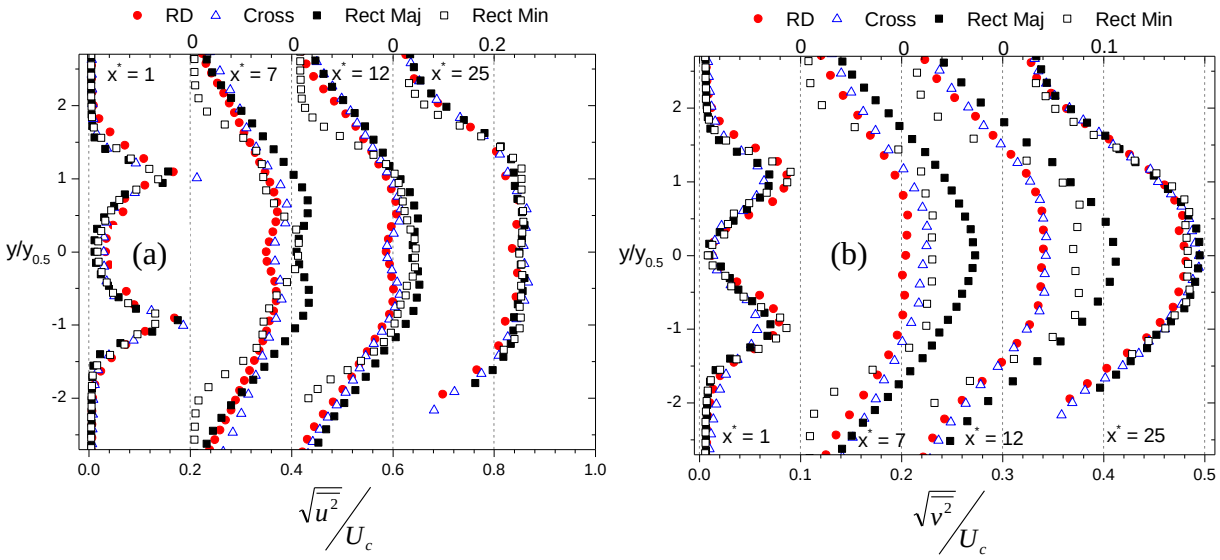

Figure 4.15: (a) Streamwise and (b) transverse turbulent intensity profiles for the round, cross and rectangular nozzles

anisotropy of the jets in the current study. For isotropic flow, the stress ratio $\overline{u^2}/\overline{v^2}$ = 1 but turbulent shear flows are generally anisotropic (i.e. $\overline{u^2}/\overline{v^2} \neq 1$). For example, in the shear layers of the round, cross and rectangular nozzles considered, $\overline{u^2}/\overline{v^2} > 2$. On the jet centerline ($y/y_{0.5}$ = 0), the value of $\overline{u^2}/\overline{v^2}$ for the round and rectangular nozzle (in the minor axis plane) is 3.62 and 2.53 respectively for x^* = 2 (not shown). This suggests that the level of anisotropy in the round nozzle is greater in the very near-field compared with the non-circular nozzles. The values of $\overline{u^2}/\overline{v^2}$ for the round nozzle also decrease by 16% from x^* = 7 to x^* = 15; there is a corresponding decrease of 33% for the rectangular nozzle (in the minor axis plane). The faster decay of $\overline{u^2}/\overline{v^2}$ for the non-circular nozzles is due to the higher mixing in these nozzle which helps to homogenize the flow and make it more isotropic.

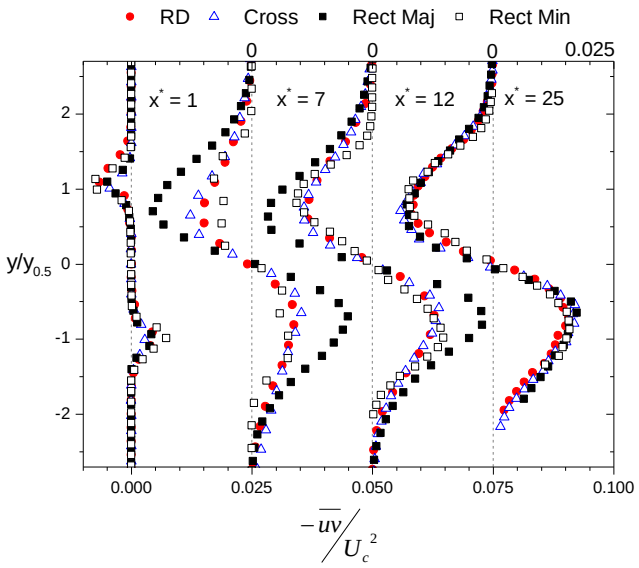

Figure 4.16: Reynolds shear stress profiles for the round, cross and rectangular nozzles

Profiles of the ratio of the Reynolds shear stress to the streamwise and transverse Reynolds normal stresses are shown in Figure 4.18 and Figure 4.19 for x^* = 2, 7, 15 and 25. The profiles of $-\overline{uv}/\overline{u^2}$ and $-\overline{uv}/\overline{v^2}$ are qualitatively similar to the profiles of the Reynolds shear stress. The magnitudes of $-\overline{uv}/\overline{v^2}$ are higher compared to the magnitudes of $-\overline{uv}/\overline{u^2}$ since $\overline{u^2} > \overline{v^2}$ throughout the flow domain. The magnitudes of the profiles of both $-\overline{uv}/\overline{u^2}$ and $-\overline{uv}/\overline{v^2}$ decrease with increasing streamwise distance for each nozzle; however by x^* = 25, the various profiles for each jet nozzle collapse well onto each other. For example, at x^* = 7, the magnitude of $-\overline{uv}/\overline{u^2}$ for the round, cross and rectangular nozzles are 0.341, 0.315 and 0.411 respectively; by x^* = 25, these values are 0.28, 0.269 and 0.273 respectively.

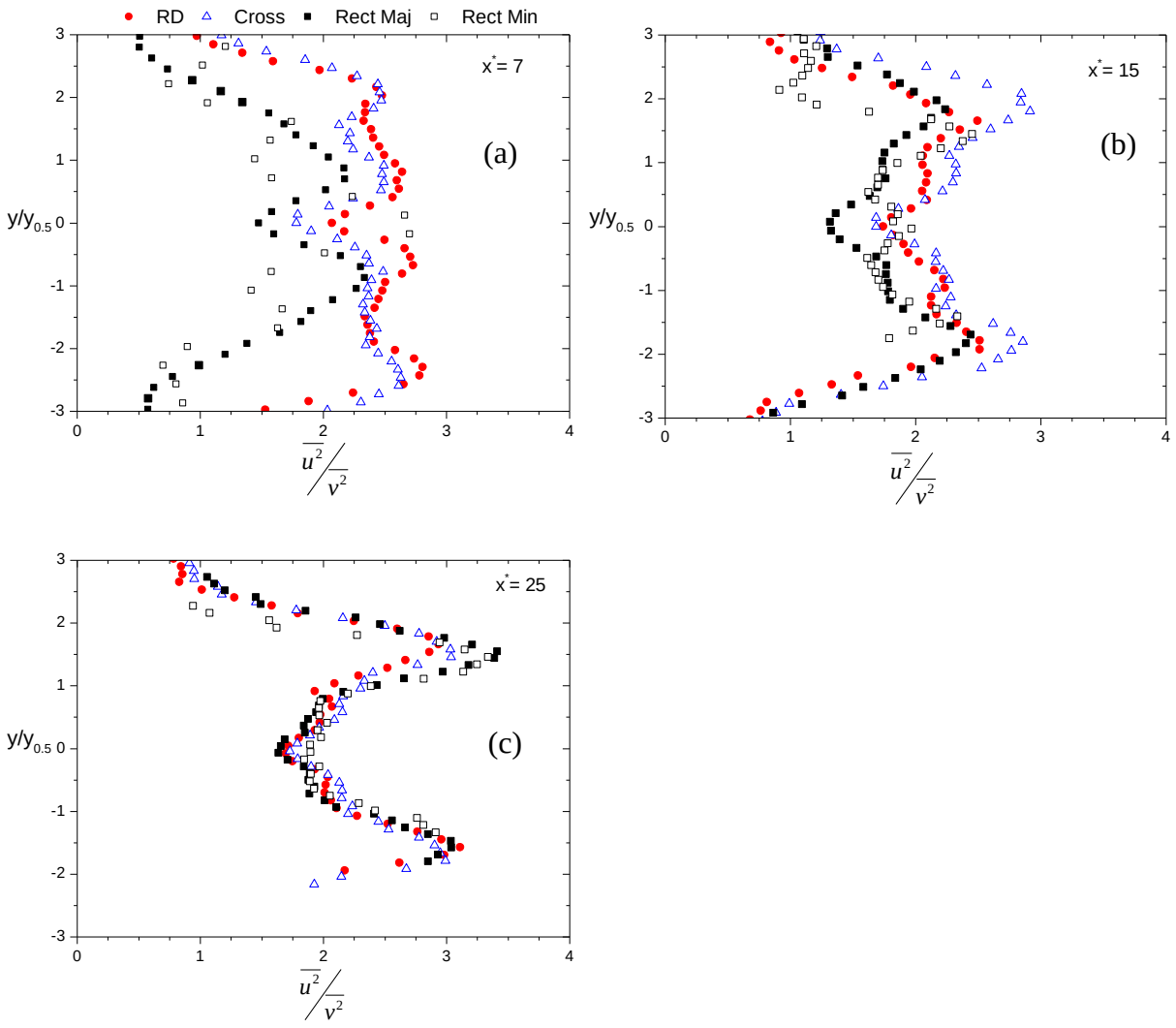

Figure 4.17: Ratio of streamwise Reynolds normal stress to transverse Reynolds normal stress at (a) $x^* = 7$, (b) $x^* = 15$ and (c) $x^* = 25$ for the various nozzle geometries studied.

In Figure 4.20, the correlation coefficient, ρ_{uv}, for the round, cross and rectangular nozzles are shown. The correlation coefficient is defined as the ratio of the Reynolds shear stress and the turbulent intensities, i.e. $\rho_{uv} = (-\overline{uv})/ (\sqrt{\overline{u^2}} \times \sqrt{\overline{v^2}})$. The profiles of the ρ_{uv}, are also qualitatively similar to the Reynolds shear stress profiles. The maximum values of ρ_{uv} in the shear layers decrease with increasing streamwise distance from the nozzle exit. For example, for $x^* = 7$, the correlation coefficient for the round, cross and rectangular nozzles is 0.53, 0.50 and 0.60

respectively; however, by $x^* = 25$, the value of ρ_{uv} for all the nozzles is approximately 0.42. This value is comparable to $\rho_{uv} = 0.4$ for a round jet in the self-similar region (Pope, 2000).

The structure parameter, defined as $-\overline{uv}/2k$ (where k is the turbulent kinetic energy), is shown in Figure 4.21. The turbulent kinetic energy was estimated as $k = 0.5(\overline{u^2} + 2\overline{v^2})$ (e.g. Hu et al., 2000) since the spanwise Reynolds normal stress was not measured. The structure parameter is used in turbulence modelling to estimate the modelling constant, C_μ, which is defined as $(-\overline{uv}/k)^2$. The value of C_μ is typically set to 0.09, which corresponds to $-\overline{uv}/2k = 0.15$. For the various streamwise distances considered, the plots are qualitatively similar to each other and by $x^* = 25$, the peak value of the profiles of $-\overline{uv}/2k \approx 0.154$ for the round, cross and rectangular nozzles. Pope (2000) reported a $-\overline{uv}/k = 0.27$ (i.e. $-\overline{uv}/2k = 0.135$) for a round jet in the self-similar region. Thus, the value of $-\overline{uv}/2k$ reported in this study is comparable with both the turbulence model constant and the value reported in Pope (2000).

The eddy viscosity (ν_t) profiles for the various nozzle geometries are shown in Figure 4.22. The eddy viscosity is typically defined as $\nu_t = -\overline{uv}/(\partial U/\partial y + \partial V/\partial x)$ in standard eddy viscosity models. As expected, from the profiles shown, (i.e. $x^* = 2$, 7, 15 and 25) the values of ν_t are positive within the bulk of the jet because the Reynolds shear stress and the velocity gradients have the same sign. At $x^* = 25$, for example, the peak values of $\nu_t \approx 0.024$, 0.027 and 0.028 for the round, cross and rectangular nozzles respectively. The eddy viscosity for a round jet in the self-similar region reported in Pope (2000) is 0.028 $\pm$15% which is comparable to the values reported in the current study, although the eddy viscosity was estimated as $\nu_t = -\overline{uv}/(\partial U/\partial y)$ in Pope (2000).

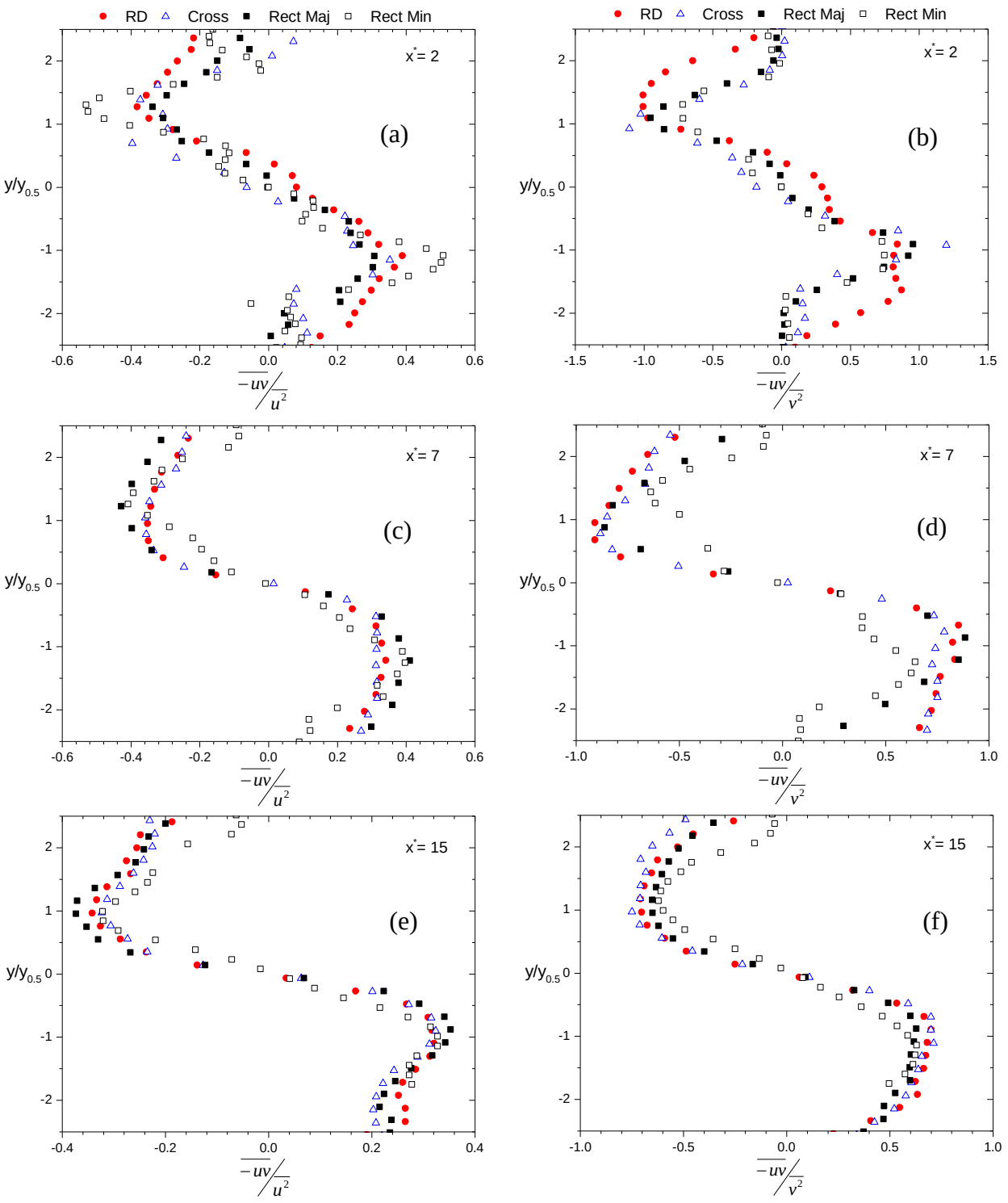

Figure 4.18: Ratio of Reynolds shear stress to streamwise (a, c and e) and transverse (b, d and f) Reynolds normal stresses respectively for x^* = 2, 7 and 15

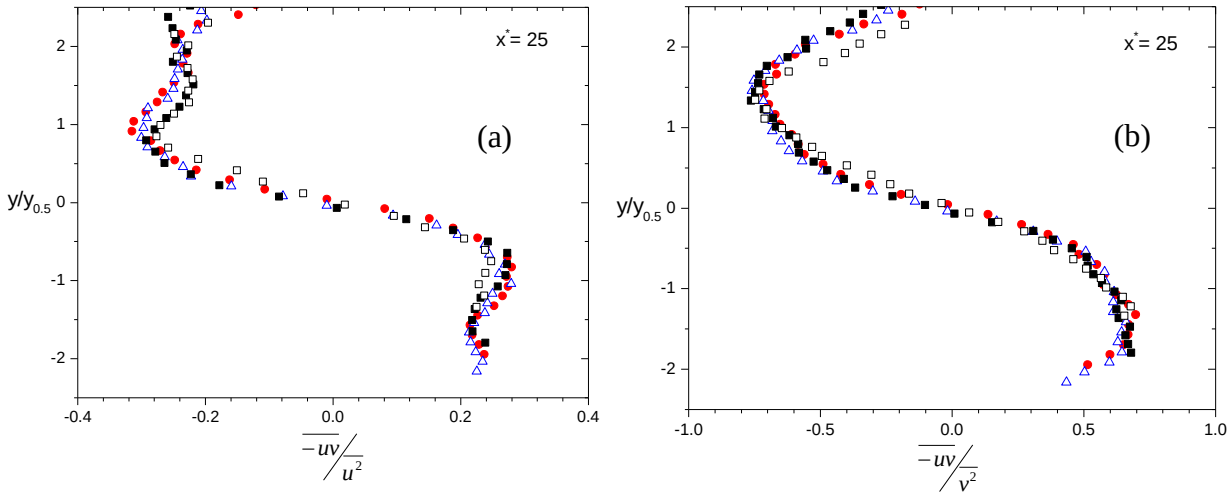

Figure 4.19: Ratio of Reynolds shear stress to the (a) streamwise and (b) transverse Reynolds normal stresses for x^* = 25

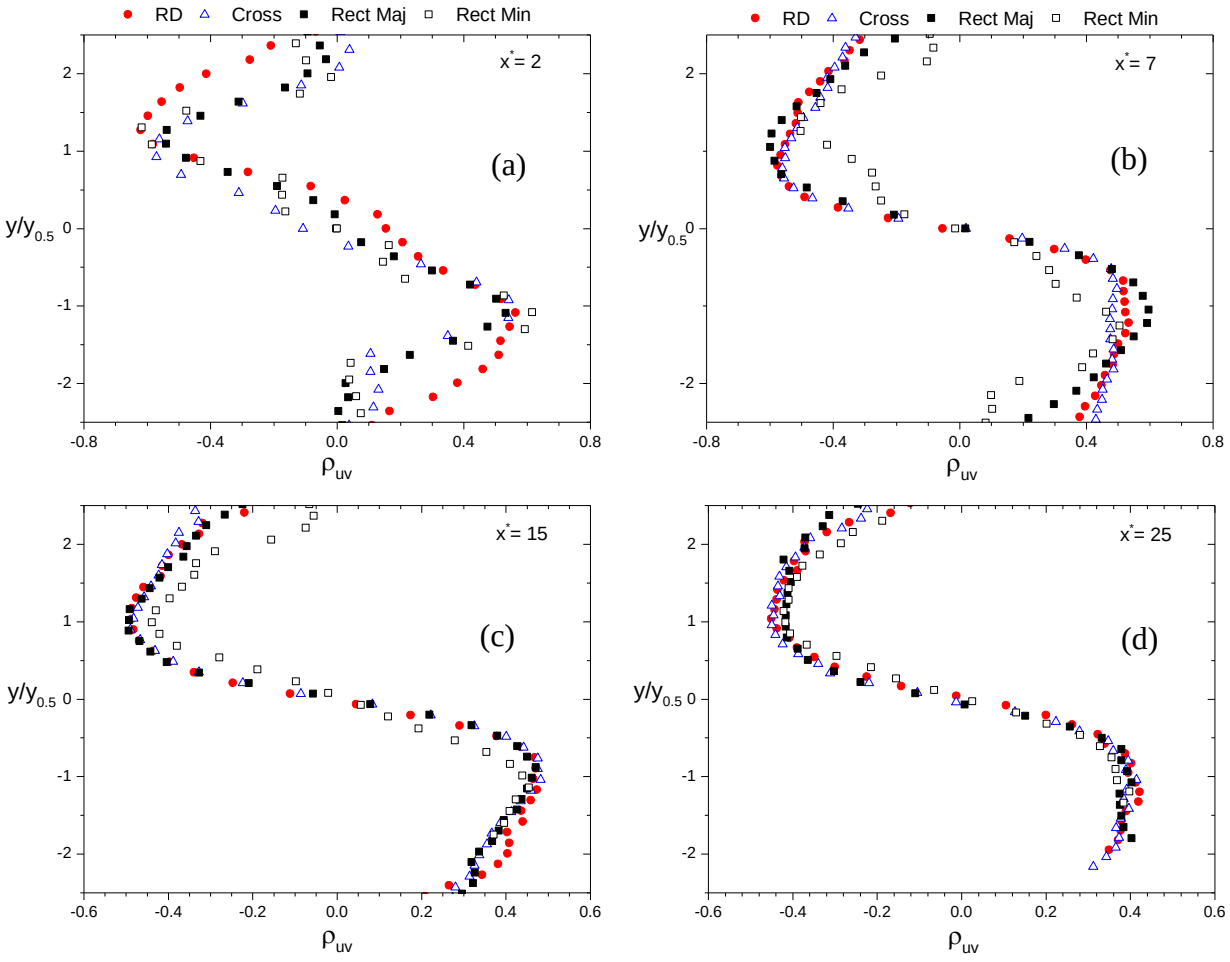

Figure 4.20: Profiles of the correlation coefficient at (a) x^* = 2, (b) x^* = 7, (c) x^* = 15 and (d) x^* = 25 for the round, cross and rectangular nozzles

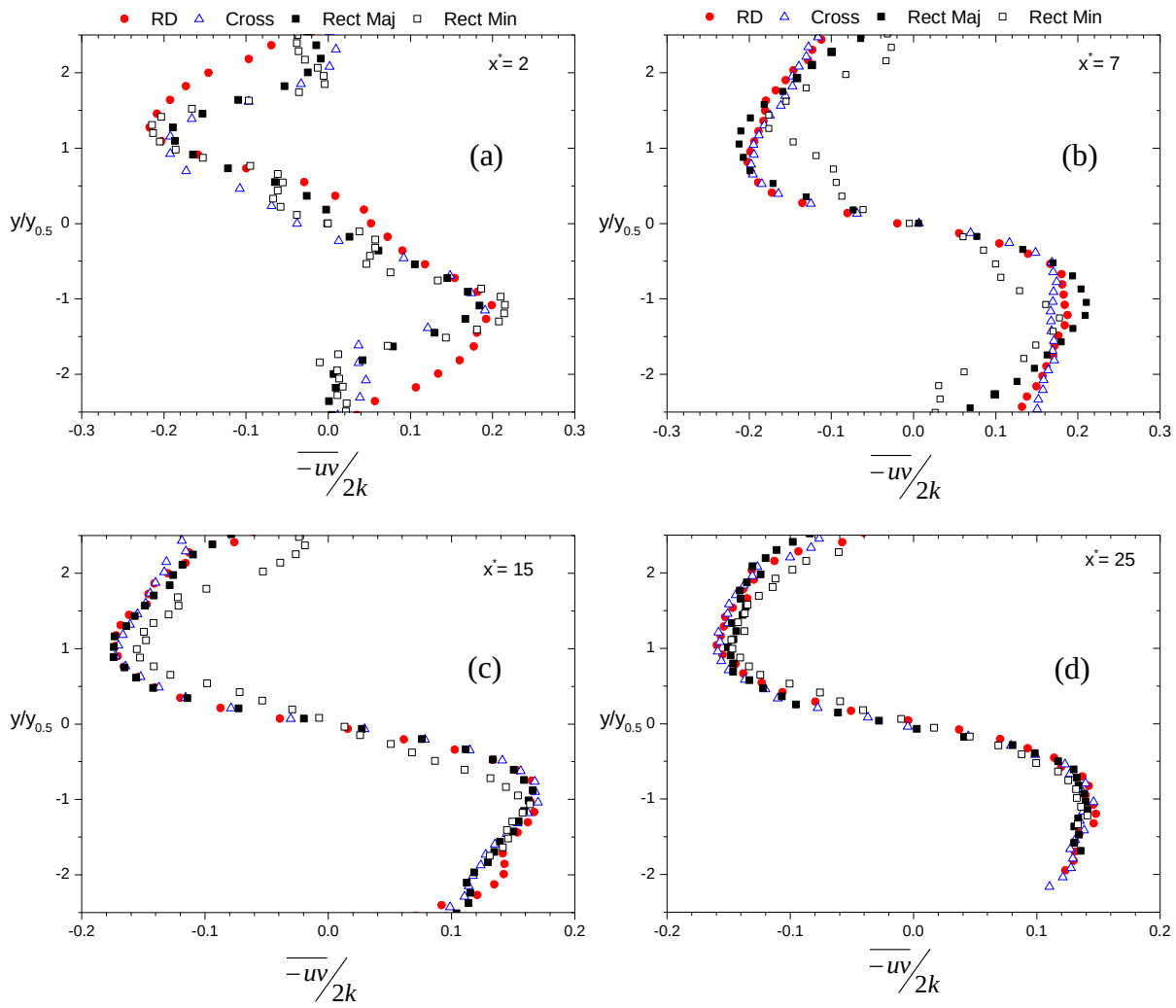

Figure 4.21: Profiles of the structure parameter at (a) $x^* = 2$, (b) $x^* = 7$, (c) $x^* = 15$ and (d) $x^* = 25$ for the round, cross and rectangular nozzles

4.2.4 Budget terms of turbulent kinetic energy

Some budget terms of turbulent kinetic energy equation are presented in this section. These are the production term, $P_k = -(\overline{u^2}\partial U/\partial x + \overline{uv}\partial U/\partial y + \overline{uv}\partial V/\partial x + \overline{v^2}\partial V/\partial y)$, the diffusion term, $D_k = -0.5[\partial(\overline{u^3} + \overline{uv^2})/\partial x + \partial(\overline{u^2 v} + \overline{v^3})/\partial y]$ and the convection term, $C_k = U\partial k/\partial x + V\partial k/\partial y$. These terms are normalized by the jet centerline velocity and the equivalent diameter and are represented

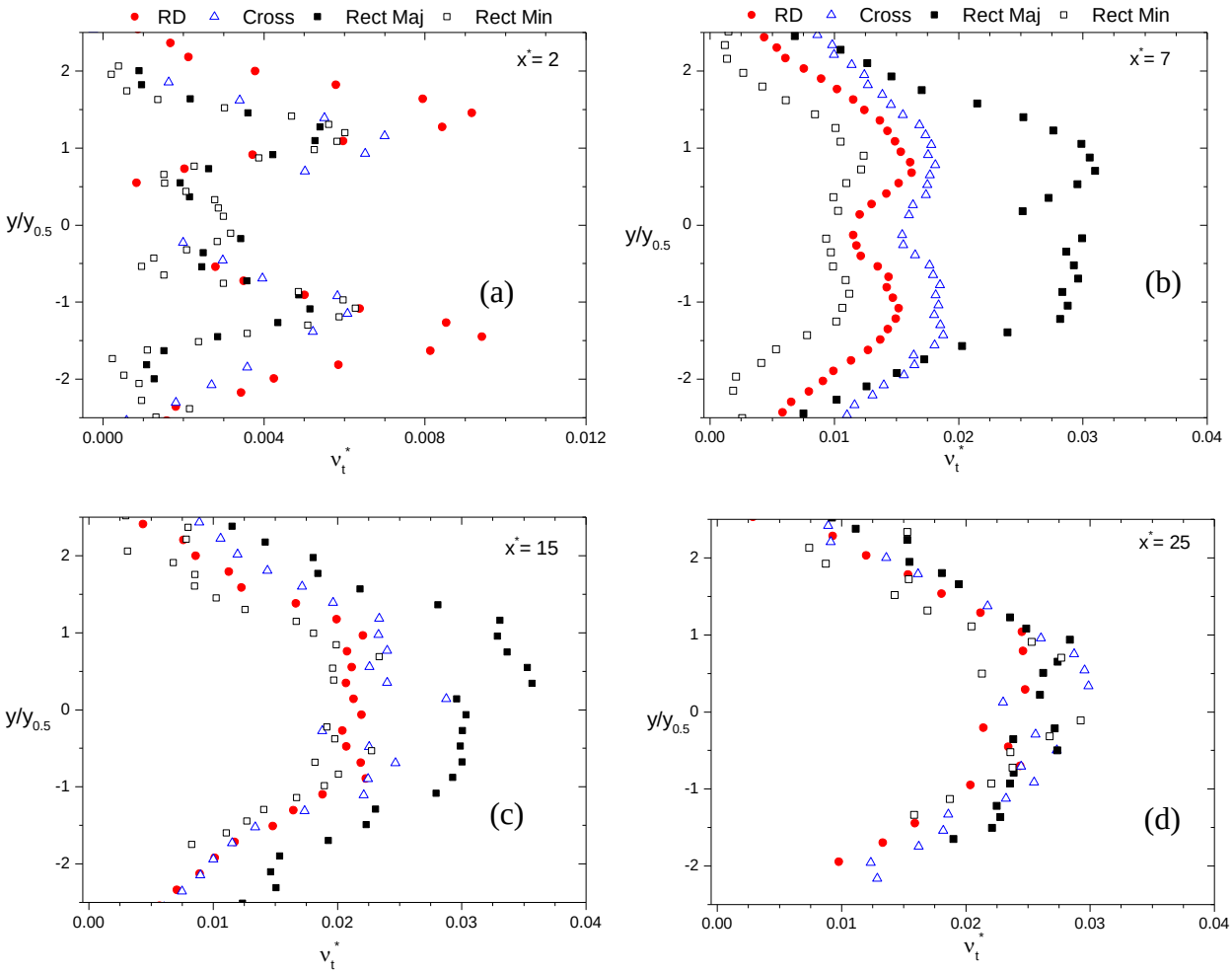

Figure 4.22: Eddy viscosity profiles at (a) $x^* = 2$, (b) $x^* = 7$, (c) $x^* = 15$ and (d) $x^* = 25$ for the round, cross and rectangular nozzles

as P_k^*, D_k^* and C_k^* at $x^* = 2$, 7 and 15 as shown in Figure 4.23, Figure 4.24, and Figure 4.25 respectively.

The production of k represents the action of the mean velocity gradients working against the Reynolds stresses to remove kinetic energy from the mean flow (Pope, 2000). P_k can also be represented as the sum of the production by the normal stresses (P_n) and the production by the shear stress (P_s), i.e. $P_k = P_n + P_s$, where $P_n = -(\overline{u^2}\partial U/\partial x + \overline{v^2}\partial V/\partial y)$ and $P_s = -\overline{uv}(\partial U/\partial y +$

$\partial V/\partial x$). The production of turbulence first increases in the near-field, before decaying with streamwise distance, with P_s being the major contributor to P_k throughout the jet flow in the shear layers. On the jet centerline at $x^* = 7$ and 15, the dominant contributor to P_k is P_n, due to the merging of the shear layers and subsequent growth of the Reynolds normal stresses. The cross and rectangular nozzles produce higher levels of turbulence compared with the round nozzle in the near-field. For example, for $x^* = 7$, the peak values of P_k^* in the major axis plane of the rectangular nozzle is about 2 times greater than its corresponding value in the round nozzle. The values of P_k^* then decay with streamwise distance since $\partial U/\partial y$ decreases with streamwise distance and the levels of the streamwise Reynolds normal stress and the Reynolds shear stress are not significantly different from each other.

In the very near-field of the jets ($x^* = 2$), convection and diffusion terms predominantly act as sinks whiles the production term acts as a source of energy. However, as the jet evolves further downstream, both the convective and production terms act as sources of energy to the turbulent field while the diffusive term acts as a sink. At $x^* = 7$, for example, C_k^* for the cross and rectangular nozzle are significantly higher than its value for the round nozzle. By $x^* = 15$, the overall trend of the energy budget resembles those reported for a round jet in the self-similar region (e.g. Panchapakesan & Lumley, 1993). It should be noted that an analysis of the two convective terms shows that $U\partial k/\partial x$ is the dominant contributor to C_k.

4.2.5 Two-point auto-correlation

The two-point auto-correlation is a technique that is used to study the distances over which the turbulent field is correlated across the flow. It also provides an estimate of the size of the integral

scales of the flow. The two-point auto-correlation functions in the *x*-*y* plane at a reference point (x_r, y_r) for the streamwise (u) and transverse (v) fluctuating velocities, separated by the spatial distances Δx and Δy in the streamwise and transverse directions respectively is given by:

$$R_{uu} = \frac{\overline{(u(x_r,y_r)u(x_r+\Delta x,y_r+\Delta y))}}{(\sqrt{\overline{u^2}}(x_r,y_r)\sqrt{\overline{u^2}}(x_r+\Delta x,y_r+\Delta y))} \tag{4.4}$$

$$R_{vv} = \frac{\overline{(v(x_r,y_r)v(x_r+\Delta x,y_r+\Delta y))}}{(\sqrt{\overline{v^2}}(x_r,y_r)\sqrt{\overline{v^2}}(x_r+\Delta x,y_r+\Delta y))} \tag{4.5}$$

Contours of the R_{uu} and R_{vv} functions were obtained for the round, cross and rectangular nozzles at reference points $x^* = 4$ and 15 (on the jet centerline) to visualize the large-scale structures in the flow. One-dimensional profiles of R_{uu} and R_{vv} functions were also obtained at various streamwise locations (on the jet centerline) within the flow to estimate the streamwise and transverse extents of the large-scale structures respectively.

Figure 4.26 and Figure 4.27 show the contours of R_{uu} and R_{vv} at $x^* = 4$ on the jet centerline for the round, cross and rectangular nozzle in both the major and minor axis respectively. The effects of nozzle geometry are not apparent from the R_{uu} contours in the near-field region. The R_{vv} contours are more elongated in the transverse direction in the major axis of the rectangular nozzle compared to its minor axis, implying the structures are more correlated in the transverse direction in the near-field of the rectangular jet. By $x^* = 15$, the contours of both R_{uu} and R_{vv} (Figure 4.28 and Figure 4.29) are relatively larger for all the jets compared to their size at $x^* = 4$. The R_{uu} contours are more correlated in the streamwise direction whilst the R_{vv} contours are more correlated in the transverse direction. The effects of nozzle geometry are more evident in the transverse direction, with the largest transverse extent of the large-scale structures (R_{vv} contour) occurring in the major axis plane

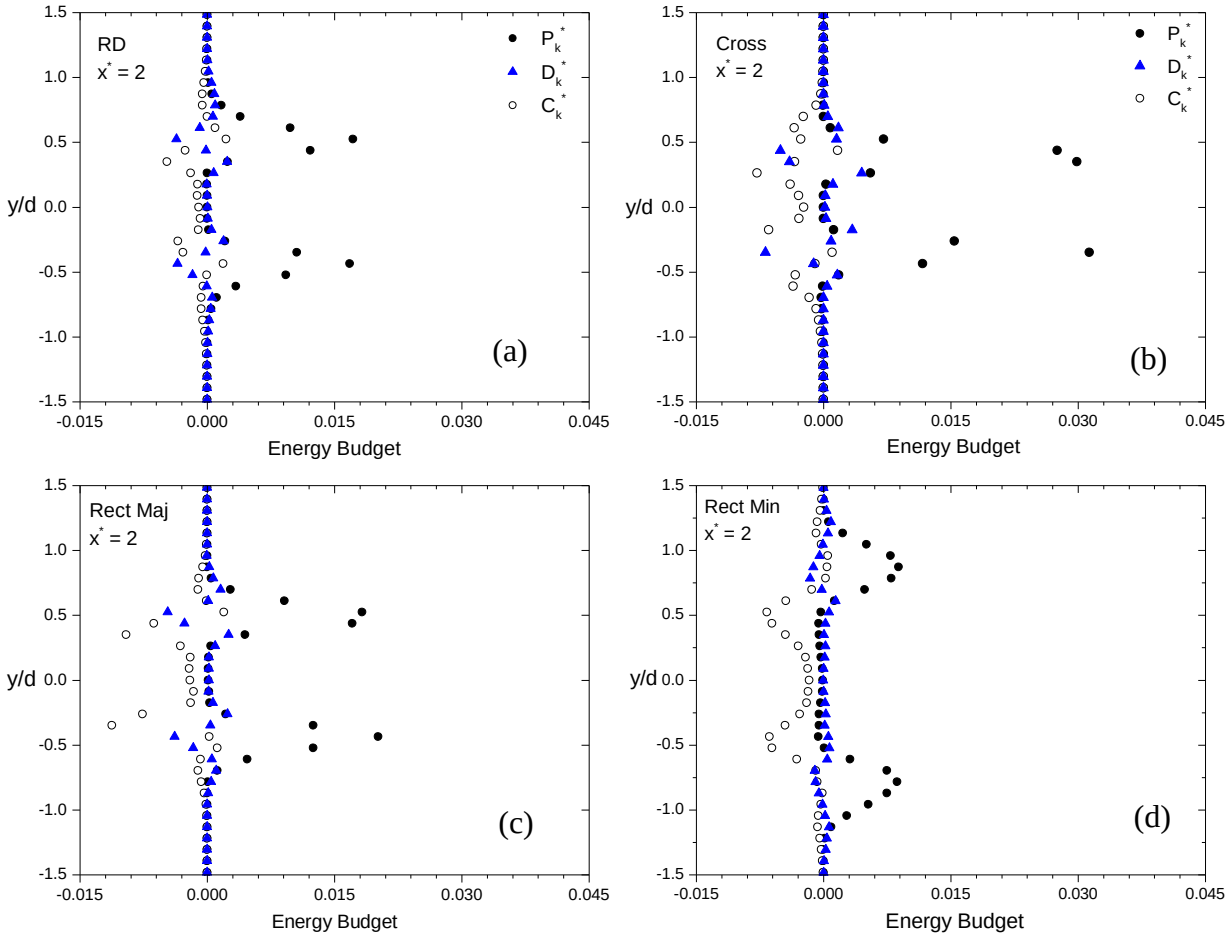

Figure 4.23: Energy budget at x^* = 2 for the (a) round, (b) cross and (c,d) rectangular nozzles

of the rectangular nozzle.

4.2.5.1 Scales of turbulence

In order to quantify the size of the large-scale structures in the jet flow, one-dimensional profiles of R_{uu} and R_{vv} (e.g. Figure 4.30) were extracted at various streamwise locations. The longitudinal (Lx_{uu}) and transverse (Ly_{vv}) integral length scales were obtained by integrating the profiles of R_{uu} and R_{vv} respectively as follows: $Lx_{uu} = \int_0^\infty R_{uu} dx$ and $Ly_{vv} = \int_0^\infty R_{vv} dy$. The variation of the

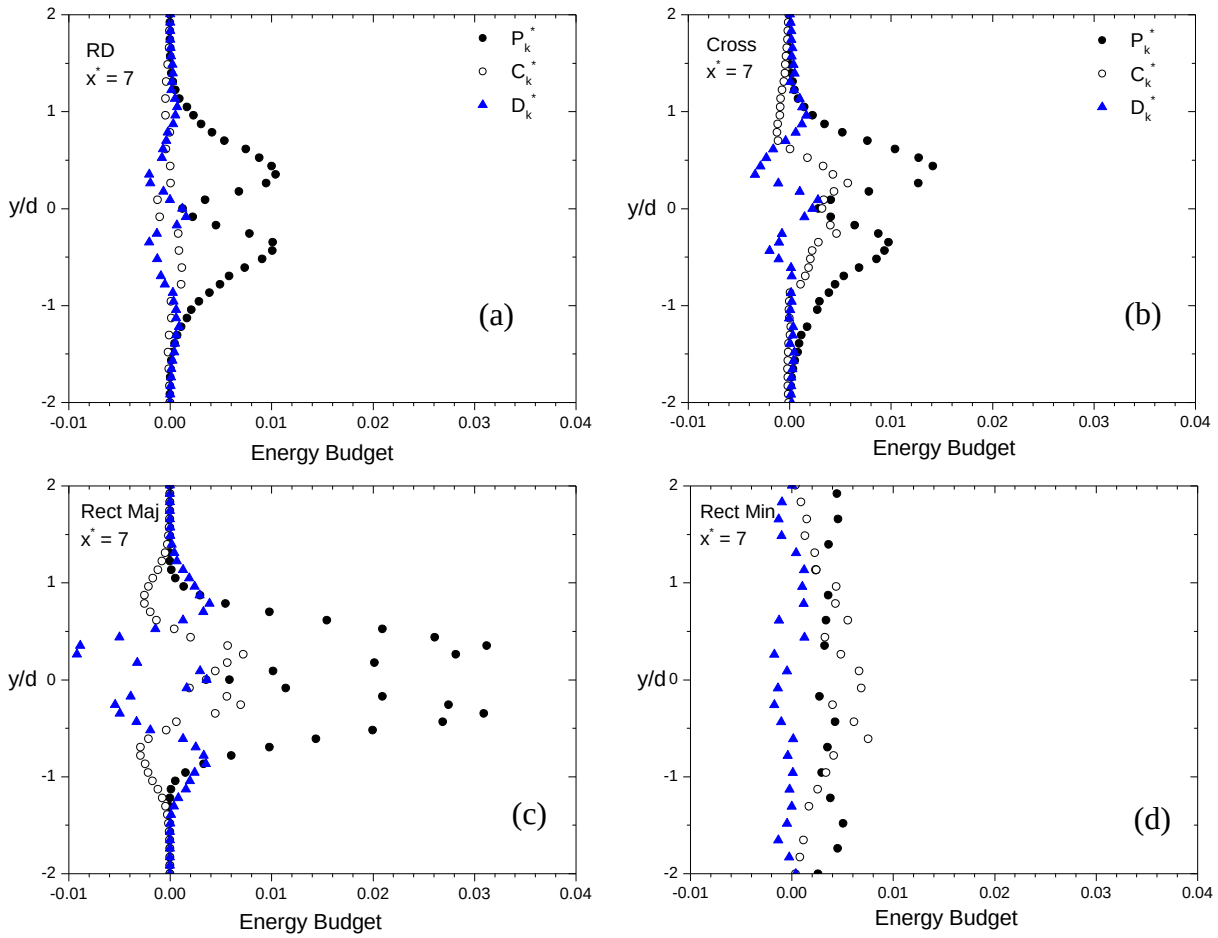

Figure 4.24: Energy budget at $x^* = 7$ for the (a) round, (b) cross and (c,d) rectangular nozzles

streamwise and transverse integral length scales with streamwise distance is presented in Figure 4.31. The plots are normalized by d (i.e. $Lx_{uu}^* = Lx_{uu}/d$ and $Ly_{vv}^* = Ly_{vv}/d$). It should be noted that the streamwise integral scales of the rectangular nozzle in both the major and minor axis are identical since they are extracted on the jet centerline. Lx_{uu}^* increases monotonically from the nozzle exit for all the jet nozzles. The linear growth rate of Lx_{uu}^* for the cross and rectangular nozzles are almost identical; however, they are about 20% greater than that of the round nozzle. In the case of Ly_{vv}^* however, the effects of nozzle geometry become more apparent; the structures in the major axis of the rectangular nozzle have a larger transverse extent compared to the round and

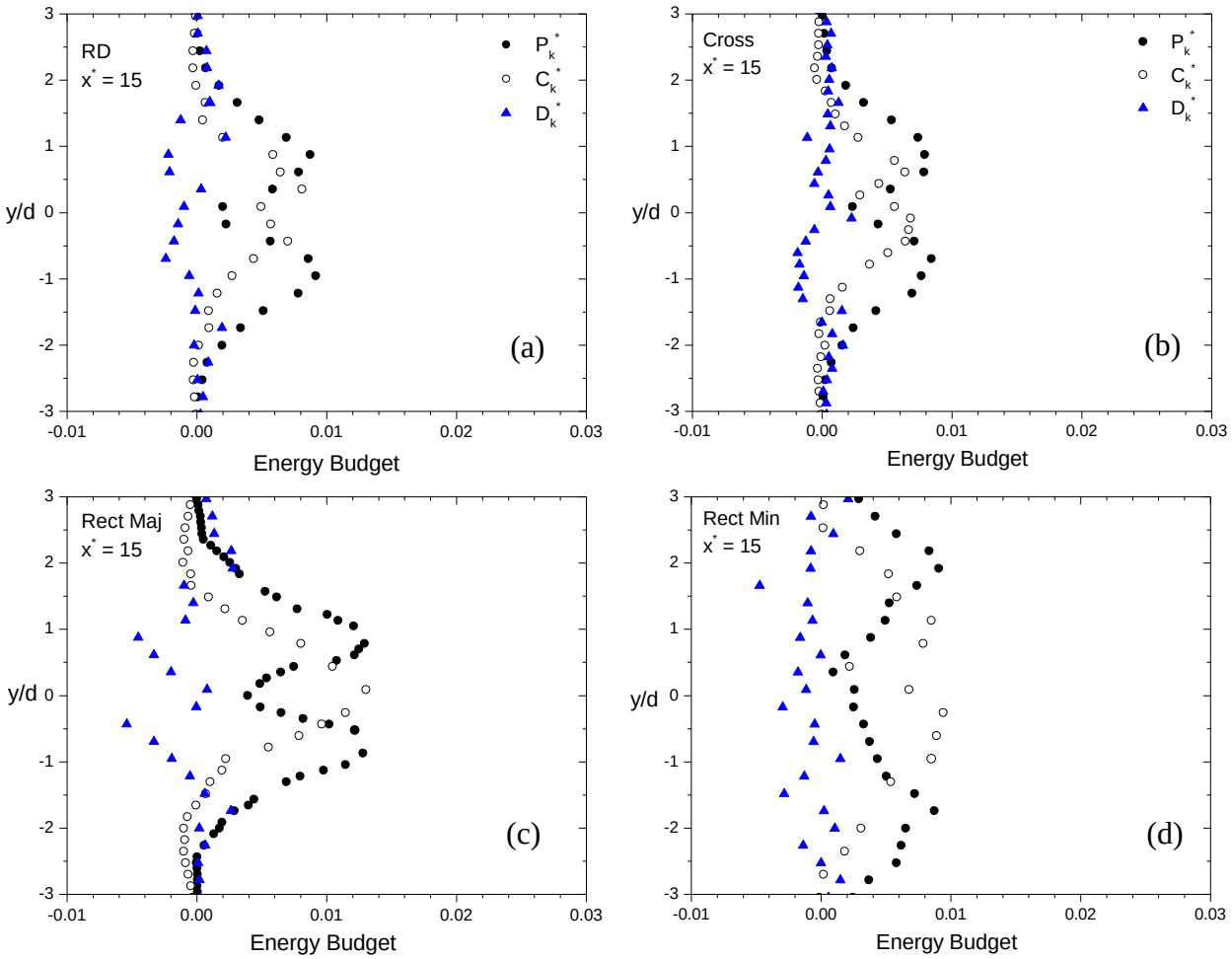

Figure 4.25: Energy budget at $x^* = 15$ for the (a) round, (b) cross and (c,d) rectangular nozzles

cross nozzles. For example, at $x^* = 15$, the transverse integral scale in the rectangular major plane is about 46% greater than those in the round nozzle. It should be noted that Ly_{vv}^* also increases with streamwise distance throughout the jet flow domain. The linear growth of L_{xuu}^* is consistent with previous studies (e.g. Mi & Nathan, 2010).

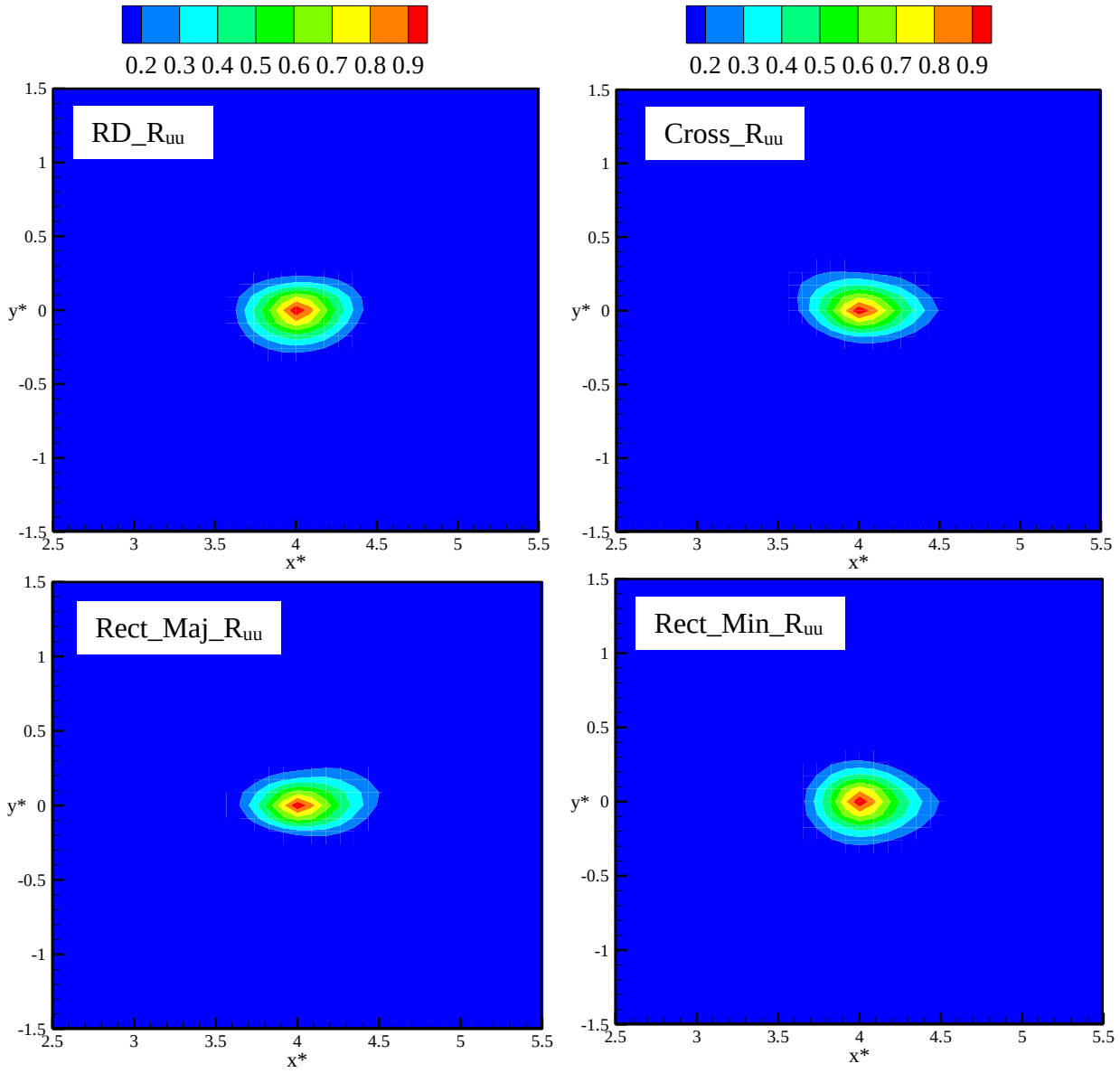

Figure 4.26: Contours of two-point auto-correlation function, R_{uu} at $x^* = 4$ for the round, cross and rectangular nozzle

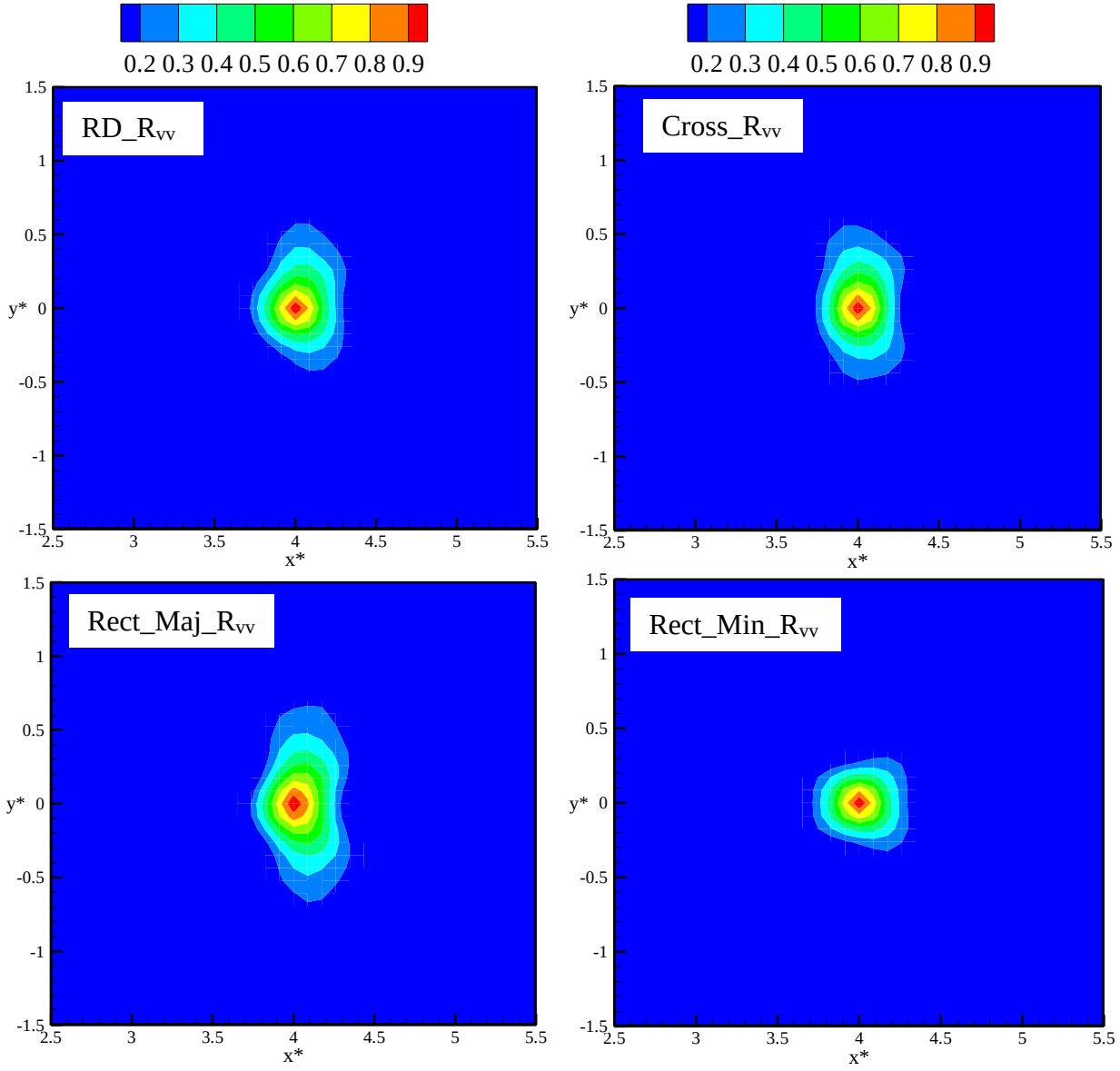

Figure 4.27: Contours of two-point auto-correlation function, R_{vv} at $x^* = 4$ for the round, cross and rectangular nozzle

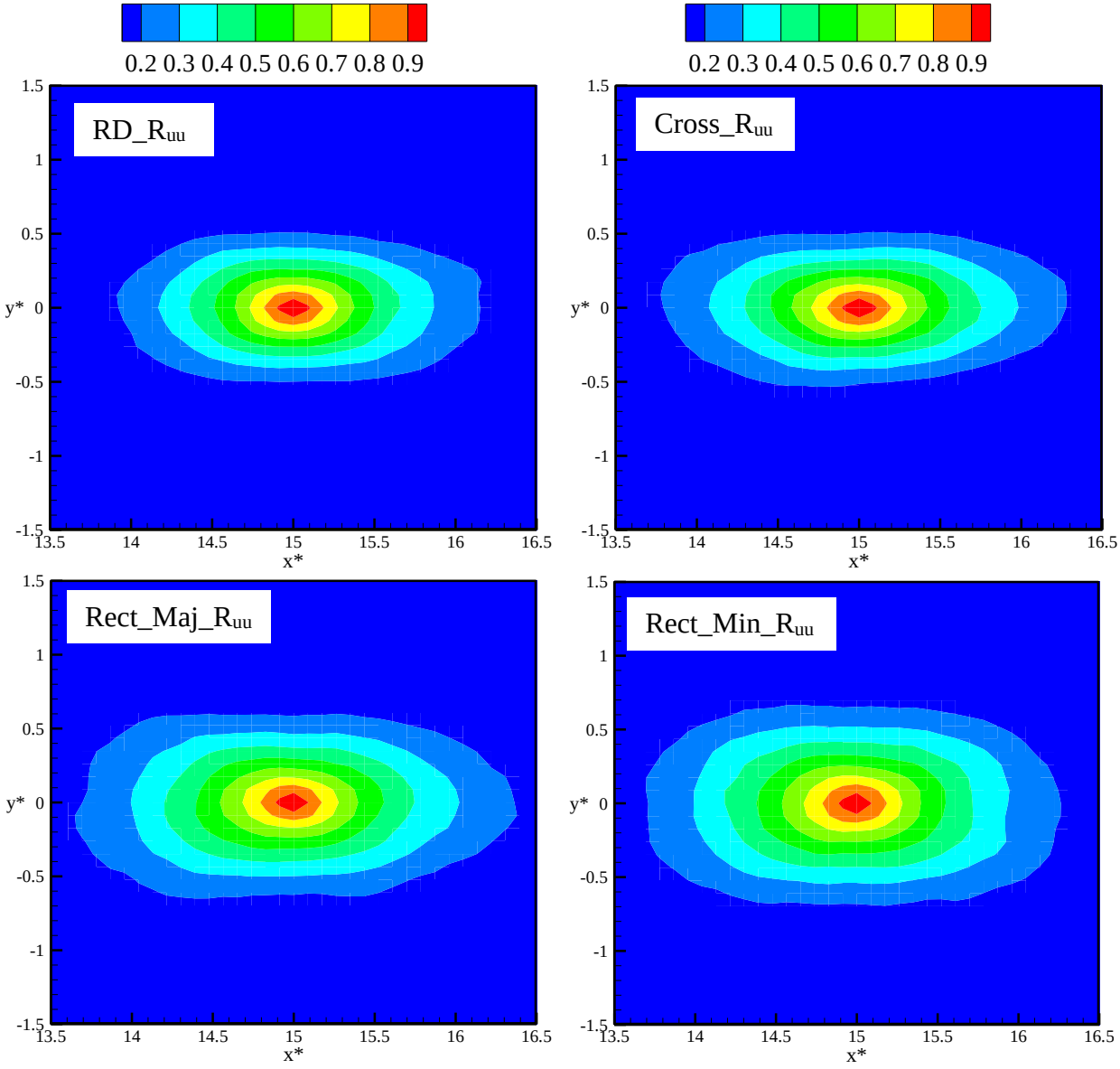

Figure 4.28: Contours of two-point auto-correlation function, R_{uu} at x^* = 15 for the round, cross and rectangular nozzle

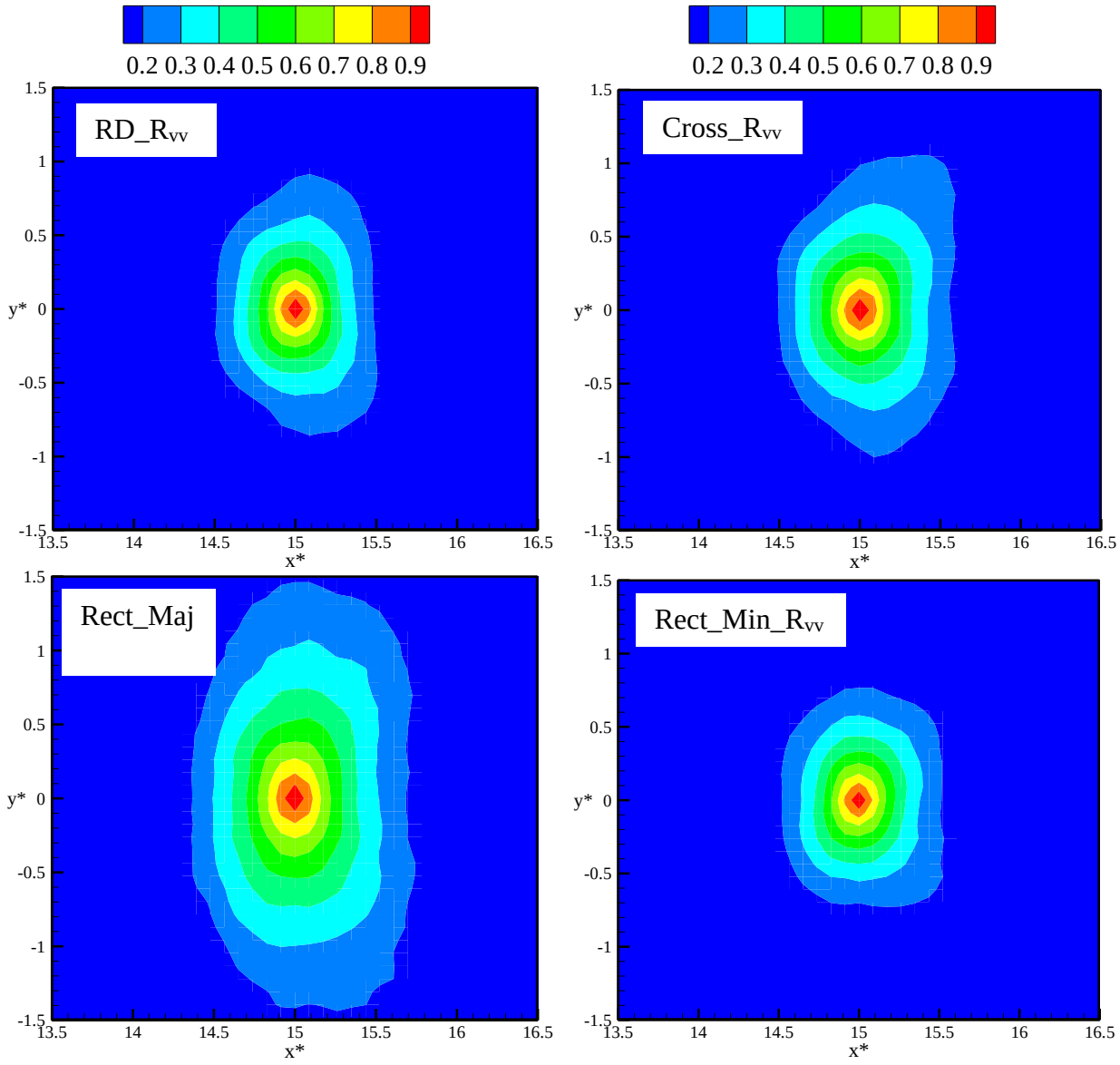

Figure 4.29: Contours of two-point auto-correlation function, R_{vv} at $x^* = 15$ for the round, cross and rectangular nozzle

The Taylor microscale (λ) and Kolmogorov (η) scales, representing the intermediate and smallest scales of the flow are presented in Figure 4.32 (normalized by d). The scales were estimated at various streamwise distances on the jet centerline throughout the flow. The Taylor microscale, $\lambda = \sqrt{\overline{u^2}/\overline{(\partial u/\partial x)^2}}$ increased with streamwise distance throughout the flow for the round, cross and rectangular nozzles studied. The linear rate of this increase was approximately constant (i.e. 0.006) for all the nozzles studied, implying no apparent nozzle geometry effect on the Taylor microscales. It should be noted that the spatial resolution of the current study was enough to resolve the Taylor microscales (0.1d to 0.3d), but not adequate to resolve the Kolmogorov scales (i.e. $0.005 \leq \eta/d \leq 0.01$). Nevertheless, the Kolmogorov scales were also estimated as follows: $\eta = (\nu^3/\varepsilon)^{0.25}$, where ε is the mean dissipation rate which was computed as $\varepsilon = 15\nu\overline{(\partial u/\partial x)^2}$. The Kolmogorov scales also exhibit a linear increase with streamwise distance for all the nozzles studied. It should be noted that the kinetic energy produced at the integral scales are transferred through an energy cascade to the Taylor microscale, which are in turn transferred to the Kolmogorov scales, where it is dissipated into heat. There was no significant effect of nozzle geometry on the Kolmogorov scales. This is consistent with Mi & Nathan (2010) who also observed no significant differences due to nozzle shapes on the Taylor microscale (λ/d = 0.211~0.236) and Kolmogorov scales (η/d = 0.0081~0.0093).

The separation of scales between the integral, Taylor and Kolmogorov scales was also investigated. At relatively high *Re*, the scale separation between the largest (integral) and the smallest (Kolmogorov) scales is large. This is because Kolmogorov scale, which depends on viscosity becomes smaller as *Re* is increased. The variation of the ratio of the integral length scales

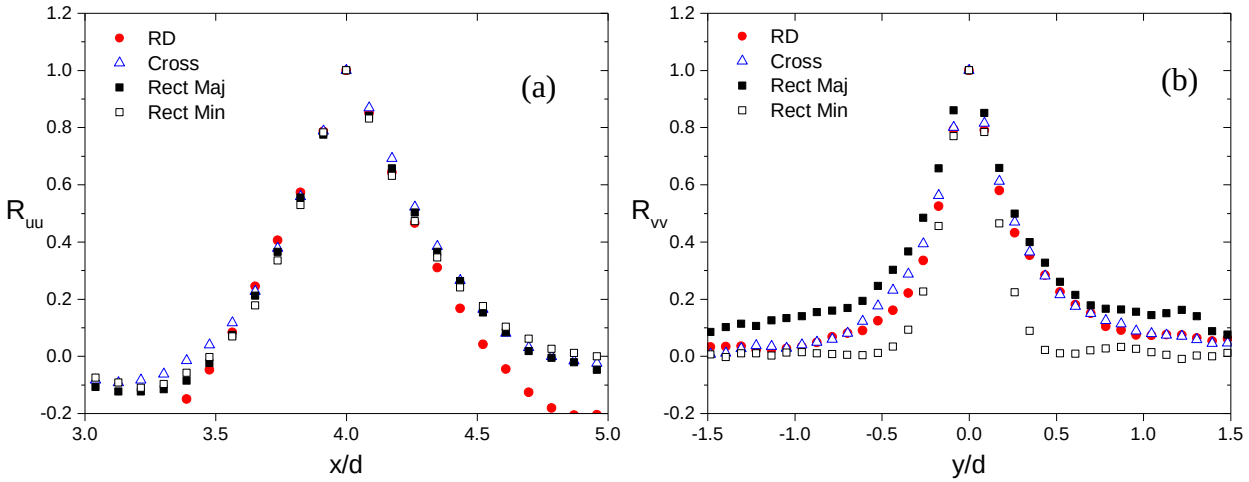

Figure 4.30: One-dimensional profiles of (a) R_{uu} and (b) R_{vv} for the round, cross and rectangular nozzles at $x^* = 4$

to the Kolmogorov scales (L/η) and the Taylor microscale (L/λ) with streamwise distance are shown in Figure 4.33 while the variation of the ratio of the Taylor microscale to the Kolmogorov scale (λ/η) with streamwise distance is shown in Figure 4.34. The ratios of L/η and L/λ increase with streamwise distance for all the jets considered because L, λ and η also increase with streamwise distance, with the integral scale increasing at the fastest rate. No significant effect of nozzle geometry is observed. At x/d = 25 for example, $L/\eta \approx 115$~130 and $L/\lambda \approx 3.7$~4.3 for the round cross and rectangular nozzles. The values of L/η reported in Mi & Nathan (2010) for different nozzle shapes at Re_b = 15,000 are slightly higher (i.e. 150~250) than those reported in the present study since η decreases with increasing Re (e.g. Mi et al., 2013). This implies the scale separation at relatively low Re is small and therefore there is interaction between the scales of the flow unlike at relatively high Re. λ/η also increases with streamwise distance and does not show any effect nozzle geometry. For example, at $x^* = 25$, $\lambda/\eta \approx 28$~33 and this differs slightly with Mi & Nathan (2010) who reported $\lambda/\eta \approx 30$~50 due to Re dependence of both λ and η.

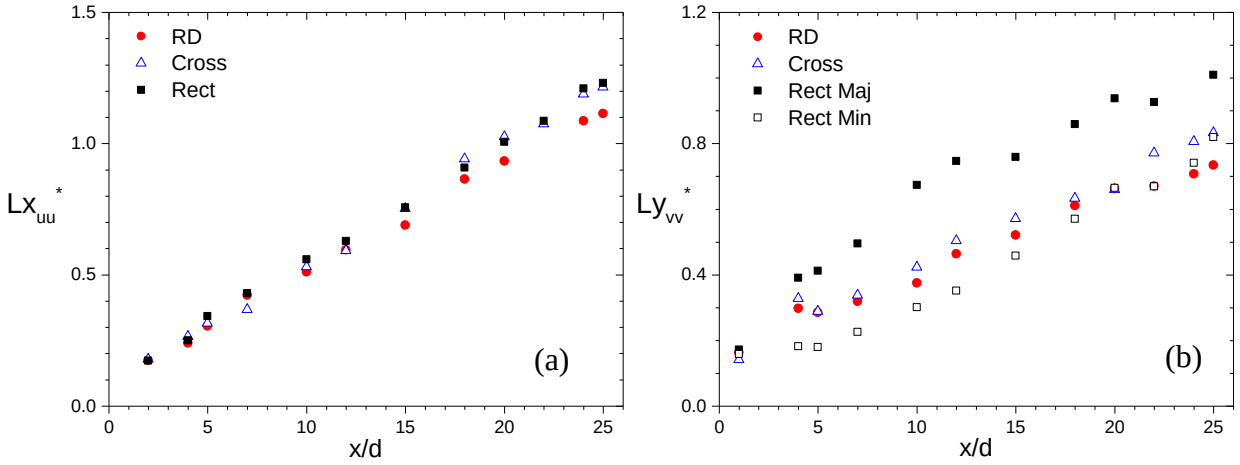

Figure 4.31: Variation of the (a) longitudinal and (b) transverse integral length scales with streamwise distance

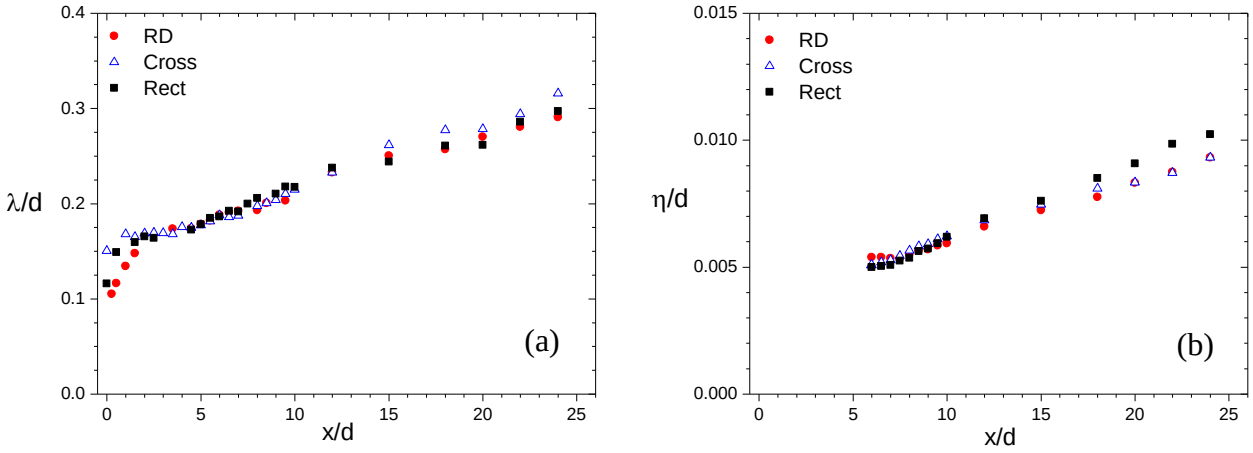

Figure 4.32: Variation of (a) Taylor microscale and (b) Kolmogorov scales with streamwise distance

A Reynolds number based on $y_{0.5}$ and U_c (Re_m) was estimated for the round, cross and rectangular nozzle and is shown in Figure 4.35. In the self-similar region of a round jet, the conservation of momentum in the jet requires the product of ($U_c \times y_{0.5}$) to remain constant and as a result Re_m also becomes constant (Pope, 2000). As a result, Re_m is observed to remain fairly constant for the round

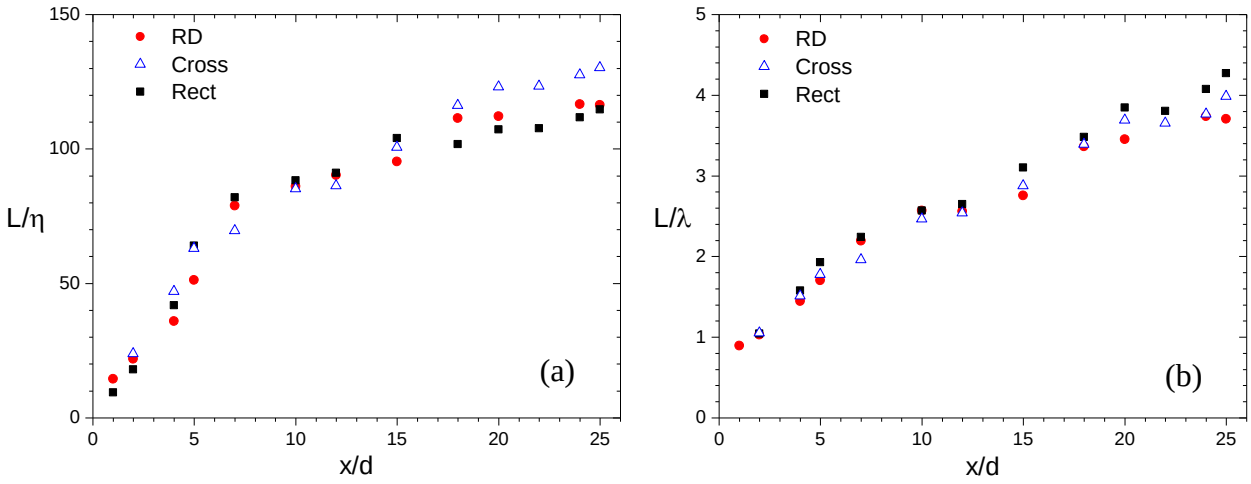

Figure 4.33: Variation of the ratio of integral scale to (a) Kolmogorov and (b) Taylor microscales respectively with streamwise distance

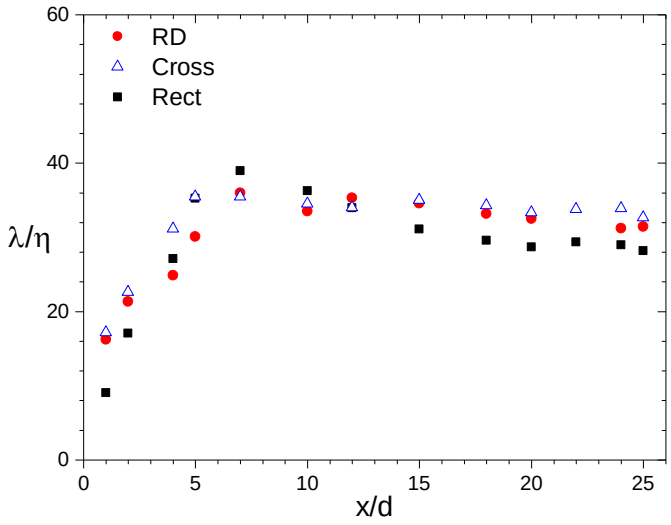

Figure 4.34: Variation of the ratio of Taylor microscale to Kolmogorov scale with streamwise distance

and cross nozzles. However, due to the differential spreading in the major and minor axis of the rectangular nozzle, which results in axis switching, the local Reynolds number deviates from that of the round nozzle. However, beyond the developing region, the jets from all nozzles seem to

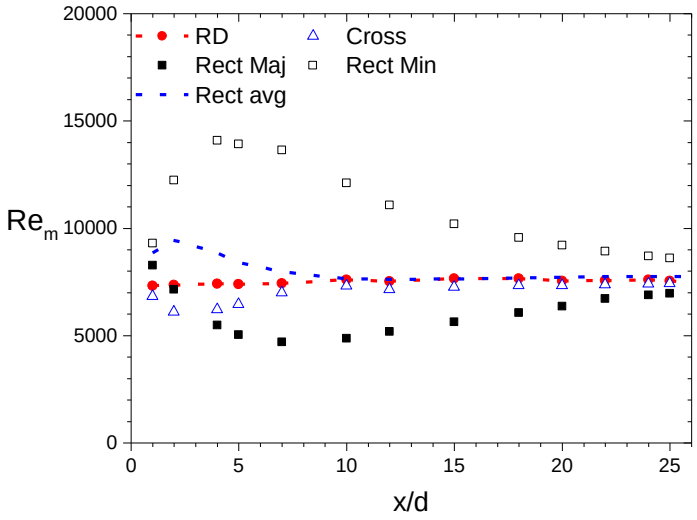

Figure 4.35: Variation of the Reynold number based on U_c and $y_{0.5}$ with streamwise distance

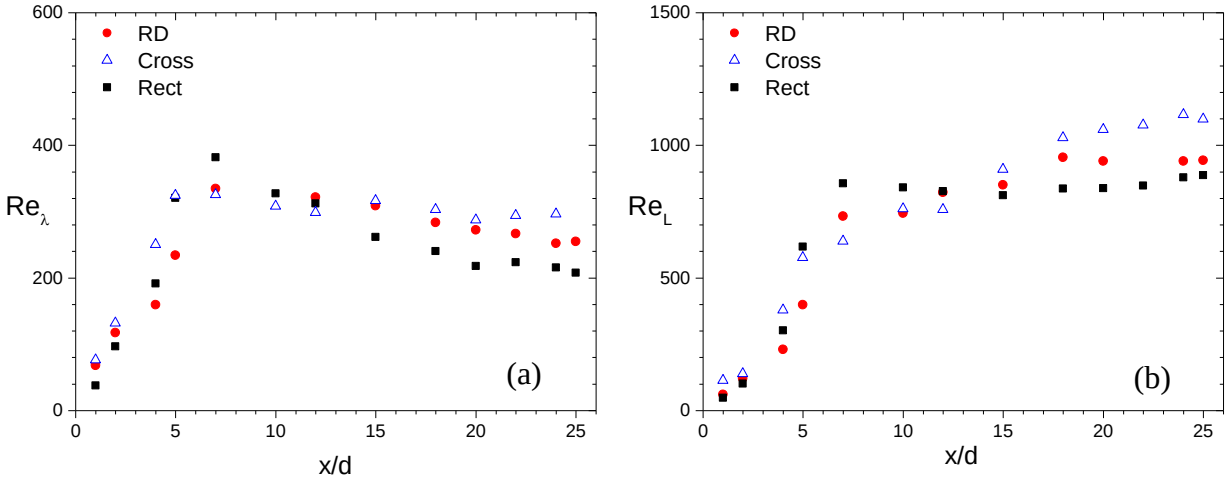

Figure 4.36: Variation of the Reynolds number based on (a) Taylor microscale and (b) integral length scales with streamwise distance

converge towards $Re_m \approx 7500$. The geometric mean of Re_m was calculated for the rectangular nozzle and is also shown in Figure 4.35. In the near field of the rectangular jet, due to the faster growth of $y_{0.5}$, Re_m is greater compared with the round nozzle, but after say $x^* > 7$, the local Reynolds number is identical with the round jet, implying that the changes due to the nozzle

geometry are more significant in the near-field of the jet. The Taylor Reynolds number (Re_λ) based on the streamwise turbulent intensity, $\sqrt{\overline{u^2}}$ and the Taylor microscale is shown in Figure 4.36 (a). Re_λ first increases with streamwise distance near the nozzle exit, before decaying to a fairly constant range of $Re_\lambda \approx 216$~296 at about $x^* = 24$. Re_λ was also observed to be constant in the self-similar region of a round jet (e.g. Mi et al., 2013). The large-scale Reynolds number (Re_L), based on $\sqrt{\overline{u^2}}$ and L are shown in Figure 4.36 (b). For Re_L, there is a consistent increase from the nozzle exit before reaching $Re_L \approx 879$~1115 at about $x^* = 24$.

4.2.6 Summary

The round, cross and rectangular air jets were studied. The rectangular and cross nozzles showed a smaller potential core length and higher decay rate compared with the round nozzle. The spread rates computed with the conventional $y_{0.5}$, as well as $y_{0.1}$ and $y_{0.75}$ showed the greatest spreading occurring in the rectangular nozzle due to the axis-switching mechanism. This implies a greater mixing capacity in the non-circular nozzles. The rectangular nozzle also showed the highest values of the turbulent intensity and Reynolds shear stress. In terms of the energy budget, the non-circular nozzles had a higher production of turbulence and convection by the mean flow. Finally, the two-point auto-correlation functions revealed a faster growth rate of the streamwise integral length scale of the non-circular nozzles compared with the round one while the transverse integral length scale was largest in the rectangular nozzle. This implies that nozzle geometry effects were evident in the largest structures of the flow; however the intermediate and smallest structures as well as their relative magnitudes were not affected by nozzle geometry.

5 SUMMARY, CONCLUSIONS AND RECOMMENDATION FOR FUTURE WORK

5.1 Summary

An experimental investigation was conducted to study the effect of nozzle geometry on turbulent free orifice jets. Detailed velocity measurements were performed for jets issuing from a round, square, cross, rectangle and ellipse (of aspect ratio 2), star and flower nozzle using particle image velocimetry (PIV). The experiments were conducted in two stages; first in a water tunnel to investigate the effect of nozzle geometry on the decay and spread rates, as well as mass entrainment. The best nozzles identified from the first stage were further analyzed in air test facility to determine their turbulent characteristics. The air jets were analyzed using mean velocities, turbulent intensities, Reynolds stresses, structure parameter, Reynolds stress ratio and some budget terms in the turbulent kinetic energy transport equation. Two-point auto-correlation functions were also used to investigate the large-scale structures in the flow field as well as estimate the size of the structures in the various jets.

5.2 Conclusions

The conclusions from the present study include:

- The non-circular nozzles had a higher decay rate than the round nozzle. In particular, the rectangular and elliptical nozzles had the highest decay rates of the nozzle geometries studied, implying a greater mixing capacity of jets produced from them.
- Apart from the conventional half-width ($y_{0.5}$), other velocity widths (i.e. $y_{0.9}$, $y_{0.75}$, $y_{0.5}$, $y_{0.25}$, $y_{0.1}$) were used to estimate the spreading of the jets. In all cases, the non-circular nozzles had higher spread rates compared to the round nozzle. In particular, the rectangular and

elliptical nozzles had the greatest spreading rate regardless of the jet velocity width used and this was due to the axis-switching mechanism.

- The location at which axis-switching took place remained identical regardless of the jet velocity width that was used to estimate it.
- The jets produced from non-circular geometries had a thicker jet width than those produced from the round nozzle and was directly correlated to the spreading rates of these jets, i.e. the rectangular, elliptical and cross nozzles had the greatest spread rates and jet thickness.
- There was a greater mass entrainment in the minor axis plane of both the rectangular and elliptical jets compared with their respective major axis planes as well as all the other nozzle geometries studied.
- Jets produced from the rectangular nozzle had the greatest streamwise turbulent intensity on the jet centerline and the highest shear layer values of the Reynolds shear stress.
- Evaluation of the energy budget revealed there was more production of turbulence and convection of the mean flow in the non-circular (e.g. rectangular and cross) nozzles compared with the round nozzle. The production and convection terms acted as sources of energy to the turbulent field, while the diffusion term acted as a sink.
- Two-point correlation function revealed higher growth rate of the integral scales in the streamwise direction for the non-circular nozzles. The transverse integral length scale was largest in the rectangular nozzle.
- The Taylor microscale and the Kolmogorov scales did not show any nozzle geometry dependence; their relative sizes of the scales of turbulence also showed no nozzle geometry effect.

5.3 Recommendation for future work

The findings of the current study can be advanced by applying the results to the study of multiple jets. Also, the effect of row of nozzles as well as their spacing can be studied to add to the body of knowledge of turbulent free jets.

REFERENCES

Abdel-Rahman, A. (2010). A review of effects of initial and boundary conditions on turbulent jets. *WSEAS Transactions on Fluid Mechanics*, *5*(4), 257–275. Retrieved from http://www.wseas.us/e-library/transactions/fluid/2010/52-334.pdf

Abdel-Rahman, A. A., Al-Fahed, S. F., & Chakroun, W. (1996). The near-field characteristics of circular jets at low Reynolds numbers. *Mechanics Research Communications*, *23*(3), 313–324. http://doi.org/10.1016/0093-6413(96)00028-6

Ball, C. G., Fellouah, H., & Pollard, a. (2012). The flow field in turbulent round free jets. *Progress in Aerospace Sciences*, *50*, 1–26. http://doi.org/10.1016/j.paerosci.2011.10.002

Coleman, H. W., & Steele, W. G. (1995). Engineering Application of Experimental Uncertainty Analysis. *AIAA Journal*, *33*(10), 1888–1896. Retrieved from http://arc.aiaa.org/doi/abs/10.2514/3.12742

Deo, R. C., Mi, J., & Nathan, G. J. (2008). The influence of Reynolds number on a plane jet. *Physics of Fluids*, *20*(7), 1–16. http://doi.org/10.1063/1.2959171

Forliti, D. J., Strykowski, P. J., & Debatin, K. (2000). Bias and precision errors of digital particle image velocimetry. *Experiments in Fluids*, *28*(5), 436–447. http://doi.org/10.1007/s003480050403

George, W. K. (1989). The self-preservation of turbulent flows and its relation to initial conditions and coherent structures. *Advances in Turbulence*, 39–73.

Goldschmidt, V. W., & Bradshaw, P. (1981). Effects of Nozzle Exit Turbulence on the Spreading (or Widening) Rate of Plane Free Jets. *Fluids Engineering Division of the American Society of Mechanical Engineers (81-FE-22)*.

Grinstein, F. F. (1997). Entrainment, axis switching and aspect- ratio effects in rectangular free

jets. In *4th Shear Flow Control Conference*.

Gutmark, E. J., & Grinstein, F. F. (1999). Flow control with noncircular jets. *Annual Review of Fluid Mechanics*, *31*, 239–272. http://doi.org/10.1146/annurev.fluid.31.1.239

Gutmark, E., & Wygnanski, I. (1976). The planar turbulent jet. *Journal of Fluid Mechanics*, *73*(3), 465–495. http://doi.org/10.1017/S0022112076001468

Ho, C.-M., & Gutmark, E. (1987). Vortex induction and mass entrainment in a small-aspect-ratio elliptic jet. *Journal of Fluid Mechanics*, *179*, 383–405. http://doi.org/10.1017/S0022112087001587

Hu, H., Kobayashi, T., Saga, T., Segawa, S., & Taniguchi, N. (2000). Particle image velocimetry and planar laser-induced fluorescence measurements on lobed jet mixing flows. *Experiments in Fluids*, 141–157. http://doi.org/10.1007/s003480070016

Hussain, F., & Husain, H. (1989). Elliptic jets. Part 1. Characteristics of unexcited and excited jets. *Journal of Fluid Mechanics*, *208*, 257–320. Retrieved from http://journals.cambridge.org/abstract_S0022112089002843

Hussein, H. J., Capp, S. P., & George, W. K. (1994). Velocity measurements in a high-Reynolds-number, momentum-conserving, axisymmetric, turbulent jet. *J. Fluid Mech.*, *258*, 31–75. Retrieved from http://journals.cambridge.org/abstract_S002211209400323X

Khashehchi, M., Ooi, A., Soria, J., & Marusic, I. (2013). Evolution of the turbulent/non-turbulent interface of an axisymmetric turbulent jet. *Experiments in Fluids*, *54*. http://doi.org/10.1007/s00348-012-1449-3

Krothapalli, A., Baganoff, D., & Karamcheti, K. (1981). On the mixing of a rectangular jet. *J. Fluid Mech.*, *107*(1), 201–220. http://doi.org/10.1017/S0022112081001730

Laurence, J. C. (1955). Intensity, scale and spectra of turbulence in mixing region of free subsonic

jet. Cleveland, Ohio.

Lee, S.-J., & Baek, S.-J. (1994). The effect of aspect ratio on the near-field turbulent structure of elliptic jets. *Flow Measurement and Instrumentation*, *5*(3), 170–180.

Liepmann, D., & Gharib, M. (1992). The role of streamwise vorticity in the near-field entrainment of round jets. *Journal of Fluid Mechanics*, *245*, 643–668. http://doi.org/10.1017/S0022112092000612

Lipari, G., & Stansby, P. K. (2011). Review of Experimental Data on Incompressible Turbulent Round Jets. *Flow, Turbulence and Combustion*, *87*, 79–114. http://doi.org/10.1007/s10494-011-9330-7

Mi, J., Kalt, P., Nathan, G. J., & Wong, C. Y. (2007). PIV measurements of a turbulent jet issuing from round sharp-edged plate. *Experiments in Fluids*, *42*(4), 625–637. http://doi.org/10.1007/s00348-007-0271-9

Mi, J., & Nathan, G. J. (2010). Statistical Properties of Turbulent Free Jets Issuing from Nine Differently-Shaped Nozzles. *Flow, Turbulence and Combustion*, *84*(4), 583–606. http://doi.org/10.1007/s10494-009-9240-0

Mi, J., Nathan, G. J., & Nobes, D. S. (2001). Mixing Characteristics of Axisymmetric Free Jets From a Contoured Nozzle, an Orifice plate and a Pipe. *Journal of Fluids Engineering*, *123*(4), 878–883. http://doi.org/10.1115/1.1412460

Mi, J., Xu, M., & Zhou, T. (2013). Reynolds number influence on statistical behaviors of turbulence in a circular free jet. *Physics of Fluids*, *25*(7). http://doi.org/10.1063/1.4811403

Namer, I., & Ötügen, M. V. (1988). Velocity measurements in a plane turbulent air jet at moderate Reynolds numbers. *Experiments in Fluids*, *6*, 387–399.

Panchapakesan, N. R., & Lumley, J. L. (1993). Turbulence measurements in axisymmetric jets of

air and helium. Part 1. Air jet. *Journal of Fluid Mechanics*, *246*, 197–223. http://doi.org/10.1017/S0022112093000096

Pope, S. B. (2000). *Turbulent flows*. Cambridge University Press. http://doi.org/10.1017/CBO9780511840531

Quinn, W. R. (1989). On mixing in an elliptic turbulent free jet. *Physics of Fluids A: Fluid Dynamics*, *1*(10), 1716–1722. http://doi.org/10.1063/1.857536

Quinn, W. R. (1991). Passive Near-Field Mixing Enhancement in Rectangular Jet Flows. *AIAA Journal*, *29*(4), 515–519.

Quinn, W. R. (2006). Upstream nozzle shaping effects on near field flow in round turbulent free jets. *European Journal of Mechanics-B/Fluids*, *25*(3), 279–301. http://doi.org/10.1016/j.euromechflu.2005.10.002

Raffel, M., Willert, C., Wereley, S., & Kompenhans, J. (1998). *Particle image velocimetry - A practical guide*. Springer-Verlag.

Tandalam, A., Balachandar, R., & Barron, R. (2010). Reynolds Number Effects on the Near-Exit Region of Turbulent Jets. *Journal of Hydraulic Engineering*, *136*(9), 633–641. http://doi.org/10.1061/(ASCE)HY.1943-7900.0000232

Tso, J., & Hussain, F. (1989). Organized motions in a fully developed turbulent axisymmetric jet. *Journal of Fluid Mechanics*. http://doi.org/10.1017/S0022112089001539

Westerweel, J., Draad, A. A., van der Hoeven, J. G. T., & van Oord, J. (1996). Measurement of full-developed turbulent pipe flow with digital particle image velocimetry. *Experiments in Fluids*, *20*, 165–177.

Wygnanski, I., & Fiedler, H. (1969a). Some measurements in the self-preserving jet. *J. Fluid Mech.*, *38*, 577–612. http://doi.org/10.1017/S0022112069000358

Wygnanski, I., & Fiedler, H. (1969b). Some measurements in the self-preserving jet. *Journal of Fluid Mechanics, 38,* 577–612. http://doi.org/10.1017/S0022112069000358

Yoon, J.-H., & Lee, S.-J. (2003). Investigation of the near-field structure of an elliptic jet using stereoscopic particle image velocimetry. *Measurement Science and Technology, 14*(12), 2034–2046. http://doi.org/10.1088/0957-0233/14/12/002

APPENDIX

A.1 CONVERGENCE TEST

In order to determine the sample size that would be adequate to accurately compute the mean and higher order turbulent statistics, a convergence test was performed. The required sample size for statistical convergence of the mean and higher order turbulent statistics generally depends on the specific statistic being measured and the turbulence levels of the flow. Sample sizes of N = 2000, 4000 and 6000 were used to calculate the mean velocity, turbulent intensities, Reynolds shear stress and the triple velocity correlations (i.e. $\overline{u^3}$ and $\overline{v^3}$) in the near-field region (x^* = 4) and the developing region (x^* = 22) of the jets studied. The results for the round nozzle used in the air experiments is presented in Figure A.1. The results of the convergence test conducted show that N ≥ 2000 is sufficient to obtain statistically independent measures of the mean velocity, turbulent intensities and the Reynolds shear stress. For the case of the triple velocity correlations, by N = 6000, the statistics converge. As a result, a sample size of 6000 image pairs were used in acquiring the mean and higher order statistics that are presented in the current study. The sample size used in this study is greater than the 2000 samples that was used in both Tandalam et al. (2010) and Khashehchi et al. (2013) to compute the mean velocity, vorticity, turbulent intensities, Reynolds shear stress and proper orthogonal decomposition of turbulent jet flows. It should be noted that the measurement uncertainty also reduces with a larger sample size.

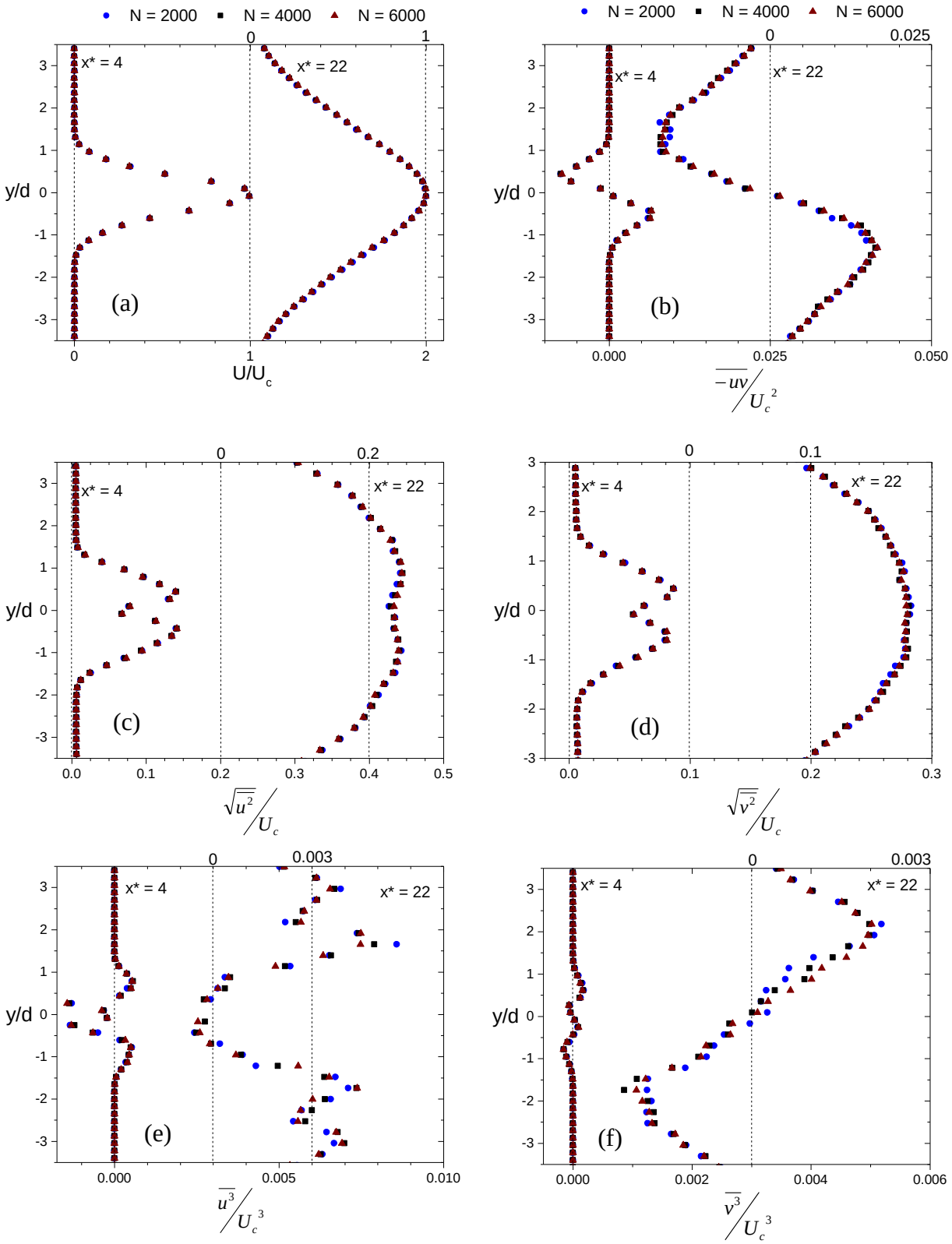

Figure A.1: Profiles of (a) streamwise mean velocity, (b) Reynolds shear stress (c,d) turbulent intensities and (e,f) triple velocity correlations for N = 2000, 4000 and 6000.

B.1 MEASUREMENT UNCERTAINTY

Measurement error or uncertainty can be defined as the deviation of an experimentally determined value from the true value of a physical variable. A detailed uncertainty methodology was presented in Coleman & Steele (1995), following the AIAA standard. There are two components of the total error; the precision (random) error and the bias (systematic) error. An error is classified as a precision error if it contributes to the scatter of the data while it is classified as bias if it is a systematic error (Coleman & Steele, 1995). A Gaussian peak-fitting algorithm has been found to produce the lowest bias and precision errors and consequently, reduce the uncertainty associated with measurements (e.g. Forliti et al., 2000). For PIV measurements, sources of error include selection of time between pulses, sub-pixel displacement bias, insufficient sample size and spatial resolution. Additional sources of error also include positioning of the laser sheet, particle response time to fluid motion and errors arising from algorithms that determine the average particle displacement.

In order to minimize the error in the current study, a large sample size was used, which reduced the precision error. Also, the tracer particles chosen based on the settling velocity and response time confirmed that these particles will follow the flow "faithfully". During the calibration process, the laser sheet was carefully aligned to the mid-span of the test section and the maximum particle displacement was set to ¼ of the interrogation window used.

B.2 ERROR ESTIMATION

Analysis of the bias and precision errors for the PIV measurement in this study is presented in this section

B.2.1 BIAS ERRORS

The instantaneous velocity at any given point for PIV measurements is given by:

$$U_i = \Delta s_i L_O / \Delta t L_i \quad \text{(B.1)}$$

where U_i is the velocity component, Δs_i is the component of the particle displacement in the *x*-*y* direction obtained from the correlation algorithm, L_O is the width of the field of view of the camera, Δt is the time between pulses and L_I is the width of the digital image.

The bias limit of the measured velocity is determined with a root-sum-square (RSS) of the elementary bias limits based on the sensitivity coefficients, which are given as:

$$B_{Ui}^2 = \theta_{\Delta si}^2 B_{\Delta si}^2 + \theta_{Lo}^2 B_{Lo}^2 + \theta_{\Delta ti}^2 B_{\Delta ti}^2 + \theta_{LI}^2 B_{LI}^2 \quad \text{(B.2)}$$

where the sensitivity coefficients, θ_x, are defined as:

$$\theta_x = \partial U_i / \partial X \quad \text{(B3)}$$

where X = (Δs_i, L_O, Δs_i and L_I).

The bias errors were estimated for *U* and *V* for the various test conditions and a typical case presented for the round nozzle in the near-field of the air experiments. A summary of the results are presented in Table B. and Table B.2. The bias limits of Δs and Δt were obtained from the PIV

Table B.1: Bias limits of the local streamwise mean velocity (U) in the near-field of the jet

Variable	***Magnitude***	B_x	θ_x	$B_x\theta_x$	$(B_x\theta_x)^2$
L_O (m)	1.00E-01	5.00E-04	5.93E+01	2.96E-02	8.78E-04
L_I (pix)	2.05E+03	5.00E-01	-2.89E-03	-1.45E-03	2.09E-06
Δt (s)	2.31E-05	1.00E-07	-2.57E+05	-2.57E-02	6.60E-04
Δs (pix)	2.80E+00	1.27E-02	2.12E+00	2.69E-02	7.24E-04
U (m/s)	2.60E+00				
				$\Sigma(B_x\theta_x)^2$	2.26E-03
				Bias Error	4.76E-02
				%Bias Error	1.83%

Table B.2: Bias limits of the local transverse mean velocity (V) in the near-field of the jet

Variable	***Magnitude***	B_x	θ_x	$B_x\theta_x$	$(B_x\theta_x)^2$
L_O (m)	1.00E-01	5.00E-04	2.12E+00	3.92E-02	1.12E-06
L_I (pix)	2.05E+03	5.00E-01	-1.03E-04	-1.92E-03	2.67E-09
Δt (s)	2.31E-05	1.00E-07	-9.17E+03	-3.40E-02	8.41E-07
Δs (pix)	1.00E-01	1.27E-02	2.12E+00	9.97E-01	7.22E-04
V (m/s)	5.50E-01				
				$\Sigma(B_x\theta_x)^2$	7.24E-04
				Bias Error	2.69E-02
				%Bias Error	4.89%

manufacturer's specifications. Finally, the bias limit of L_O is obtained from a calibration procedure.

B.2.2 PRECISION ERROR

The precision error, P, of a measured variable, X is given by:

$$\boldsymbol{P_x = K\sigma/\sqrt{N}} \tag{B.4}$$

where K is the confidence coefficient and $\boldsymbol{\sigma}$ is the standard deviation of the sample of N readings of the variable X. To determine the standard deviation, the sample size used (i.e. 6000) was sub-divided into 10 sets and each set was used to calculate the mean velocities. The standard deviation was then calculated from the 10 readings at the locations of interest. At 95% confidence level, K = 2. The precision error for U and V were estimated as approximately 0.09% and 0.03% respectively. Due to the large sample size used, the precision error is negligible. Therefore the total uncertainty is due almost entirely to the bias error.

B.2.3 TOTAL ERROR

The total uncertainty *E*, in the result U_i is the root-sum-square of the bias and precision limits, given by:

$$E = \sqrt{P_x + B_x} \tag{B.5}$$

The total uncertainty was obtained from the values of the bias and precision errors obtained. The measurement uncertainty at 95% confidence level in the mean velocities, *U* and *V*, was estimated to be 1.8% and 4.8% respectively. The measurement uncertainty in the turbulence intensities and Reynolds stresses was estimated to be $\pm$7% and $\pm$10%. The uncertainty in the triple velocity correlations and energy budget terms is of the order of ± 15%.